RR Lyrae Stars
as Tracers of Substructure
in the Galactic Halo

Sayuri Louise Prior

A thesis submitted for the degree of

Master of Philosophy
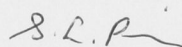
of The Australian National University

Disclaimer

This thesis contains my own original work, except where noted in the text or below.

Observations   Follow-up observations were taken by me, except for:
  ★ November 2006 40″ observations were taken by
     Simon Murphy and Stefan Keller.
  ★ While I was observing on the 2.3 m telescope
     - February, May and October 2007 40″ observations
       were taken by Gary Da Costa.
     - August 2007 40″ observations were taken by Keller.
  ★ Nightly scheduling of 40″ observations was partly done
     using a script by Keller.
  ★ A few extra 2.3 m observations were kindly taken by
     Mike Bessell during his run after very poor weather
     during our May 2007 run.

Reductions   ★ Da Costa performed initial reduction stages of
     some of the 40″ data.
  ★ Some of the 40″ data were reduced using scripts
     written by Keller.

Analysis   ★ For §2.3, the script calculating equivalent widths
     was written by Da Costa.
  ★ For §3.3, Keller wrote a script to extract dereddened
     stars from 2°×2° regions from the SEKBO survey.
  ★ For §4.1, Keller used SEKBO data to estimate
     the RRL halo field contamination in the Sgr region.

Other   ★ Figure 2.1 was produced by Keller.

Publications   ★ The sections pertaining to the Virgo Stellar Stream
     were submitted to the Astrophysical Journal on 30th
     May 2008.

Sayuri L. Prior
August 2008

For my mother

Acknowledgements

Abstract

A subset of the RR Lyrae (RRL) candidates identified from the Southern Edge-worth-Kuiper Belt Object (SEKBO) survey data has been followed up photometrically ($n = 106$) and spectroscopically ($n = 51$). The spectroscopic targets are located in the Virgo Stellar Stream (VSS) region, a Sagittarius (Sgr) Stream region and in other apparent spatial clumps. Period and light curve fitting reveals a 24±7% contamination of SEKBO survey data by non-RRLs.

The first part of the thesis focuses on the VSS region, particularly on its extension to the south of the declination limits of the SDSS and of the QUEST RRL survey. The distribution of radial velocities in the Galactic standard of rest frame (V_{GSR}) for the 11 RRLs in the VSS region has two apparent peaks. The larger peak coincides with the four RRLs having $\langle V_{\mathrm{GSR}}\rangle = 127 \pm 10$ km s^{-1} and dispersion $\sigma = 27$ km s^{-1}, marginally larger than that expected from the errors alone. The two type ab RRLs in this group have $\langle[\mathrm{Fe/H}]\rangle = -1.95 \pm 0.1$ dex. Both the radial velocities and metal abundances are consistent with membership in the VSS. To further explore the spatial extent of the stream, luminosity functions have been constructed from the observed data and compared to data synthesised with the Besançon Galactic model. Analysis of the excess over the model predictions reveals the VSS as a large ($\sim$760 deg^2) overdensity centred at roughly (RA, Dec) $\sim$ (186°, −4°), spanning a length of $\sim$15 kpc in projection, assuming a heliocentric distance of 19 kpc. This data set provides the first opportunity to probe more southern regions of the stream and traces it to Dec $\sim$ −15° and Galactic latitudes as low as $b \sim 45$°.

The second part of the thesis focuses on suspected debris from the interaction of the Sgr dwarf galaxy with the Milky Way. The 21 type ab RRLs in this region have $\langle[\mathrm{Fe/H}]\rangle = -1.79 \pm 0.08$ dex, consistent with the age-metallicity relation of the Sgr body if the stars are part of the oldest population. The radial velocities appear non-normally distributed, with a prominent group having highly negative radial velocities ($\langle V_{\mathrm{GSR}}\rangle \sim -175$ km s^{-1}). Such velocities are predicted by a model of the interaction featuring an oblate dark halo potential. A number of stars cannot be fit to the simulated Sgr streams and are either contaminating halo field stars or are perhaps indicative of problems with the model distances. The possible association of RRLs in the VSS region with Sgr streams is also explored. Similar radial velocity trends with orbital longitude are seen in the simulated and observed data, pointing towards the association of the VSS region RRLs with the old trailing and leading streams. The best fits are obtained when the dark halo is modelled as oblate for the trailing stream and prolate for the leading stream. This result is consistent with previous findings and highlights the inability of any model to fit all the observational data. The need for further refinements to models is evident, with the consideration of an evolution of the orbital parameters of Sgr being a possible avenue of exploration.

Contents

List of Figures

List of Tables

Words are flowing out like
Endless rain into a paper cup
They slither while they pass
They slip away across the universe

Lennon & McCartney

1

Introduction

G alaxy formation is one of the outstanding problems in astrophysics (see Freeman & Bland-Hawthorn, 2002, and references therein). The progress made on this fundamentally important topic in the past few decades, however, has resulted in a drastic shift in our understanding. Whereas formation of a galaxy such as the Milky Way was once regarded as an event which took place in the distant past, it is now believed to be an ongoing process. This realisation has brought with it the exciting prospect of uncovering fossil evidence of how such a process might have unfolded. Indeed, recent years have seen the emergence of many tantalising clues to the complex and intriguing evolutionary history of our galaxy.

1.1 Structure of the Milky Way galaxy

Before elaborating on these clues and their relation to galaxy formation theories, it is useful to define the main structural components of the Galaxy. Like many other spiral galaxies, the Milky Way consists of a stellar bulge and flattened disk encased in a spheroidal stellar (baryon) halo and a dark halo (e.g. Bahcall & Soneira, 1980; Gilmore & Reid, 1983, see Figure 1.1). A brief description of these components will now be given, but the reader is referred to Freeman & Bland-Hawthorn (2002) for a more detailed account.

The *disk*, contributing about 90% of the Galaxy's visible light but only about 5% of its mass, actually consists of thin and thick disk subcomponents. The former
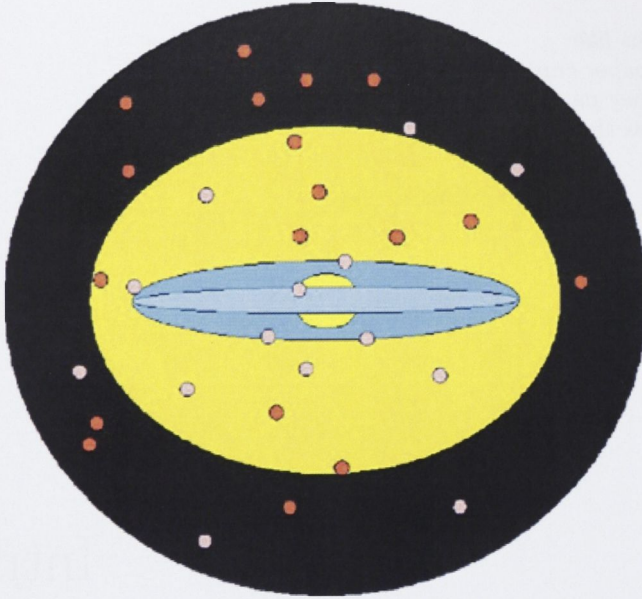
Figure 1.1: Schematic diagram of the Milky Way galaxy showing the stellar disk (light blue), thick disk (dark blue), stellar bulge (yellow), stellar halo (mustard yellow), dark halo (black) and globular cluster system (filled circles). Taken from Freeman & Bland-Hawthorn (2002).

has a vertical scale height of about 300 pc and is easily seen in other spiral galaxies viewed edge-on. The stars in the thin disk undergo rapid differential rotation and exhibit a wide spread in age (0–12 Gyr) and metallicity ($-0.5 <$[Fe/H]< 0.3). Thick disk stars, on the other hand, tend to be older and more metal poor ($-0.6 <$[Fe/H]< -0.4). It has been argued that, in contrast to the thin disk, the fainter thick disk is not always present in spiral galaxies and hence cannot be an essential element of galaxy formation (Freeman & Bland-Hawthorn, 2002). While it would clearly be desirable to study the thin disk in detail, the dissipation involved in its formation means that much of the information about the history of the protogalactic baryons is now irretrievable. However, research investigating possible surviving chemical signatures is showing considerable potential (De Silva et al., 2007).

Unlike the disk and the bulge, the *stellar* and *dark halos* are far more difficult to observe. In fact, as its name would suggest, the dark halo can only be detected through its gravitational influences. Dense, ancient globular cluster systems, along with various field stars, are dispersed throughout the halo which extends to a radius of at least 100 kpc. The stars in the halo, which account for only about 1% of the stellar mass of the Galaxy, are metal poor and their density is believed to fall off with increasing galactocentric radius according approximately to a $\rho \sim r^{-3}$ power law distribution (see Siegel et al., 2002, for a review of star count results), though this may depend on the particular stellar population studied (Chiba & Beers, 2000). There is also evidence that the inner halo may be considerably flattened while the

outer halo is more spherical (e.g. Preston et al., 1991; Chiba & Beers, 2000). The concept of a dual stellar halo has been further demonstrated with abundance and kinematic observational data (e.g. Carollo et al., 2007) and implications for galaxy formation are discussed below.

The halo is supported by its velocity dispersion and, unlike the disk, it has close to zero angular momentum. Of all the Galactic components, the stellar halo arguably presents the best opportunity for probing its formation for several reasons. Firstly, it contains the most metal poor stars and some of the oldest stars in the Galaxy. These stars can potentially provide information about the earliest periods of Galactic history. Secondly, orbital periods of stars in the halo are longer than in other components and hence structures have undergone less spatial and kinematic dissipation over their lifetimes. In addition, the Galactic potential is relatively smooth and slowly evolving in the outer regions. The remoteness and relative quiescence of the outer halo thus provides an ideal environment in which to search for preserved fossil records, which may remain for several gigayears (Bullock & Johnston, 2005). Moreover, as illustrated in §1.3.1, information gleaned from the stellar halo places constraints on the nature of the mysterious dark halo which accounts for at least 90% of the Galactic mass.

1.2 Galaxy formation

One of the traditional ways of conceptualising the Galaxy formation process was proposed in a seminal paper by Eggen et al. (1962; hereafter ELS). After observing a strong correlation between the metallicities and orbital eccentricities of a sample of halo field stars in the solar neighbourhood, ELS hypothesised a scenario in which the Galaxy was formed via a *rapid free-fall collapse of a relatively uniform, isolated pre-galactic cloud* on a timescale of 10^8 years. Although it is now known that the result was due to a selection effect, this paper was highly influential in illustrating that dynamical and abundance observations have great potential as tools for reconstructing galactic history. The specific galaxy formation theory, however, has since been challenged.

Based on the finding that globular clusters in the outer halo show no abundance gradient and exhibit a significant age range, Searle & Zinn (1978; hereafter SZ) were led away from the idea of a monolithic collapse and tentatively proposed that the Galactic halo was formed by a *prolonged, chaotic aggregation of independent, protogalactic fragments*. After years of debate, it is now generally accepted that at least part of the halo was indeed built up this way. On the theoretical front, this paradigm is consistent with the currently favoured Λ cold dark matter (ΛCDM) cosmological framework which postulates that galaxy formation is a consequence of

the hierarchical assembly of subgalactic dark halos and the subsequent accretion of cooled baryonic gas (e.g. Springel et al., 2006, and references therein). Elements of the ELS model may still apply, however, as SZ indeed assumed that the central regions formed through a collapsing process. This is in line with the findings of numerous researchers (e.g. Norris, 1994; Chiba & Beers, 2000; Carollo et al., 2007) who have noted a duality in properties such as the density, kinematics and age of halo field stars. Thus, a hybrid ELS-SZ model might be appropriate, with the inner halo forming through a dissipative collapse and the outer halo through dissipationless merging.

Although simulations based on CDM models are qualitatively successful in reproducing some of the properties of spiral galaxies (see Johnston et al., 2008, for a recent example), they are generally better able to predict structure on large scales than on galactic or subgalactic scales. One commonly noted problem lies in CDM's prediction of a significantly greater number of dark matter satellites than the number of dwarf galaxies observed to be orbiting the Milky Way (Klypin et al., 1999; Moore et al., 1999; Diemand et al., 2007). This has provoked considerable concern over the accuracy of CDM models and is referred to as the *missing satellite problem*. One proposed solution from the observational perspective is that there may exist satellites which are not completely dark but have not been detected due to their faintness or other observational biases (Mateo, 1998). Indeed, a number of ultra faint dwarf galaxy satellites have been discovered only in recent years (e.g. Belokurov et al., 2007b) using data from the Sloan Digital Sky Survey (SDSS; Adelman-McCarthy et al., 2008, and references therein). Although the new discoveries have alleviated the missing satellite problem somewhat, a discrepancy of a factor of ∼4 between observational data and CDM models remains (Simon & Geha, 2007). The potential discovery of further dwarf galaxies through the upcoming Stromlo Missing Satellites Survey with the SkyMapper telescope (Keller et al., 2007) could, however, bring the observations and simulations even closer together.

While satellite galaxies are certainly to be expected in an accretion scenario of galaxy formation, under certain circumstances the merging process could disrupt these systems to the extent that they become difficult to detect in position space. A prime example is the Sagittarius (Sgr) dwarf galaxy which, formerly hidden by foreground Milky Way stars, was discovered by Ibata et al. (1994) as a large group of stars sharing a common radial (i.e. line-of-sight) velocity. Indeed, it is expected that stars in systems which have been undergoing disruption over a long time period would no longer be highly confined in position space but would be identifiable on the basis of their phase space coherence (as illustrated in Figure 1.2). Other early examples of this principle are seen in the discoveries made by Majewski et al. (1994), identifying a coherent moving group of nine stars in the halo near the North Galactic Pole and Helmi et al. (1999), identifying eight stars clumped in 'integrals of motion' space (defined by two components of angular momentum).
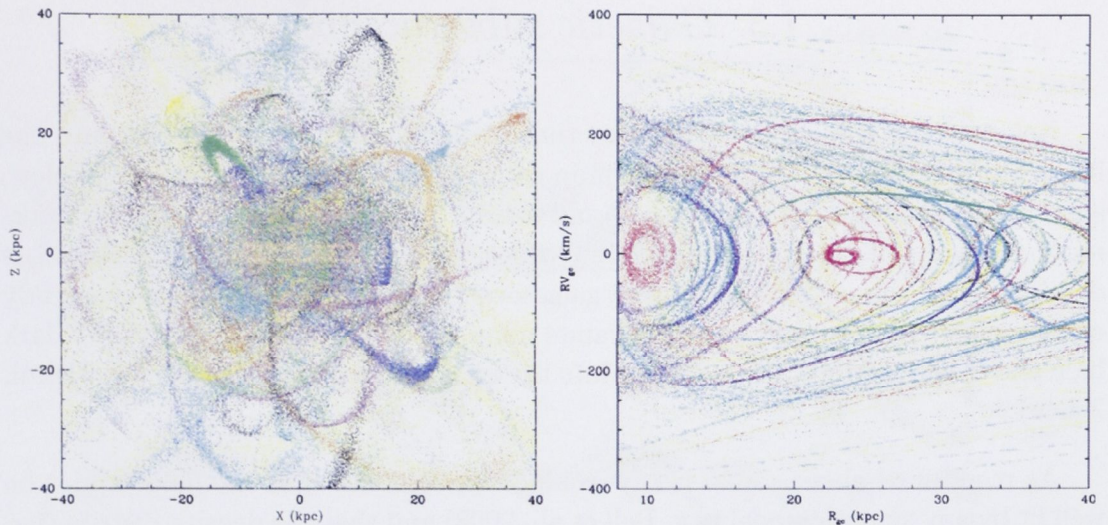
Figure 1.2: A simulation of a stellar halo built from the accretion of 100 satellite galaxies, with different colours representing the remnants of individual satellites. *Left:* Position space; *Right:* Phase space (radial velocity against orbital radius). We acknowledge P. Harding and H. Morrison for this figure. Taken from Freeman & Bland-Hawthorn (2002).

Since these small-scale studies, others have been undertaken in order to obtain a more comprehensive picture of the kinematical substructure in the halo, including the 'spaghetti' survey (Morrison et al., 2000), the APM carbon star survey (Ibata et al., 2001) and the SDSS (Adelman-McCarthy et al., 2008). While obtaining full space velocities for a comprehensive sample of halo stars awaits space missions such as Gaia (Perryman et al., 2001), as discussed further in Chapter 5, a profitable approach which is currently feasible is to identify possible substructures on the basis of spatial coherence and to confirm associations based on radial velocities of the potential members. Armed with such information, one can gain a clearer impression of the way and the extent to which the stellar halo deviates from a smooth halo (Bell et al., 2008) or from a simulated halo built up entirely from accretion events (Johnston et al., 2008). Johnston et al. found that, qualitatively, observations from the Milky Way and Andromeda galaxies are broadly consistent with simulated galaxies built within the context of ΛCDM. In further support of the notion of hierarchical aggregation of fragments, Bell et al. found that the amount of deviation of SDSS data from a smooth model was typical of simulated galaxies constructed entirely from disrupted satellite remnants. The evidence thus points to a scenario in which accretion plays a significant role in the formation of the Galaxy.

1.3 Galactic substructure

Not only can the study of substructure further inform investigations into the importance of the accretion mechanism in galaxy formation, but as reviewed below, spatial and kinematic data of clump and stream members can also provide information about the Galactic potential in which they move. Since the potential is dominated by the dark halo at large galactocentric radii, identification and study of halo substructures can place constraints upon the shape of the Milky Way's dark halo and consequently provide insight into the very nature of dark matter (see Helmi, 2004a).

As mentioned above, there is now compelling evidence that the halo cannot be well fit by any smooth model (e.g. Bell et al., 2008) and that the density distribution is highly affected by substructure at large radii. Supporting this notion of a clumpy halo is the observation that, while spatially smooth, the halo is lumpy in phase space coordinates at small radii (Morrison et al., 2008). In this section we discuss some of the Galactic substructure which has been observed to date, with particular emphasis on two very large contributors: the Sagittarius Stream and the Virgo Stellar Stream.

1.3.1 The Sagittarius Stream

The Sgr dwarf galaxy, located a mere 16 kpc from the Galactic centre, provides direct evidence of a system currently undergoing disruption. From the time of its discovery, the elongated morphology of Sgr, pointing towards the Galactic centre, has been taken as evidence for strong, ongoing tidal disruption (Ibata et al., 1994). A combination of observations have subsequently found the debris from the interaction to wrap around the sky (Majewski et al., 2003; Newberg et al., 2003; Belokurov et al., 2006), making it the most significant known contributor to the Galactic halo. Figure 1.3 shows Majewski et al.'s all-sky view of the Sgr debris from the Two Micron All Sky Survey (2MASS).

Since the discovery of the Sgr dwarf, many studies have reported detections of suspected Sgr tidal debris streams using various tracers including carbon stars from the APM survey (Totten & Irwin, 1998; Ibata et al., 2001), red clump stars from a pencil beam survey (Majewski et al., 1999), RR Lyrae stars from the SDSS (Ivezić et al., 2000) and from the Quasar Equatorial Survey Team (QUEST; Vivas et al., 2005), giant stars from the Spaghetti Project Survey (Dohm-Palmer et al., 2001), A type stars from the SDSS (Newberg et al., 2003) and M giants from the 2MASS (Majewski et al., 2003). Debris associated with Sgr has been found at various angles from the current position of the dwarf, as close as a few kpc from the sun (Kundu et al., 2002) and as far as the distant, outer reaches of the halo (Newberg et al.,
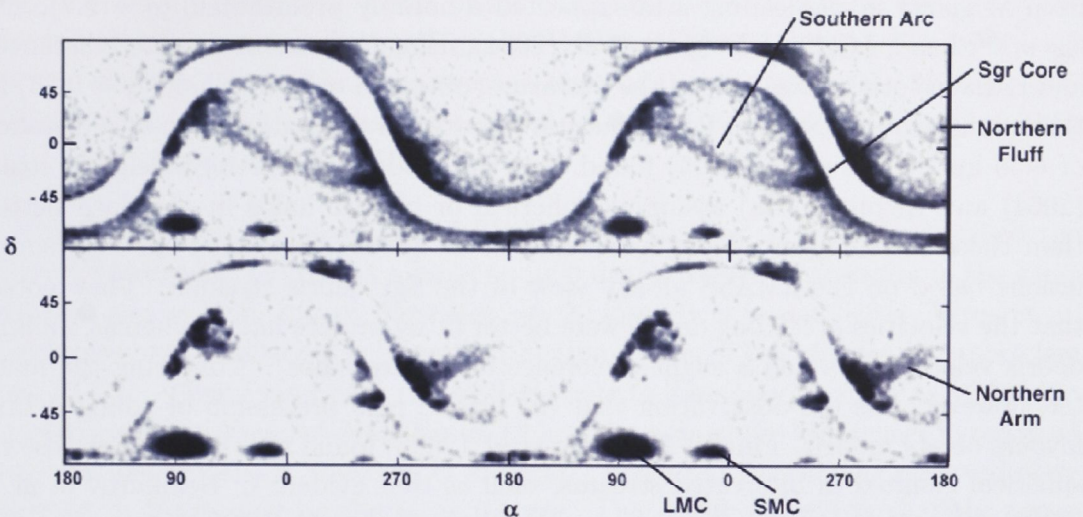
Figure 1.3: A smoothed, all-sky view of the Sgr debris from point sources in the 2MASS catalogue. Colour-magnitude selections for the top and bottom panels were chosen to optimise the signal from the southern arc and northern arm, respectively. Two cycles in RA (α) are shown to demonstrate the continuity of the features. Taken from Majewski et al. (2003).

2003). Some of the detections were hypothesised to be from older wraps, lost on pericentric passages several Gyr ago (Dohm-Palmer et al., 2001; Kundu et al., 2002).

The wealth of observational data has motivated several attempts at modelling the disruption of the Sgr dwarf and predicting the positions and radial velocities of the ensuing debris particles (e.g. Johnston et al., 1999; Ibata et al., 2001; Helmi & White, 2001; Martínez-Delgado et al., 2004; Law et al., 2005; Fellhauer et al., 2006). These models have resulted in estimates of the orbit pericentre and apocentre, Sgr's transverse velocity and current bound mass. In addition, several studies, considering the debris as test particles, have drawn conclusions about the shape of the Galactic halo potential. While Helmi (2004a) asserted that debris lost recently, such as M giant data in the trailing arm, was too young dynamically to provide any constraints on the shape of the dark halo potential, debris lost earlier has certainly been shown to discriminate between prolate (flattening $q > 1$), spherical ($q = 1$) and oblate ($q < 1$) shapes for the potential. For example, from the observation that the Sgr stream identified in their carbon star sample traces a great circle, Ibata et al. (2001) concluded that the halo must be almost spherical. Moreover, on the basis of N-body simulations, they subsequently constrained the mass distribution in the dark halo and concluded that it too was most likely spherical.

The issue of dark halo shape remains clouded, however, since a range of contrasting views have also been presented in recent years. Helmi (2004b) found that results

from M giants in the leading arm supported a notably prolate halo ($q = 1.7$). On the other hand, Martínez-Delgado et al. (2004), using the various reported distances and radial velocities available in the literature, obtained an oblate halo ($q = 0.85$) in their simulations. Based on RR Lyrae stars located in the leading arm at a distance of ~50 kpc, Vivas et al. (2005) found that the models of Martínez-Delgado et al. (2004) and Helmi (2004a) assuming spherical or prolate halos fit the data better than those assuming an oblate halo. Law et al. (2005) performed the first simulations based on the 2MASS all-sky view of the Sgr debris streams. They noted that the velocities of leading debris were better fit by prolate halos (whereas trailing debris velocity data had a slight preference for oblate halos). Confusing the matter, however, was the observation that the orbital pole precession of young debris favours oblate models. Finally, Fellhauer et al. (2006) found that only halos close to spherical resulted in bifurcated streams, such as that evident in Belokurov et al.'s (2006) analysis of upper main sequence and turn off stars in SDSS data.

The brief discussion above illustrates that the shape of the dark halo is a point of contention, with no model being capable of fitting all the available data. Law et al. (2005) propose that evolution of the orbital parameters of Sgr over several Gyr is needed to explain the results and suggest dynamical friction as the most likely mechanism to bring this about. They note that this would require Sgr to have been an order of magnitude more massive 2 Gyr ago and recognise the need to model the dwarf as a two-component system, with the dark matter bound less tightly than the baryons. They indicate that such a study is underway. Inclusion of additional, newly discovered samples of observed Sgr stream stars will no doubt help to more tightly constrain these improved models, particularly samples containing old stars which were lost several pericentric passages ago and which have been influenced by the Galactic halo potential for a longer time period. As we discuss below, RR Lyrae stars, used in the current study, are an excellent choice of tracer for this purpose.

1.3.2   *The Virgo Stellar Stream*

A number of other streams and groups have been identified in the halo. Examples include the Monoceros Stream (Newberg et al., 2002; Yanny et al., 2003) which surrounds the Galaxy in a giant ring (Ibata et al., 2003), and the Hercules-Aquila Cloud (Belokurov et al., 2007a) which extends above and below the Galactic plane and stretches ~80° in longitude. Another significant feature was discovered in QUEST data as an overdensity of RR Lyrae stars (Vivas et al., 2001, 2004; Vivas & Zinn, 2006), and in SDSS data as an excess of F-type main sequence stars (Newberg et al., 2002, 2007), in the direction of the Virgo constellation. QUEST, dubbing the feature the '12^h.4 clump', estimated its heliocentric distance as ~19 kpc, centred at RA ~ 186°. It was found to span RA ~ 175°–200° and the Dec range of the QUEST survey (−2.3°–0.0°). Subsequent radial velocity measurements

by Duffau et al. (2006) of a subset of the clump revealed a common velocity in the Galactic standard of rest frame (V_{GSR}) of 100 km s^{-1} and a dispersion of $\sigma = 17$ km s^{-1}, slightly smaller than the average error of the measurements. Using SDSS data, they estimated the feature to cover at least 106 deg^2 of sky and suggested the name 'Virgo Stellar Stream' (VSS).

Using photometric parallaxes of SDSS stars, Jurić et al. (2008) identified the 'Virgo Overdensity' (VOD) as a large ($\sim$1000 deg^2), diffuse overdensity in the same direction as the VSS, but at distances $\sim$6–20 kpc. In a recent paper, Vivas et al. (2008) provided additional information in this region of the sky for distances less than 13 kpc. They found that the VSS extends to distances as short as 12 kpc, in comparison to its previous detection at 19 kpc. In spite of the differences in reported distances and velocities, Newberg et al. (2007) suggested that all the observed overdensities in Virgo may be the same feature. The possibility exists that the terms may not be interchangeable, but for simplicity, this thesis hereafter refers to the feature as the VSS. The association of the VSS with Sgr debris was hypothesised by Martínez-Delgado et al. (2007) who showed that Law et al.'s (2005) model of the Sgr leading tidal tail passes through the region of the VSS. However, the model predicts highly negative radial velocities for Sgr stars in this region, contrary to the observations of Duffau et al. (2006) (see above) and Newberg et al. (2007) who find the most significant peak at $V_{\mathrm{GSR}} = 130 \pm 10$ km s^{-1}. The model also predicts a relatively low density of Sgr debris in this region which is at odds with the significance of the observed overdensity. Newberg et al. also note that the VSS is not spatially coincident with the main part of the Sgr leading tidal tail, but that the features do significantly overlap.

1.4 The current study

The previous section reviewed some of the substructures which have thus far been observed in the Galactic halo. All searches for substructure require the selection of an unbiased tracer population. The choice of RRL stars as the probe for the current project is now discussed.

1.4.1 RR Lyrae stars as tracers

RR Lyrae stars are radially pulsating variable stars in the core helium burning stage of their evolution and are found on the horizontal branch's instability strip in the Hertzsprung Russell (HR) diagram. They are characteristic of old (age > 10 Gyr) populations. Due to their similar core masses (about 0.5 solar masses), they exhibit a very small spread in absolute magnitude and they are thus deemed to

be standard candles. Their spectral classes range from late A to early F and they typically have a blue colour ($<V-R> \leq 0.4$). In the majority of cases, their periods are between 0.2 and 0.9 days, though the distribution within this range varies with subclass. Bailey type RRab stars have large amplitude variations of up to 1.5 mag and triangular light curves with a mean period of about 0.5 days. Type RRc stars, on the other hand, have more sinusoidal light curves with a lower amplitude of about 0.5 mag and a mean period of about 0.3 days.

It is thus apparent that RRL stars have many characteristics which make them very suitable probes of the halo. Not only are they relatively common (in local dwarf spheroidal galaxies, for example), but they are easy to recognise on the basis of their characteristic colours and patterns of variability which have relatively large amplitudes and short periods. Because they are standard candles, distances can easily be calculated from their apparent magnitudes, with high accuracy relative to other tracer populations. Moreover, by virtue of their intrinsic brightness, they can be seen to quite large distances in the halo compared to other tracers. This is particularly valuable for the purposes of the current study since substructure is more likely to survive in outer halo regions. Finally, since RRL stars are Population II stars, they provide a rare opportunity to trace ancient stellar populations which is clearly vital when attempting to unravel Galactic history.

Because their desirable properties as tracers have been known for many years, quite a number of surveys for RRL stars have been undertaken, pioneered by Shapley's (1939) search for variable stars in the Galactic halo. A historical review is provided by Wetterer & McGraw (1996). Recent years have seen the emergence of a number of surveys covering much wider areas to greater depth, significantly enhancing our view and knowledge of the halo. The sky coverage, number of candidates and maximum distance probed in recent wide-field surveys for RRLs, as summarised by Keller et al. (2008), are presented in Table 1.1. Some of the findings of these surveys as they pertain to Galactic substructure were discussed in the previous section. The current project utilises RRL data from the Southern Edgeworth-Kuiper Object (SEKBO; Moody et al., 2003) survey, which is fully described in Keller et al. (2008), in addition to follow-up photometry and spectroscopy. The data sets are described fully in §2.1.

1.4.2 Aims and outline

It is clearly an exciting time to be studying galaxy formation, with related research appearing in the literature at a prodigious rate. As various substructures continue to be discovered in the observational realm, modelling of halo buildup through accretion and of disruption of satellite galaxies is refined theoretically. A thorough understanding of the number, location and size of halo substructures is

Table 1.1. Wide-field surveys for RRLs (taken from Keller et al., 2008)

Survey Name	Sky Coverage (sq. deg.)	Number of Candidates	Maximum Distance (kpc)
QUEST	380	498	55
LONEOS-1	1430	838	30
Ivezić et al. (2000)	100	296	65
Sesar et al. (2007)	290	634	100
SEKBO survey	1675	2016	50

useful in order to make accurate comparisons and assessments of these models. In addition, the vast debris arms from the interaction of the Sgr dwarf galaxy with the Milky Way provide an enticing opportunity to study the distribution of dark matter in the Galaxy.

The discussion in §1.3.2 is only a brief summary of the findings relating to the overdensity in Virgo, but it highlights the considerable uncertainty that remains regarding its spatial form and origin. From the results of Belokurov et al. (2006) and Newberg et al. (2007), it is highly probable that the center of the VSS in fact lies to the south of the regions mapped by SDSS and QUEST. This region is covered by the SEKBO survey. Keller et al. (2008) produced a list of over 2000 RRL variable star candidates from this data set and analysed their spatial distribution. Among other overdensities, they identify two clumps in the region of the VSS. Clump 1, at a heliocentric distance of 16 kpc, is located $\sim 8°$ south-east of the VSS centre identified by Duffau et al. (2006), while Clump 2 is at a distance of 19 kpc and located $\sim 16°$ further to the south-east. The current study follows up a subset of these RRLs. In addition, clumps of RRL candidates in regions overlapping Sgr debris are also followed up.

Chapter 2 describes the target selection (§2.1.1) and data reduction procedures. Specifically, §2.1.2 describes the process of confirming the RRL classification of candidates while §2.2 and §2.3 describe the method of calculating radial velocities and metal abundances, respectively, from the spectra. Chapter 3 presents the results of these calculations for the RRLs in the VSS region and identifies possible members of the VSS on the basis of radial velocities (§3.1). To obtain further information regarding the spatial extent of the stream, a wider stellar population from the SEKBO survey data set is examined for signs of an excess of stars in the region of interest (§3.3). Chapter 4 is dedicated to the Sgr region. In §4.1, we compare the distances and radial velocities of confirmed RRLs in these regions to those predicted by the recent models of Law et al. (2005). In so doing, we investigate how the fits of the observed data to the models vary with shape of the dark halo. Further, by comparing

our VSS data with Law et al.'s models, we explore Martínez-Delgado et al.'s (2007) proposition that the VSS is in fact part of the Sgr debris stream. Metal abundances for Sgr region stars are presented in §4.2 and the potential use of luminosity functions is commented on in §4.3. Finally, Chapter 5 presents conclusions and briefly comments on future directions.

Images of broken light which
Dance before me like a million eyes
They call me on and on
Across the universe

Lennon & McCartney

2

Method

2.1 Observations and data reduction

T his chapter describes the general procedures used in the current project, including target selection, photometric and spectroscopic observations and reductions. The results as they pertain to the particular regions of interest are presented and discussed in Chapters 3 (VSS region) and 4 (Sgr region).

2.1.1 Target selection

Targets were selected from a list of 2016 candidates produced by Keller et al. (2008, hereafter KMP08) who searched the Southern Edgeworth-Kuiper Belt Object survey data for RRLs. The SEKBO survey was conducted on the 50″ telescope at Mount Stromlo Observatory between January 2000 and 2003 and covered a 10° wide band following the ecliptic (1675 deg^2 of imaging data). Two filters ('blue': 455–590 nm and 'red': 615–775 nm) were used simultaneously, with typically a set of three 300 s observations obtained, separated by ∼4 hrs and ∼1–7 days. In order to select candidates, KMP08 constructed a score that measured how well an object matched the expected properties of an RRL (i.e. in terms of its colour and variability). Their analysis showed that this procedure produced a candidate list with completeness for RRab ∼60% for $V < 18.5$, falling to 25% by $V = 19.5$.

The heliocentric radial distribution of RRL candidates from the SEKBO survey is

displayed in Figure 2.1. From this set of candidates, several apparent clumps of stars were targeted for follow-up. Firstly, as the SEKBO survey region overlaps that of the QUEST survey in the vicinity of the VSS, the possibility existed to not only recover previously identified VSS members, but also to gain further information regarding the spatial extent of the stream. A selection of the RRLs from the candidate list falling within the RA range 183°–192° and V_0 range 16.6–17.2 was targeted for observation ('VOD Clump 1' in KMP08). A second clump located at RA $\sim$ 206° at a similar distance was also targeted ('VOD Clump 2' in KMP08). In addition, apparent spatial groupings of stars at (RA, V) of $\sim$ (14 h, 16 mag), (16 h, 15 mag), (20 h, 17 mag), (21.5 h, 17 mag) and (0 h, 17 mag) were targeted. Note that the spatial position of the 20 and 21.5 h stars overlaps the expected position of the trailing arm of the Sgr debris stream.
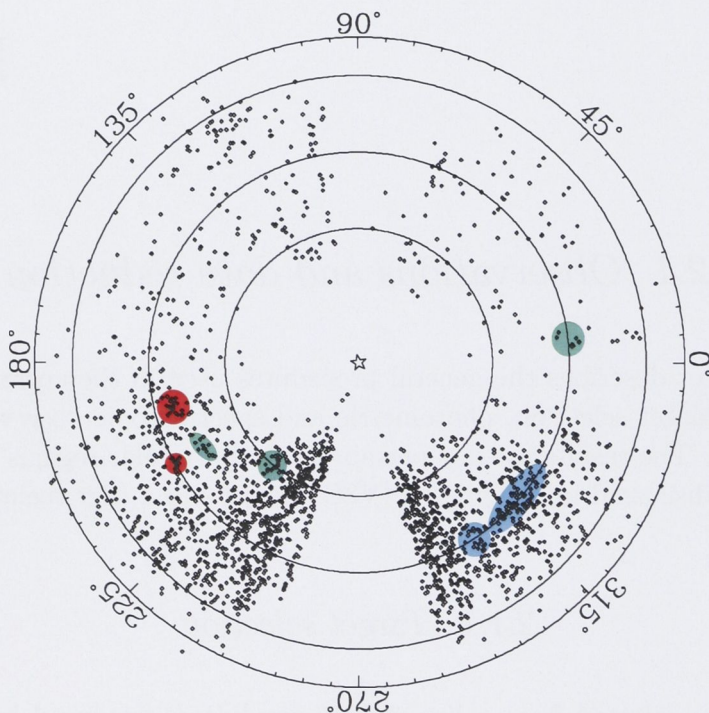
Figure 2.1: The heliocentric radial distribution of RRL candidates from the SEKBO survey in ecliptic longitude, λ (taken from KMP08, colour-coding added). The concentric circles are at V_0=15, 17 and 19. Shaded areas represent regions of apparent overdensity which were followed up in the current study. Red ($\lambda \sim$ 195° and 210°): VSS region; Blue ($\lambda \sim$ 305° and 315°): Sgr region; Green ($\lambda \sim$ 210°, 230° and 5°): 14h, 16 h, and 0 h regions.

In addition to the 51 RRLs from the clumps which were targeted for spectroscopic follow-up, a selection of a further 55 candidates over a wide range of RAs was targeted for photometric follow-up in order to elucidate the nature of the contamination of the SEKBO RRL candidate sample by non-RRLs. These targets varied in magnitude between $V = 15$ and 19.5. This set of targets included a selection of

Table 2.1. Target summary

	Number of Targets
PHOTOMETRY AND SPECTROSCOPY	
VSS:	
Clump 1 (12.4 h)	8
Clump 2 (14 h)	3
Sgr:	
Clump 1 (20 h)	5
Clump 2 (21.5 h)	21
Other clumps:	
14 h	3
16 h	6
0 h	5
Spectroscopy Total	*51*
PHOTOMETRY ONLY	
Contamination check:	
0 – 21.5 h	55
Photometry Total	*106*

'red' variable objects to investigate whether the adopted dereddened colour cutoff of $(V - R)_0 = 0.3$ for RRL candidates was appropriate. The number of spectroscopy and photometry targets in each region is summarised in Table 2.1.

2.1.2 Photometry

Observations were made with the Australian National University (ANU) 40″ telescope at Siding Spring Observatory (SSO) over six six-night runs between November 2006 and October 2007. The target was centred on one of the Wide Field Imager's eight CCDs. The *V* filter was used, with exposure times ranging from 120 to 600 s depending on the target magnitude. The total number of observations for each target over the observing runs ranged from 5 to 19, with an average of 9 observations per target (see Figure 2.2).

The data were overscan subtracted, trimmed, bias subtracted and flatfielded with twilight sky flats using standard IRAF procedures. Aperture photometry was then performed on each target as well as on an ensemble of nearby comparison stars, yielding an average differential magnitude for each target at each epoch. This series of differential magnitudes for the target was subsequently entered into Andrew Layden's period-fitting routine (Layden & Sarajedini, 2000, and references therein)
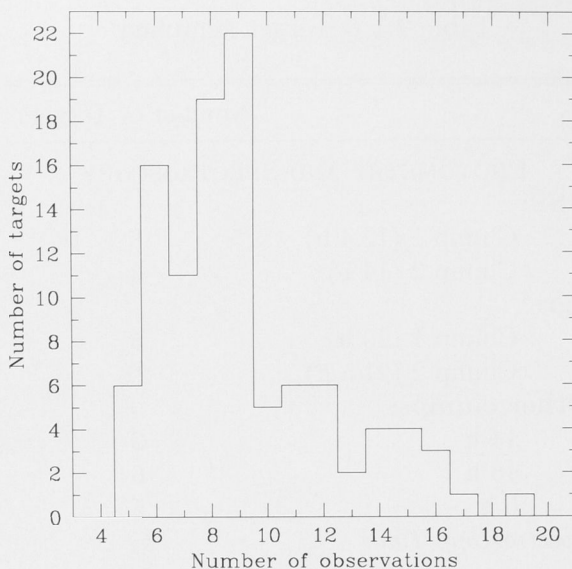
Figure 2.2: The distribution of number of observations for imaged candidates.

along with the mid-exposure heliocentric Julian dates of the observations. Layden's routine identifies the most likely period by fitting the photometry of the variable star with 10 templates (including 7 RRL templates) and performing a χ^2 minimisation. See Pritzl et al. (2002) for a more detailed description of the method. In addition to locating the period with the minimum χ^2 value, deciding on the best period also involved a certain amount of judgement. There was consideration of whether the periods and amplitudes were reasonable for RRLs of type *ab* or *c*, and light curves (using another routine by Layden) were also perused. Examples of good light curve fits are displayed in Figure 2.3.

One important application of the analysis of this photometry was to determine which candidates were indeed RRL stars and which were spurious detections. Of the 73 stars observed at least 8 times, 11 had magnitudes which did not vary significantly over the observations, 4 were classified as binary stars and 7 showed variability but did not appear to have periods and light curves corresponding to either RRLs or binary stars. Figure 2.4 shows the number of candidates falling into each classification category as a function of $(V - R)_0$.

Given that there are 51 RRLs and 16 non-RRLs within the colour selection, this indicates that the procedure KMP08 used to identify RRLs from the SEKBO survey data has a contamination rate of $24 \pm 7\%$, where the uncertainty has been calculated using Poisson statistics. Table 1 in the Appendix summarises the photometric data, including the classification, period and fitted V amplitudes (where applicable) for all targets.
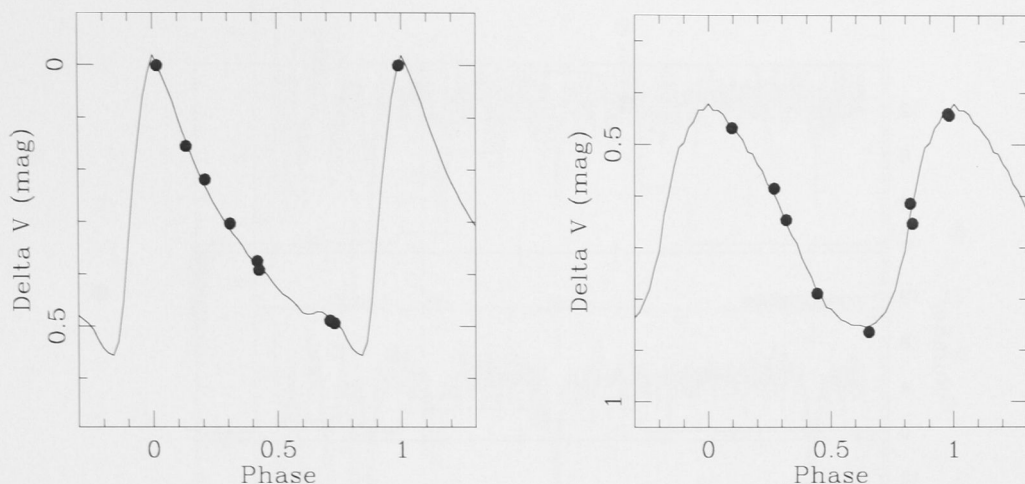
Figure 2.3: Phased V mag differences between a candidate and nearby comparison stars. From the tight fit of the data points to the template light curves *(solid line)*, we can be very confident that these two candidates are indeed RR Lyrae stars. *Left:* RR*ab* with period = 0.583 d. *Right:* RR*c* with period = 0.358 d.

2.1.3 Spectroscopy

Observations were made with the ANU 2.3 m telescope at SSO in runs that were concurrent with those on the 40″ telescope. The blue arm of the Double Beam Spectrograph was used with a 2″ slit and the 600B grating, giving a resolution of ~2 Å. The spectra were centred on 4350 Å so that the Ca II K line and Hydrogen lines such as Hδ, Hγ and Hβ could be observed. Exposure times were chosen to give a signal-to-noise of ~20 and varied between 900 and 3000 s. Each target was observed between one and four times, spread throughout a given observing run. Each observation was accompanied by a comparison Cu Ar lamp exposure. Radial velocity standards of similar spectral type were also observed for use as cross-correlation templates (see §2.2) as well as standards for Layden's (1994) pseudo-equivalent width system (see §2.3). A small number of bright RRLs from Layden (1994) were also observed to serve as additional cross-correlation templates.

The data were overscan subtracted and trimmed using standard IRAF procedures. Bias subtraction and flatfielding were not performed as they only served to add noise to the data. Wavelength calibration was performed over the range 3500–4965 Å using 4th–8th order legendre polynomials and 26–28 spectral lines, yielding dispersion solutions with RMS ~ 0.05 Å. Example spectra (after continuum fitting as described in §2.3) are displayed in Figure 2.5 and demonstrate the range in quality obtained.
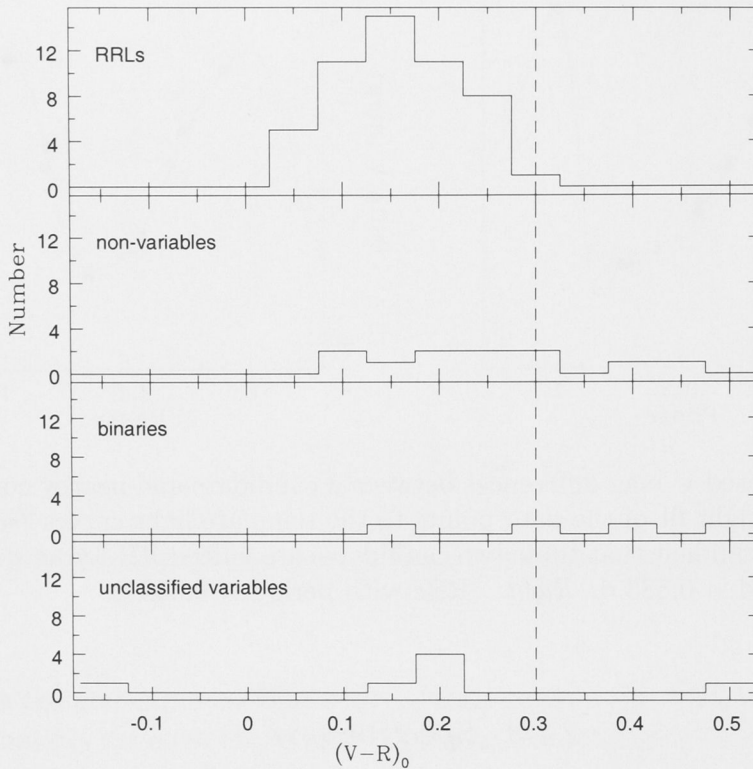
Figure 2.4: The classification of RRL candidates based on follow-up photometry. The dashed line indicates the adopted colour cutoff of $(V - R)_0 < 0.3$ for RRL candidates in the SEKBO survey.

2.2 Radial velocities

Radial velocities were determined using the IRAF task FXCOR which performs Fourier cross-correlations between spectra of the target star and chosen template stars. For each observing run, we chose 5–6 stars to use as templates from amongst the radial velocity standards and the bright RRLs from Layden (1994). The selection process was guided by the fact that relative velocities between template and target stars were most precise when the two stars were of similar spectral type. Subsequently, heliocentric corrections were made to remove the component of the observed velocity due to the Earth's motion around the Sun.

Observed radial velocities of an RR*ab* star can vary up to ± 50 km s^{-1} from its systemic velocity as a function of phase. In order to correct the observed velocities to systemic velocities we first determined the phase of each observation using the ephemerides based on the best period obtained from our photometric data. Layden's
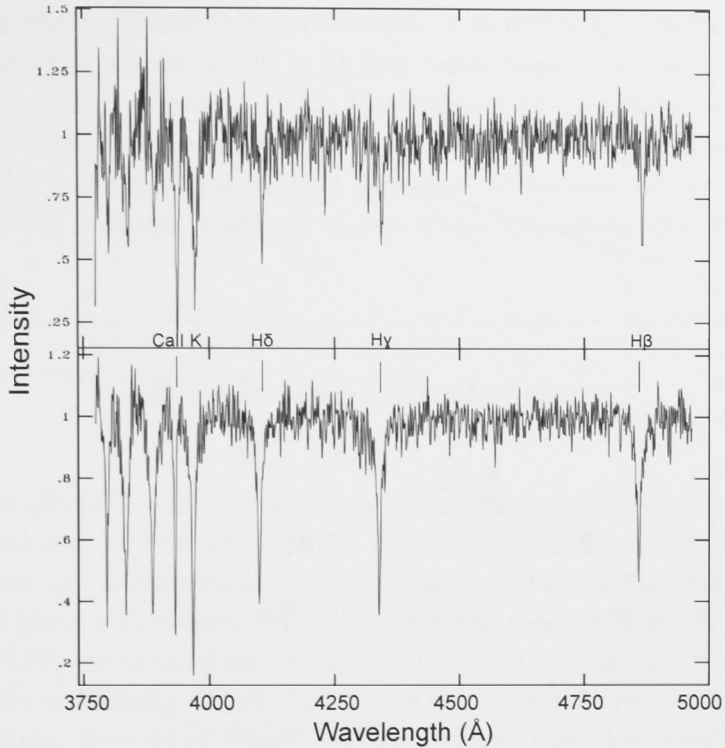
Figure 2.5: Examples of poor quality *(top)* and good quality *(bottom)* normalised spectra.

(1994) parameterisation of the velocity curve for the RRL star X Ari (measured by Oke (1966) from the Hγ line) was then used to determine the systemic velocity. Figure 2.6 shows example fits of the curve to our observed data. Based on X Ari, the systemic velocity is taken to occur at phase 0.5. Note that because the form of the discontinuity in the light curve near maximum light varies amongst RRLs, only phases between 0.1 and 0.85 were used in the fit. The average RMS of the fits was 18 km s^{-1}, which we use as an estimate of the uncertainty in the conversion from observed velocities to systemic velocities. We then combine this with the average uncertainty in the radial velocity zeropoints across the observing runs (± 7 km s^{-1}) and the uncertainty in the cross-correlations (± 4 km s^{-1}). The latter was quantified by calculating, for each observation, the standard deviation of the velocities obtained using the different templates, then averaging over all observations. The combination of these errors then yields an overall uncertainty in the systemic radial velocities of ± 20 km s^{-1}. For the two RRLs in common with Duffau et al. (2006), the velocities agree within the combined errors.

Of the 51 spectroscopic targets, 13 were type c RRLs. For these stars, velocity data for DH Peg and T Sex (Liu & Janes, 1989; Jones et al., 1988) were used to create a template velocity curve. However, given that the template yielded uncertainties in systemic velocities of up to 30 km s^{-1} when fitted to our data, we opted to instead
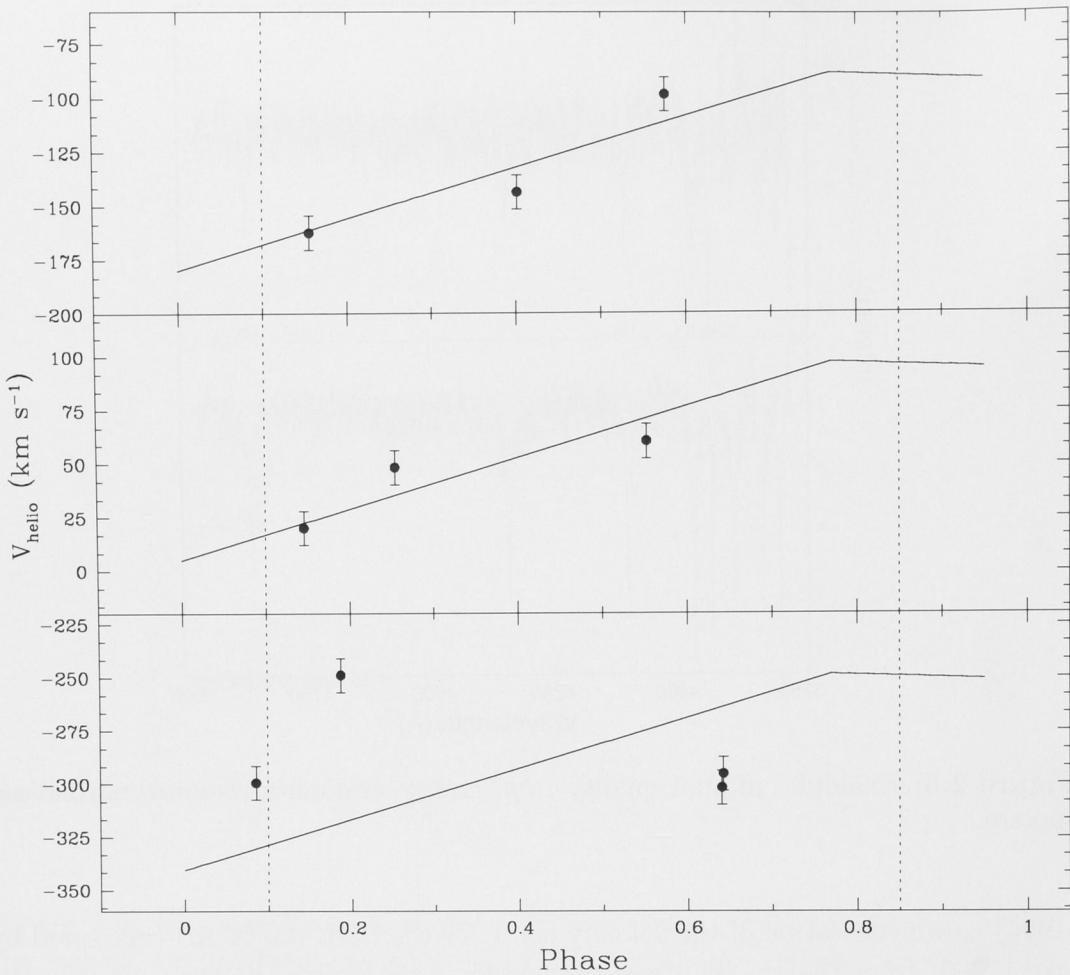
Figure 2.6: Fits of the radial velocity template of X Ari *(solid line)* to three type *ab* RRLs in our sample, each observed at three phases. The upper two plots are examples of excellent fits, while the lowest plot is an example of a poor fit. Note that data points with phase < 0.1 or phase > 0.85 are excluded in the fit. The systemic velocity corresponds to phase 0.5.

use the average radial velocity as our estimate of the systemic velocity. Taking into consideration the precision of our measurements and the fact that observed radial velocities of an RR*c* star at different phases only vary by up to ± 30 km s^{-1} from its systemic velocity, one would not expect a fit to a template curve to provide an improved constraint on the systemic velocity. This was indeed evidenced by the large scatter in the residuals of the template fit to the data as a function of phase. The average radial velocity was also used as an estimate of the systemic velocity for the four type *ab* RRLs having all observations at phases less than 0.1 or greater than 0.85. This non-optimal method likely produced inflated radial velocity uncertainties for these stars.

When investigating Galactic substructures, it is useful to consider radial velocities in a frame of reference which is at rest with respect to the Galactic centre. The heliocentric radial velocities (V_{helio}) calculated as described above were thus transformed to Galactic standard of rest frame velocities (V_{GSR}), thereby removing the effects of the Sun's peculiar motion (assumed to be $(u, v, w) = (-9, 11, 6)$ km s^{-1} with respect to the local standard of rest which has a rotation of 220 km s^{-1}).

2.3 Metal abundances

Metallicities ([Fe/H]) were calculated using the Freeman & Rodgers (1975) method which is an analogue of Preston's (1959) classic ΔS technique. In the Freeman & Rodgers method, metal abundance is determined by plotting the pseudo-equivalent width (EW) of the Ca II K line, $W(\text{K})$, against the mean EW of the Balmer lines, $W(\text{H})$. As the RRL varies in phase, it traces out a path on this plot which is strongly dependent on its metallicity. Thus, by using a calibration based on RRLs of known metallicity, we can determine [Fe/H] for our sample from low resolution spectra. Note that observations taken during rising light (phase ~ 0.8–1) should not be used since changes in the RRL's effective gravity and Balmer line profiles during this stage alter the relationship between $W(\text{K})$ and $W(\text{H})$. We have also omitted type c RRLs from the metallicity analysis since they are hotter and have weaker Ca II K lines than type ab RRLs. Lower signal-to-noise spectra and uncertainties in the contamination from interstellar Ca II K would thus result in larger uncertainties in the metallicities of type c RRLs compared to type ab.

The first step was to normalise our wavelength-calibrated spectra to unit intensity using IRAF's CONTINUUM task, which divides each spectrum by an appropriate polynomial. Subsequent steps closely followed the method described in Layden (1994). Eight of Layden's EW standard RRLs had been observed multiple times over the course of our observing runs. $W(\text{K})$ and the EWs of the Balmer lines Hδ, Hγ and Hβ were measured using numerical integration, with feature bands and continuum bands equal to Layden's wherever possible (see Table 2.2). Unlike Layden, however, the $W(\text{K})$ continuum bands were fixed for all reductions and our red continuum band for Hβ was truncated due to our smaller wavelength calibration range. Also note that all bands were offset by an appropriate wavelength shift according to the observed geocentric radial velocity of the star (described in §2.2). Finally, $W(\text{K})$ was corrected for contamination by the interstellar Ca II K absorption line (K_{int}) using the Beers (1990) model which has the form,

$$W(\text{K}_{\text{int}})\sin|b| = W_{\text{max}}(1 - e^{-|z|/h})$$

Table 2.2.　Feature and continuum band wavelengths (in Å)

Feature	λ_{feature}	Feature Band		Blue Contin. Band		Red Contin. Band	
		λ_{blue}	λ_{red}	λ_{blue}	λ_{red}	λ_{blue}	λ_{red}
Ca II K-narrow	3933.666	3927.	3941.	3908.	3923.	4019.	4031.
Ca II K-wide	3933.666	3924.	3944.	3908.	3923.	4019.	4031.
Hδ	4101.735	4092.	4112.	4008.	4060.	4140.	4215.
Hγ	4340.465	4330.	4350.	4206.	4269.	4403.	4476.
Hβ	4861.327	4851.	4871.	4719.	4799.	4925.	4950.

where b is the Galactic latitude, $|z|$ is the height above the Galactic plane, $W_{\text{max}} = 192 \pm 8$ mÅ and $h = 1081 \pm 112$ pc.

The measured equivalent widths for the standard RRLs are shown in Table 2.3 and offsets from Layden's values are displayed in Figure 2.7. It can be seen that our values agree well with Layden's for $W(\text{K})$, $W(\text{H}\delta)$ and $W(\text{H}\gamma)$ but that our values for $W(\text{H}\beta)$ are systematically smaller than Layden's. This was likely due to the use of a different red continuum band as mentioned above. A linear regression was performed to calculate the appropriate correction to bring our $W(\text{H}\beta)$ measurements in line with Layden's. The best fit is overplotted on Figure 2.7.

With the offsets to Layden's system in hand, the process of normalisation and measurement of EWs was repeated for the target RRLs. $W(\text{K})$, corrected for interstellar Ca II K, was plotted against $W(\text{H3})$, the average of the EWs of Hδ, Hγ and Hβ (offset to Layden's system). The metal abundance at a particular phase was then calculated using the relation

$$W(\text{K}) = a + bW(\text{H}) + c[\text{Fe/H}] + dW(\text{H})[\text{Fe/H}],$$

using the following coefficients, as determined by Layden (1994),

$$a = 13.858; \quad b = -1.185; \quad c = 4.228; \quad d = -0.320,$$

yielding an external precision for [Fe/H] of 0.15–0.20 dex. Finally, averaging over the [Fe/H] values at the observed phases then yielded the final value of [Fe/H]. The internal precision was estimated by noting the difference in [Fe/H] values at each phase for an RRL which was observed at similar phases (see §3.2 and §4.2).
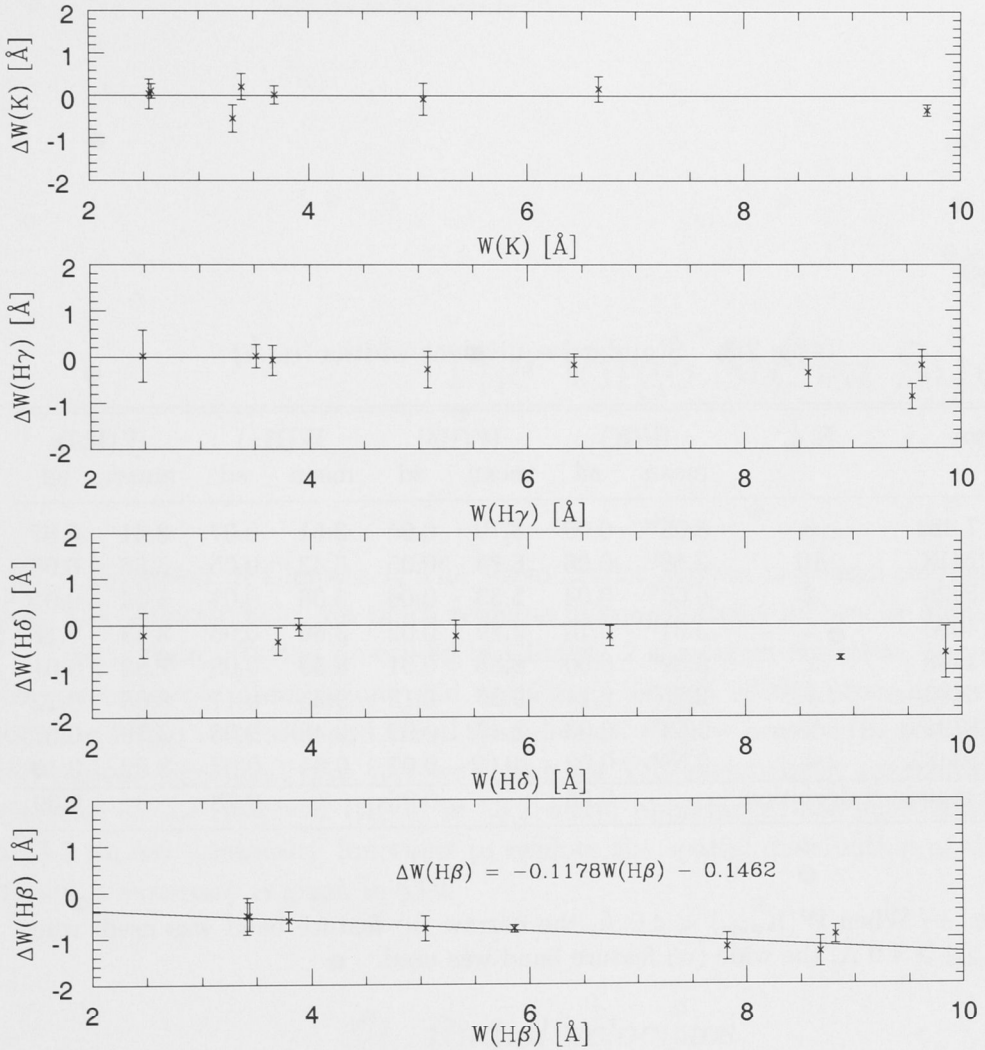
Figure 2.7: Differences between pseudo-equivalent widths (*top to bottom:* $W(\mathrm{K})$, $W(\mathrm{H}\gamma)$, $W(\mathrm{H}\delta)$, $W(\mathrm{H}\beta)$) in the current study and those of Layden (1994) for eight EW standard stars. Negative ΔW values indicate that our EWs are smaller than those of Layden. Error bars are the standard deviations of our repeated measures of the EWs (see Table 2.3 for details). No appreciable difference was noted for $W(\mathrm{K})$, $W(\mathrm{H}\gamma)$ or $W(\mathrm{H}\delta)$ (horizontal line drawn at $\Delta W = 0$ for reference) but a negative linear relationship was noted for $W(\mathrm{H}\beta)$, as shown by the solid line in the lowest plot.

Table 2.3.   Standard equivalent widths (in Å)

Star	N_{obs}	$W(K)$		$W(H\delta)$		$W(H\gamma)$		$W(H\beta)$	
		mean	sd	mean	sd	mean	sd	mean	sd
BD-17 484	8	5.05^w	0.09	3.70	0.05	3.51	0.07	3.41	0.07
HD 22413	10	3.69^n	0.05	6.75	0.05	6.43	0.05	5.86	0.06
HD 65925	2	6.66^w	0.04	5.33	0.06	5.08	0.07	5.04	0.01
HD 74000	4	3.31^n	0.10	3.89	0.02	3.66	0.06	3.43	0.17
HD 74438	2	3.39^n	0.00	8.88	0.01	8.59	0.08	7.82	0.01
HD 76483	7	2.55^n	0.11	9.85	0.13	9.55	0.17	8.68	0.22
HD 78791	2	9.69^w	0.03	2.47	0.07	2.48	0.06	3.79	0.07
HD 180482	4	2.57^n	0.02	10.02	0.07	9.64	0.07	8.82	0.10
mean standard deviation			0.06		0.06		0.08		0.09

Note. — When $W(K_{wide}) < 4.0$ Å, the narrow (n) feature band was used; when $W(K_{wide}) \geqslant 4.0$ Å, the wide (w) feature band was used.

Thoughts meander like a
Restless wind inside a letter box
They tumble blindly as
They make their way across the universe

Lennon & McCartney

3

The Virgo Stellar Stream

As discussed in Chapter 1, The Virgo Stellar Stream is a large overdensity in the Galactic halo, yet much remains unknown about its precise spatial form and origin. Having described in Chapter 2 the target selection, photometric and spectroscopic observations and reductions as well as the procedures used to calculate radial velocities and metal abundances, we now present the results for the VSS region. Specifically, in §3.1 we search for VSS members by examining radial velocities of the observed RRLs, in §3.2 metal abundances are investigated, and in §3.3 we use luminosity functions to explore the spatial distribution of the VSS. Finally, a summary is given in §3.4.

3.1 Radial velocities

The spatial distribution and V_{GSR} of observed RRLs in VSS Clumps 1 and 2 are displayed in Figure 3.1 (details are also given in Table 3.1). Distances are based on the assumption of $M_V = 0.56$ and have an uncertainty of $\sim 7\%$, as described in KMP08. This corresponds to an uncertainty of approximately ± 1 kpc at a distance of 20 kpc. RRLs observed spectroscopically by Duffau et al. (2006) (hereafter DZV06) and classified as VSS members are also included on the Figure to show the region where the VSS was detected. The four magenta points have 40 km s^{-1} < V_{GSR} < 160 km s^{-1}, the range within which DZV06 classified RRLs as members of the VSS. One star has previously been associated with the VSS by DZV06 while the remaining three proposed members are new discoveries. They would suggest

that the stream spans a much larger declination range than previously estimated. The four members have $\langle V_{\rm GSR} \rangle = 127 \pm 10$ km s^{-1} and dispersion $\sigma = 27$ km s^{-1} which is only slightly larger than the measurement error of ± 20 km s^{-1}. Our value of $\langle V_{\rm GSR} \rangle$ is somewhat higher than DZV06's value of 100 ± 8 km s^{-1} and is in better agreement with Newberg et al.'s (2007) value of 130 ± 10 km s^{-1}.
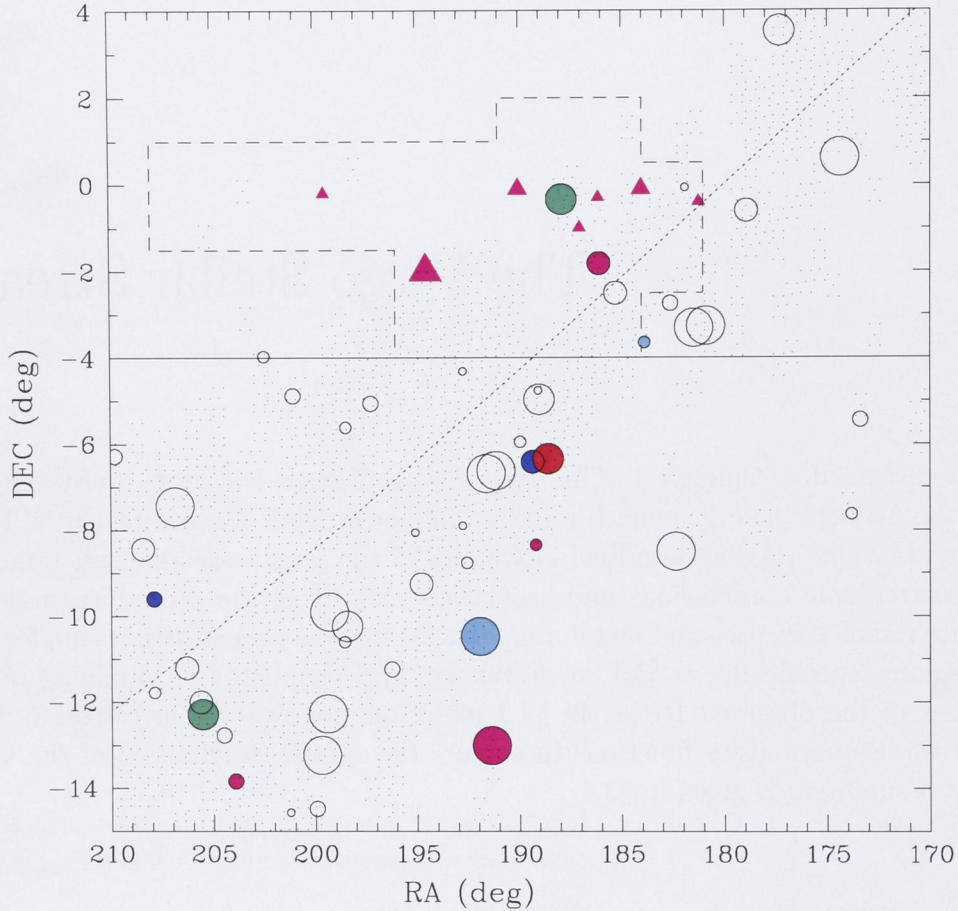
Figure 3.1: The spatial distribution of RRL candidates from the SEKBO survey *(circles)* and QUEST RRLs found to be VSS members *(triangles)*. Symbol size represents distance, ranging from 16 kpc *(largest)* to 22 kpc *(smallest)*. Filled circles were observed spectroscopically and are colour-coded according to $V_{\rm GSR}$. *Blue:* less than -160 km s^{-1}; *Cyan:* -160 to -40 km s^{-1}; *Green:* -40 to 40 km s^{-1}; *Magenta:* 40 to 160 km s^{-1} and *Red:* greater than 160 km s^{-1}. The dotted line is the ecliptic and the small dots represent the coverage of the SEKBO survey fields in this part of the sky. The dashed box is the region where Duffau et al. (2006) identified the VSS as an excess of main-sequence stars of appropriate apparent magnitude. The approximate southern limit of SDSS data in this region is shown by the solid line at Dec $= -4°$.

Table 3.1. Spectroscopic data summary for 14 h, 16 h, 0 h and VSS regions

ID	RRL type	systemic vel. calculation	n_{vel}	V_{helio} (km s^{-1})	V_{GSR} (km s^{-1})	$n_{Fe/H}$	[Fe/H]
VSS region							
96102-170*+	ab	fit	2	230	128	3	−2.15
105648-222	ab	fit	1	−91	−162	1	−1.45
107552-323	ab	fit	3	302	193	3	−1.34
108227-529	c	average	1	−8	−119	-	-
109247-528	c	average	2	113	28	-	-
119827-670	ab	fit	2	−84	−192	2	−1.68
120185-77+	ab	fit	2	94	1	2	−2.38
120679-336*	ab	fit	3	204	91	2	−1.74
120698-392*	c	average	1	227	134	-	-
121242-188*	c	average	3	276	155	-	-
121194-205	c	average	1	−39	−152	-	-
14 h, 16 h, and 0 h regions							
97890-199	c	average	2	367	285	-	-
106586-211	ab	fit	2	−5	−33	2	−1.52
114421-242	ab	fit	1	−51	40	1	−2.30
120857-475	ab	fit	1	191	100	1	−2.24
121817-2385	ab	fit	2	3	−33	1	−1.87
121906-2336	c	average	2	40	−2	-	-
122112-595	ab	fit	1	−134	−168	1	−1.42
122156-1114	c	average	2	−42	−81	-	-
122214-1315	ab	fit	1	24	−14	2	−1.96
122240-33	ab	average	2	121	21	1	−2.01
127008-210	ab	fit	2	−3	78	2	−0.96
127806-85	ab	fit	1	−187	−102	1	−2.63
127806-438	c	average	3	−165	−80	-	-
128416-544	ab	fit	2	−309	−192	2	−2.19

Note. — Proposed VSS members are marked by *; QUEST stars are marked by +

Figure 3.2 is a generalised histogram of V_{GSR} in which each observed value is represented by a normal distribution with mean equal to the observed value and standard deviation comparable to the uncertainty in the measurement. Summing probability density distributions over all observations then yields an estimate of the true distribution of V_{GSR} which, unlike in standard histograms, does not vary according to binning choice. A random selection of halo stars is expected to have a normal distribution of radial velocities (e.g. Harding et al., 2001) with a mean of ~ 0 km s^{-1} and a standard deviation of ~ 100 km s^{-1} (e.g. Sirko et al., 2004; Brown et al., 2005) (dotted line on Figure 3.2). Our data does not fit the expected distribution well, though the difference did not reach statistical significance in a Kolmogorov-Smirnov test presumably due to the small sample size.
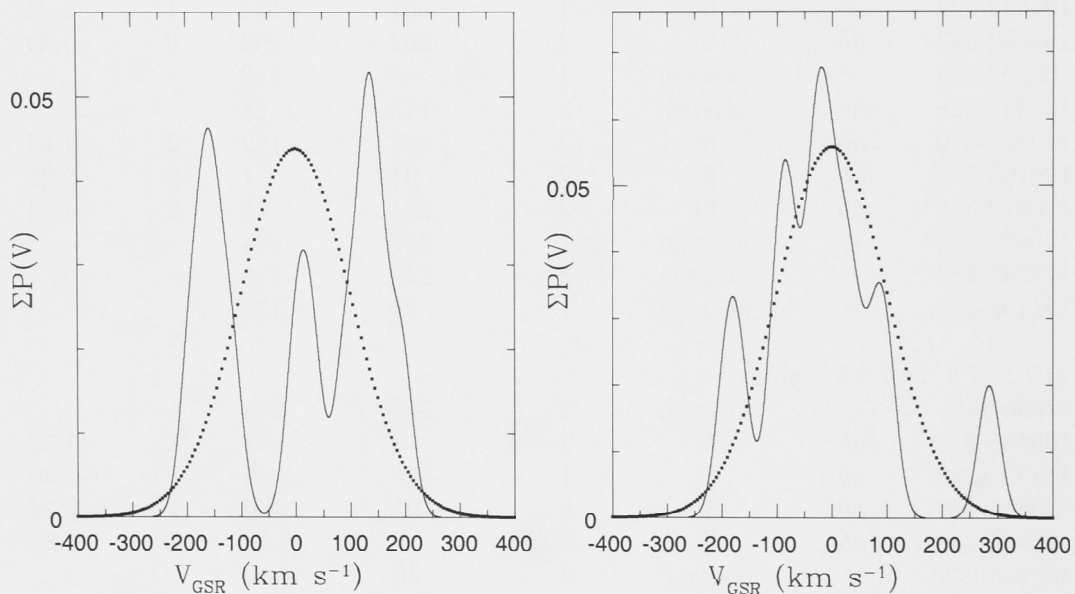
Figure 3.2: Generalised histogram of V_{GSR} (with kernel of 20 km s^{-1}) for the eleven observed RRLs in the VSS region *(left)* and for the fourteen RRLs in the 14 h, 16 h, and 0 h regions *(right)*. Overplotted *(dotted line)* is the expected distribution of V_{GSR} given a halo population in which velocities are normally distributed with $\langle V_{GSR} \rangle = 0$ km s^{-1} and $\sigma = 100$ km s^{-1}. The VSS can be seen in the left panel as the excess of stars at $V_{GSR} \sim 130$ km s^{-1}, while the excess at $V_{GSR} \sim -170$ km s^{-1} could potentially be related to the Sgr debris.

On visual inspection, however, there is a suggestion of a peak at ~ 130 km s^{-1} (VSS members) and another at ~ -170 km s^{-1}. The three stars contributing to the latter peak are in the same region as a peak identified by Newberg et al. (2007) with $V_{GSR} = -168 \pm 10$ km s^{-1} at (RA, Dec) $= (191°, -8°)$. They did not suggest an association for this peak, but it has an appropriate V_{GSR} to be part of the Sgr leading tidal tail, which is expected to have a highly negative radial velocity at this RA (e.g. see modelling by Law et al., 2005). However, debate currently surrounds

the question of whether Sgr debris, coming from the north Galactic pole to the solar neighbourhood, is in fact densely located in this region (Martínez-Delgado et al., 2007; Newberg et al., 2007). Newberg et al. do concede, however, that the VSS and Sgr streams overlap, so while the Sgr debris is not expected to be dense enough in this region to account for the entire overdensity in Virgo, it seems plausible that a portion could be attributed to Sgr debris. Further analysis and discussion of the possible association of stars in the VSS region with Sgr streams is deferred to §4.1.

No groupings of velocities were noted in the apparent spatial clumps at 14 h, 16 h, and 0 h, though it should be noted that the small sample sizes might have made any moving groups difficult to detect. We note, however, that the V_{GSR} distribution of RRLs in these regions (see the right panel of Figure 3.2) more closely resembles the expected normal distribution of halo stars than does the distribution of RRLs in the VSS region.

3.2 Metal abundances

The values of [Fe/H] for the 16 type *ab* RRLs in the 14 h, 16 h, 0 h, and VSS regions are listed in Table 3.1 and their distribution is shown in Figure 3.3. These values were calculated by averaging over the values obtained at each phase (plotted in Figure 3.4). The internal precision of the final [Fe/H] values was estimated as 0.17 dex by noting the difference in [Fe/H] values at each phase for an RRL which was observed at similar phases (0.4 and 0.56). Averaging across the sample, $\langle[Fe/H]\rangle=$ -1.86 ± 0.1 with a dispersion $\sigma = 0.45$ dex (see Figure 3.3). This value is somewhat more metal poor than the previously reported value $\langle[Fe/H]\rangle= -1.61\pm0.06$, $\sigma = 0.4$ dex, for RRLs in the halo (Kinman et al., 2000). The two proposed VSS members (the other two members were type *c* RRLs for which metallicities could not be calculated) have $\langle[Fe/H]\rangle= -1.95 \pm 0.1$ on our [Fe/H] system and an abundance range of $\sim 0.4 \pm 0.2$ dex. These values agree with $\langle[Fe/H]\rangle_{VSS} = -1.86 \pm 0.08$, $\sigma = 0.40$ dex found by DZV06. This supports our claim that these stars are part of the stream. The two type *ab* RRLs contributing to the negative V_{GSR} peak which may be associated with Sgr debris (see Figure 3.2) have $\langle[Fe/H]\rangle= -1.57 \pm 0.1$ and an abundance range of 0.2 ± 0.1 dex.
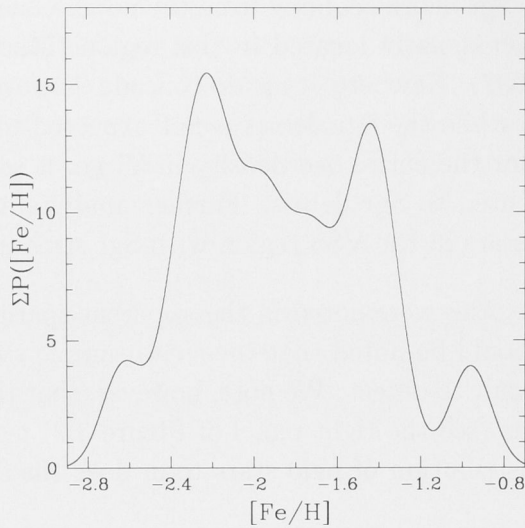
Figure 3.3: Generalised histogram of [Fe/H] (with kernel of 0.1 dex) for the 16 type *ab* RRLs in the 14 h, 16 h, 0 h, and VSS regions.
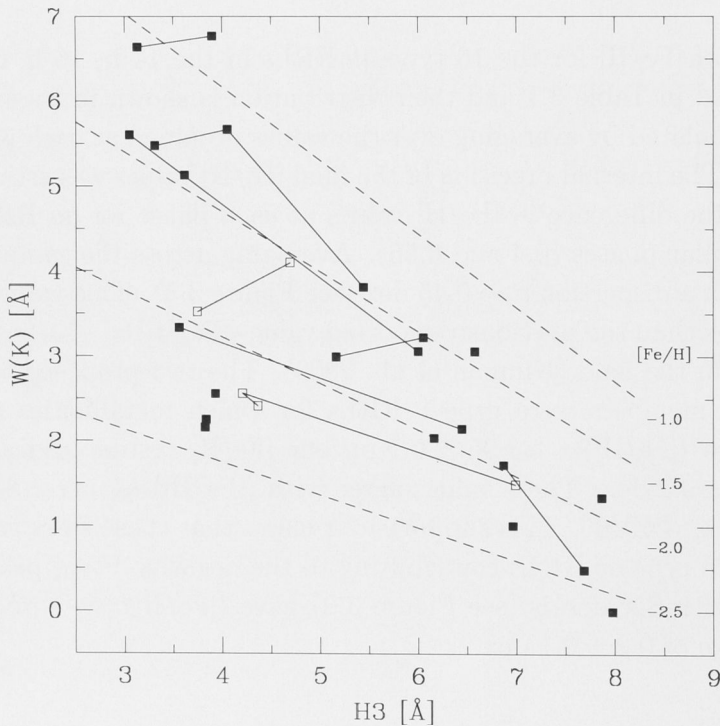
Figure 3.4: The pseudo-equivalent width of the Ca II K line, corrected for interstellar absorption, against the average width of Hδ, Hγ and Hβ for the 16 type *ab* RRLs in the 14 h, 16 h, 0 h and VSS regions. Solid lines connect values for the same RRL observed at different phases. The dashed lines are the loci of stars having the indicated [Fe/H] value according to Layden's (1994) calibration. The two hypothesised VSS members are plotted as open squares.

3.3 Luminosity functions

Having discovered three RRLs with radial velocities and metal abundances consistent with the VSS yet falling outside the VSS region identified by DZV06, it was of interest to further explore the spatial extent of the stream by now examining a broader stellar population. We selected 49 $2° \times 2°$ regions spread over RA 125–220° with the aim of sampling the area roughly evenly, given the constraints of the actual field locations (see Figure 3.5). Colour-magnitude diagrams (CMDs) and luminosity functions (LFs) were constructed from the SEKBO data (examples are shown in Figure 3.6) and examined for signs of an upturn near the magnitude where the subgiant branch and the main sequence merge. For an old population, this occurs at $M_V \sim 3.5$ which corresponds to $V \sim 19.9$ at a distance of 19 kpc (the average distance of the four identified VSS members, consistent with the findings of Newberg et al., 2002, and DZV06). This technique was also used by DZV06, where the target region was compared to a control region of equal area. Given the difficulty in identifying a suitable control region when the spatial extent of the VSS is unclear, we opted instead to compare the observational data to synthetic data produced by the Besançon model of Galactic stellar populations (Robin et al., 2003). This model comprises four components: thin disk, thick disk, halo and bulge. It is a smooth, dynamically self-consistent model where parameters are forced to follow physical laws, taking into account physical links between density, velocity and metallicity distribution.

The simulations covered a distance interval of 0–120 kpc and assumed an average V band interstellar extinction coefficient of 0.75 mag kpc^{-1}. This value was chosen so that the average integrated line-of-sight extinction was in agreement with those derived using the dust maps of Schlegel et al. (1998) and it is close to the value suggested by Robin et al. (2003) for intermediate to high galactic latitudes (the region studied here covers $30° \lesssim b \lesssim 60°$). Initial cuts in magnitude ($13 < V < 22$) and colour ($-0.5 < V - R < 1.5$) were made. In order to omit local red dwarfs and focus more clearly on the population of interest, only stars with $(V - R)_0 < 0.7$ were included in the luminosity functions. Since the simulated colour interval greatly exceeded the observational colour errors, the simulations were not convolved with photometric errors. Similarly, completeness of the observations was not incorporated into the simulated data since our analyses would focus on stars brighter than the observational incompleteness limit.

Equatorial coordinates of the regions simulated were identical to those of the chosen observed regions (with a step size of 1° in both RA and Dec), however, areas were not equal due to the non-uniform sampling of the SEKBO survey (see the small dots in the righthand panel of Figure 3.5). In order to compare the LFs, we thus normalised the synthetic data to the observed data based on counts in the range

$14.7 < V_0 < 16$. As an example, Figure 3.6 shows CMDs and LFs for three regions. In the upper panel, a clear excess of observed stars over synthetic stars can be seen for $V_0 > 16.5$, peaking at $V_0 \sim 19.5$. It should be noted that incompleteness becomes a significant factor by $V = 19$ and thus the excess may well continue to grow to fainter magnitudes. In this particular region, two excesses are apparent in the CMD for stars fainter than $V \sim 19$. One has $(V - R)_0 \sim 0.35$ while the other is redder, with $(V - R)_0 \sim 0.6$. These excesses possibly correspond to the top of the main sequence and the lower giant branch, respectively. We verified that the excess in the luminosity function is still present using a bluer cutoff, $(V - R)_0 < 0.5$, and thus the excess is not driven solely by the redder stars. In the middle panel, the overall

Figure 3.5: The spatial distribution of regions in which data was compared to the Galactic stellar distribution model. The significance of the excess of data stars over synthetic stars is represented by the colouring of the region according to the scale shown, with darker shades indicating a more significant excess. The range of magnitudes included in the excess calculation was $V_0 = 16.25$ to *(left panel, top to bottom)* 18.25, 18.75, 19.25 or *(right panel)* 19.75. Also shown are the four stars from our sample with V_{GSR} consistent with the VSS *(cyan asterisks)* and those found by DZV06 in QUEST data *(red crosses)*. The example regions in Figure 3.6 are circled in yellow. As in Figure 3.1, the red dashed box is DZV06's identification of the VSS region. The dashed line represents the ecliptic and the solid lines outline the broad limits of the SEKBO survey, with small dots showing the centres of the fields surveyed.
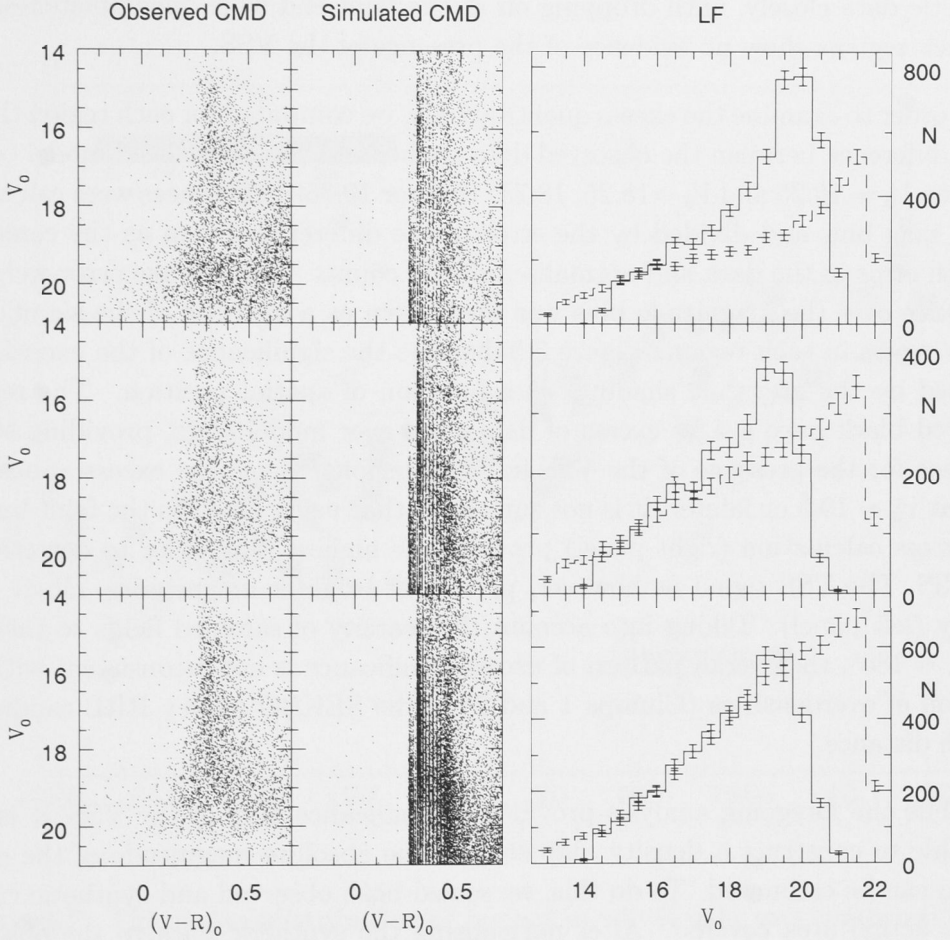
Figure 3.6: *Left panel:* Example CMDs from observed data for $2° \times 2°$ (non-uniformly sampled) regions (see yellow circles on Figure 3.5 for spatial locations). *Middle panel:* Corresponding CMDs for synthetic data using the Bescançon model (Robin et al., 2003), not convolved with completeness or photometric errors. Note that the areas have not been normalised in constructing the CMDs. *Right panel:* Luminosity functions for observed *(solid line)* and synthetic data (normalised over $14.7 < V_0 < 16$; *dashed line*) in each region for stars with $(V - R)_0 < 0.7$. Poisson error bars are shown. The field in the top panel (RA $\sim 178°$) shows a large excess of stars in the data compared to the model, providing strong evidence for the presence of the VSS. The field in the middle panel (RA $\sim 192°$) shows a weaker excess, while the field in the bottom panel (RA $\sim 218°$) shows no excess.

excess is smaller, becoming noticeable only at $V_0 \sim 17.5$ and apparently peaking at $V_0 \sim 19$ before incompleteness sets in. There is thus some evidence for the VSS in the region represented in the middle panel and evidence for a strong signal in the region represented in the top panel. The data in the bottom panel follows the synthetic data closely, until dropping off at the faint end when incompleteness sets in. Such regions show no evidence of the presence of the VSS.

In order to examine the excess quantitatively, we computed for each region the average difference between the observed data counts and the normalised model counts between $V_0 = 16.25$ and $V_0 = 18.25$, 18.75, 19.25 or 19.75. Differences were calculated in 0.5 mag bins and divided by the error in the difference, taken as the combined Poisson error in the data and normalised model counts. The average error-weighted difference over the magnitude bins was then taken as a measure of the significance of the excess in each region. Figure 3.5 displays the significance of the excess, represented by the greyscale shading, as a function of spatial position. The regions coloured black have a 4.5σ excess of data stars over model stars, providing strong evidence for the presence of the VSS in those regions. Since the excess appears to peak at $V_0 \sim 19.5$ or fainter, it is not surprising that using 19.75 as the faint limit of the excess calculation (right panel) provides the highest sensitivity to detection of the VSS. The VSS signal is, however, present at brighter magnitudes, albeit more weakly (left panel). Taking into account the scarcity of sampled fields to the west of RA $\sim 180°$, the overall pattern of excess significance is not inconsistent with the location of overdensities (Clumps 1 and 2) of the SEKBO survey RRL candidates at this distance.

While the foregoing analysis provided a significance map of the VSS, it is also desirable to construct a density map so that the absolute magnitude of the entire stream can be estimated. To do this, we scaled both observed and synthetic counts by the actual area covered. After normalising the synthetic data to the observed data based on counts between $14.7 < V_0 < 16.0$ and subtracting synthetic data from observed data, we then had a measure of the excess number of stars per square degree in each 0.5 mag bin between $V_0 = 16.25$ and 19.75. This excess number, summed over magnitude, is represented by the greyscale shading in Figure 3.7, with black indicating a 500 star excess per square degree. The overall pattern of excess is similar to the significance map in the righthand panel of Figure 3.5, with perhaps the southern regions showing a stronger signal in the density map than in the significance map. This could be understood in terms of the relative significance of the feature decreasing towards the Galactic plane due to the increase in background Milky Way stars, while the number density of stars in the feature in fact remains constant.

In order to make a rough estimation of the sky coverage of the VSS, an ellipse has been overplotted on Figure 3.7. The chosen shape is somewhat arbitrary, with the positioning and size selected so as to include the regions in which the excess
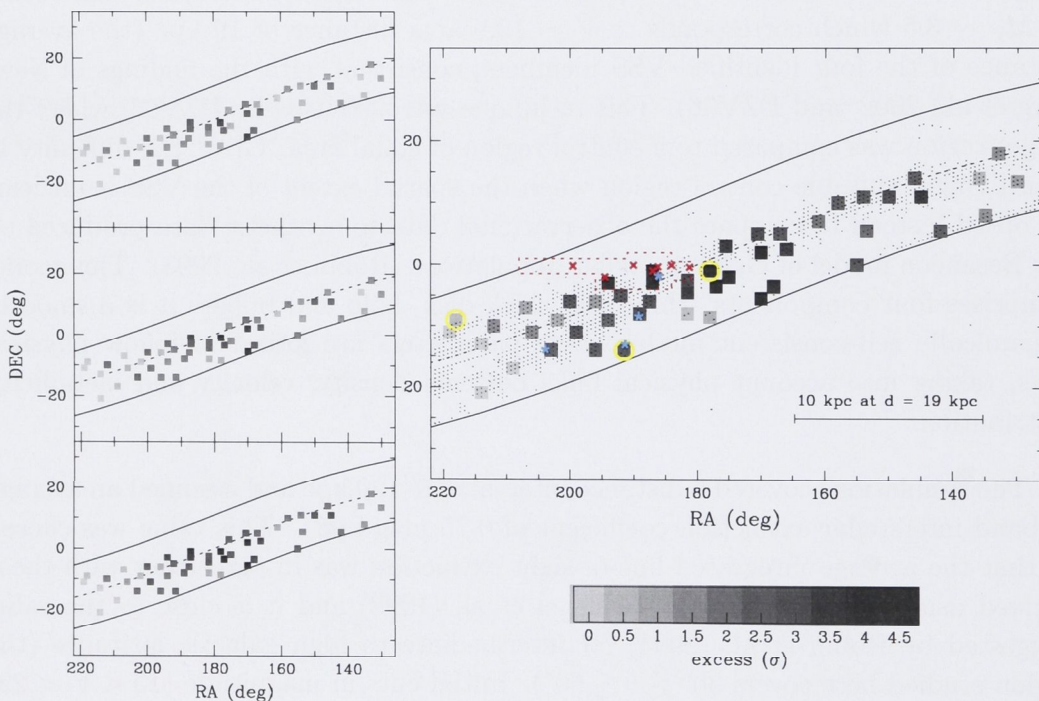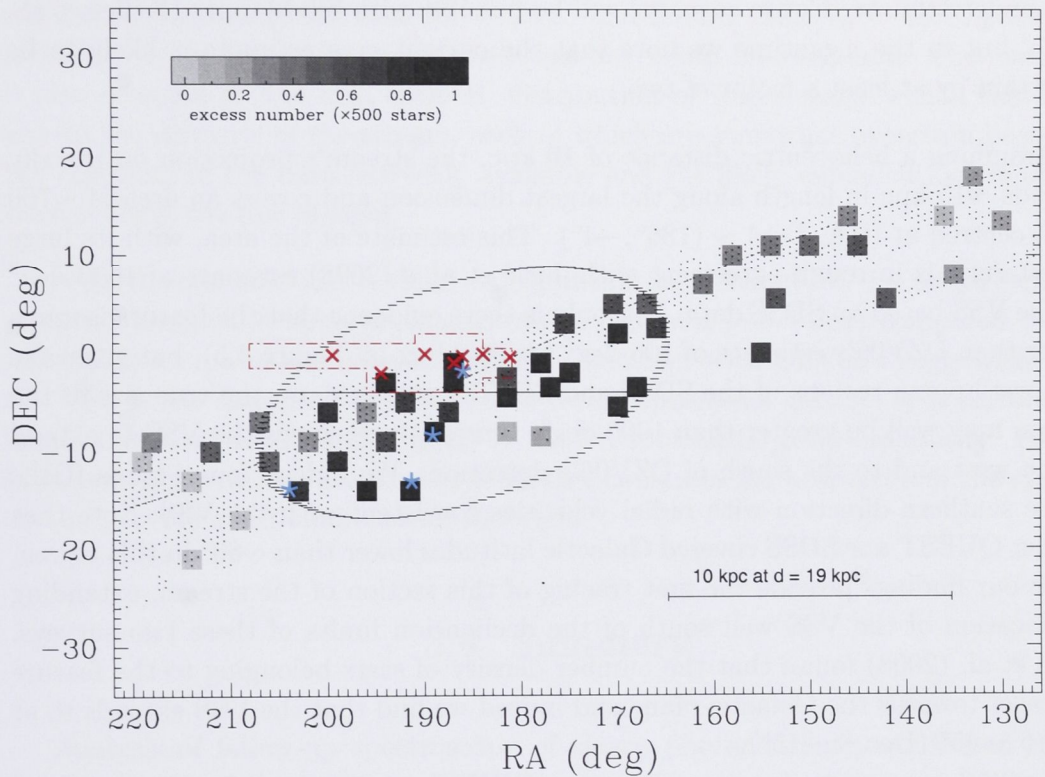
Figure 3.7: The spatial distribution of regions in which data was compared to the Galactic stellar distribution model. The number of excess data stars over synthetic stars per deg^2 is represented by the colouring of the region according to the scale shown, with darker shades indicating a larger excess. The range of magnitudes included in the excess calculation was $16.25 < V_0 < 19.75$. Also shown are the four stars from our sample with V_{GSR} consistent with the VSS *(cyan asterisks)* and those found by DZV06 *(red crosses)*. The ellipse outlines the estimated area of the VSS based on the current analysis. As in Figure 3.1, the red dashed box is DZV06's identification of the VSS region. The dashed line represents the ecliptic and the small dots show the centres of the fields surveyed. The approximate southern limit of the SDSS coverage in this region is shown by the solid line at Dec = $-4°$.

appears visually to be significant. The ellipse encompasses areas not sampled by the SEKBO survey on the basis that the VSS could plausibly extend to those areas given the distribution of high excess regions in the sampled areas and assuming a certain degree of uniformity. This assumption could lead to an overestimate in the area, but conversely, the VSS may well extend beyond the survey region (particularly to the south where no data has been gathered by previous surveys) leading to an area underestimate. Entire coverage will be possible with SkyMapper (Keller et al., 2007), but in the meantime we note that the current area estimate is likely to be uncertain by at least a factor of two.

Assuming a heliocentric distance of 19 kpc, the stream's projection on the sky extends $\sim$15 kpc in length along the largest dimension and covers an area of $\sim$760 deg^2, centred at (RA, Dec) $\sim$ (186°, −4°). This estimate of the area, with its large uncertainty, is in rough agreement with Jurić et al.'s (2008) estimate of 1000 deg^2 for the VSS based on SDSS data. Not only is there evidence that the feature is much larger than DZV06's estimate of 106 deg^2 (dashed box on Figure 3.5), but given the non-overlapping regions of the SDSS and SEKBO survey data, the true size of the stream may well be greater than 1000 deg^2. Our analysis shows the VSS to extend to the west and to the south of DZV06's detection. We indeed found three RRLs in the southern direction with radial velocities consistent with the VSS. Note that neither QUEST nor SDSS covered Galactic latitudes lower than $\sim$60° in this region, hence our findings provide the first tracing of this section of the stream, extending the location of the VSS well south of the declination limits of these two surveys. Jurić et al. (2008) found that the number density of stars belonging to the feature increases towards the Galactic plane and indeed we find that the VSS extends to at least $b \sim 45°$ (Dec $\sim -15°$).

Having estimated the area of the VSS, it is now possible to calculate an estimate of the absolute magnitude, M_V, of the stream. The fluxes for the excess stars in each magnitude bin ($16.25 < V_0 < 19.75$) were averaged over all the regions contained within the ellipse, summed over the magnitude bins and finally, multiplied by the area of the ellipse. Assuming a distance of 19 kpc and an area of 760 deg^2 and using V band values of $M_\odot = 4.83$ and $L_\odot = 4.64 \times 10^{25}$ W (Binney & Merrifield, 1998), we calculate $M_V = -11.9$ mag. This value is considerably brighter than $M_R = -8.0$ mag estimated by Jurić et al. (2008). We note, however, that their value assumed a distance of 10 kpc, an area of 1000 deg^2 and magnitude limits of $18 < R < 21.5$. Using values as close to these as possible given the constraints of our data, our estimate becomes $M_V = -10.1$ mag.

A final point to note is that Jurić et al. (2008) find the VSS to span $\sim$10 kpc along the line-of-sight, at distances closer than where it was detected by the SEKBO survey, and that their survey data did not go beyond a scale height of 20 kpc. It thus seems a likely scenario that the VSS spans many kpc along the line-of-sight

(indeed DZV06 found possible members at distances ranging between 16 and 24 kpc and new results of Vivas et al., 2008, find possible members as close as 12 kpc) but is more diffuse at distances $\lesssim 15$ kpc, with the highest concentration at $d \sim 19$ kpc. Considering that Jurić et al. (2008) do not include the portion at $d \sim 19$ kpc in their M_R calculation, it is not surprising that their value should be considerably fainter than ours. It is also important to note that all our values are lower limits only, since stars brighter than $V_0 = 16.25$ and fainter than $V_0 = 19.75$ were not included. In addition, incompleteness was not taken into account. The estimate is also sensitive to the area covered, distribution of VSS density within that area and to the distance of the stream, each of which are somewhat uncertain based on the sampling of the data currently available and the likely extended nature of the stream along the line-of-sight.

Nevertheless, the VSS is clearly a significant local structure. Its origin remains unclear, though the large abundance range observed (~ 0.4 dex) compared to the internal precision of the measurements is consistent with DZV06's suggestion that the VSS is the disrupted remnants of a dwarf Spheroidal galaxy. It is certainly a large, diffuse structure and is likely to have a substantial total luminosity. Future kinematic observations are needed to further constrain the properties of the system and to provide additional clues to its origin.

3.4 Summary

Analysis of follow-up spectroscopy of eleven photometrically confirmed RRLs from a candidate list based on SEKBO survey data reveals three new RRLs with velocities consistent with membership in the Virgo Stellar Stream, in addition to one previously identified member ($\langle V_{\mathrm{GSR}} \rangle = 127 \pm 10$ km s^{-1}, $\sigma = 27$ km s^{-1}). The two type ab members have $\langle [\mathrm{Fe/H}] \rangle = -1.95 \pm 0.1$ and an abundance range of ~ 0.4 dex, consistent with values found by DZV06 for the VSS. The newly discovered VSS members occupy a region of space covered by neither QUEST nor SDSS data, to the south-east of the apparent centre of the stream at (RA, Dec) $\sim (186°, -4°)$. Comparison of luminosity functions for observed data compared to data synthesised with the Besançon Galactic model (Robin et al., 2003) reveals the VSS to be a large, diffuse feature, covering at least 760 deg^2 of sky. The core of the VSS appears to have an angular size of $\sim 45°$ along the longest dimension, corresponding to a spatial scale of ~ 15 kpc in projection, assuming a heliocentric distance of ~ 19 kpc. We have traced the stream as far south as Dec $\sim -14°$ and to Galactic latitudes as low as $b \sim 45°$.

Sounds of laughter, shades of earth
Are ringing through my opened ears
Inciting and inviting me

Lennon & McCartney

4

The Sagittarius Stream

As discussed in Chapter 1, debris from the interaction between the Sgr dwarf galaxy and the Milky Way is the most significant substructure yet uncovered in the outer halo. In Chapter 2, the selection of targets in a region of the SEKBO survey which overlaps the expected position of a portion of the Sgr debris stream was detailed. Subsequently, the procedures used to reduce the photometric and spectroscopic data were described. While the previous chapter focused on the Virgo Stellar Stream region, we now turn our attention to results and analysis for the Sagittarius Stream region RRLs. Specifically, §4.1 presents the radial velocities and, taking into account positional information, compares them to models of the disruption of Sgr assuming different shapes for the dark halo potential. The possible association of VSS region RRLs with Sgr debris is also explored. §4.2 then examines the metal abundances of the Sgr region RRLs and §4.3 investigates the potential use of luminosity functions to elucidate the spatial nature of the Sgr Stream. Finally, the results are summarised in §4.4.

4.1 Radial velocities

Table 4.1 summarises results from the spectroscopic data for the 26 RRLs in the Sgr region, including the systemic $V_{\rm GSR}$ values calculated as described in §2.2. Results for the VSS region stars are also included for ease of reference; see following discussion. The distributions of $V_{\rm GSR}$ values in the 20 h (5 stars) and in the 21.5 h (21 stars) Sgr regions are presented as generalised histograms in Figure 4.1 (note that

results from the two regions are not combined since the pattern of radial velocities of Sgr Stream stars varies with position, as discussed further below). Deviations of the distributions from the expected normal distribution of general halo RRLs (with $\langle V_{\rm GSR} \rangle = 0$ km s^{-1} and $\sigma = 100$ km s^{-1}; e.g. Sirko et al., 2004; Brown et al., 2005) are evident. In the 20 h region, there is an apparent excess of stars having highly positive radial velocities ($V_{\rm GSR} \sim 200$ km s^{-1}), while in the 21.5 h region a striking excess (five stars) is evident at highly negative velocities ($V_{\rm GSR} \sim -175$ km s^{-1}). If this were a sample containing purely halo field stars (distributed $N{\sim}(0,100^2)$), only one RRL would be expected to have its $V_{\rm GSR}$ as extreme as the group observed. There is also an apparent lack of stars with $-25 < V_{\rm GSR} < -100$ km s^{-1}. This lack of fit to a normal distribution (again, not reaching statistical significance due to the small sample size) supports our hypothesis that these Sgr region RRLs are not simply a random selection from a smooth halo.
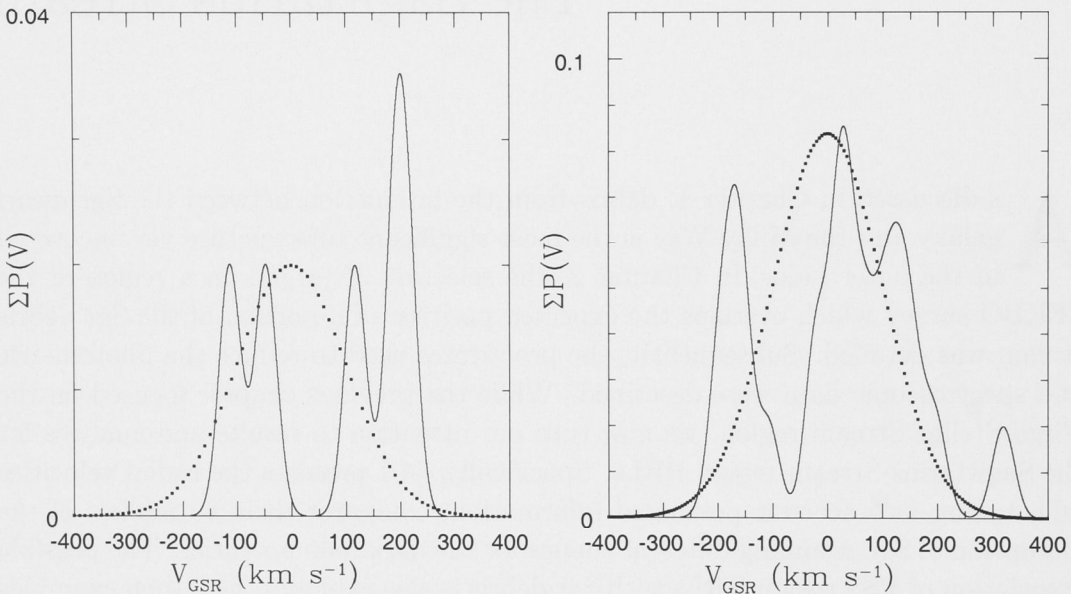
Figure 4.1: Generalised histograms of $V_{\rm GSR}$ (with kernel of 20 km s^{-1}) for observed RRLs in the Sgr regions. *Left:* the 5 RRLs in the 20 h region; *Right:* the 21 RRLs in the 21.5 h region. Overplotted in each panel *(dotted line)* is the expected distribution of $V_{\rm GSR}$ given a halo population in which velocities are normally distributed with $\langle V_{\rm GSR} \rangle = 0$ km s^{-1} and $\sigma = 100$ km s^{-1}. In the 20 h region, there is an excess of stars with highly positive velocities ($V_{\rm GSR} \sim 200$ km s^{-1}) while in the 21.5 h region, there is a marked excess of stars with highly negative velocities ($V_{\rm GSR} \sim -175$ km s^{-1}) compared to the expected halo population distribution.

Table 4.1: Spectroscopic data summary for Sgr region

ID	$\Lambda_\odot$ (deg)	$B_\odot$ (deg)	RRL type	systemic vel. calculation	n_{vel}	V_{helio} (km s^{-1})	V_{GSR} (km s^{-1})	$n_{Fe/H}$	[Fe/H]
20 h clump									
109463-3964	11.5	−10.8	*ab*	fit	2	−197	−113	3	−1.58
109464-5627	10.9	−10.2	*ab*	average	4	36	117	-	-
109489-2379	11.1	−10.2	*ab*	fit	3	108	191	3	−2.17
109489-3076	10.9	−10.4	*ab*	fit	3	−129	−47	3	−1.85
109582-3724	10.6	−10.5	*ab*	fit	3	129	211	4	−1.93
21.5 h clump									
99747-73	31.6	−11.9	*ab*	fit	1	−77	20	3	−2.55
99752-96	36.5	−12.7	*c*	average	3	−74	26	-	-
102292-1096	33.4	−14.4	*ab*	fit	2	92	198	2	−1.61
102297-1488	32.3	−13.6	*ab*	fit	3	−290	−187	4	−1.53
102601-400	35.3	−12.8	*ab*	fit	2	−301	−201	3	−1.98
102601-1489	35.1	−13.0	*ab*	fit	2	−123	−22	3	−2.26
110735-595	32.5	−15.2	*ab*	average	4	−277	−169	4	−1.62
110738-411	37.2	−12.0	*ab*	fit	4	−206	−107	4	−2.10
110753-346	35.7	−12.3	*ab*	fit	2	221	319	3	−2.00
110823-641	29.7	−10.9	*c*	average	3	−112	−20	-	-
110827-579	36.5	−11.5	*ab*	fit	3	−252	−157	2	−1.51
110828-1100	29.3	−10.7	*ab*	fit	3	−250	−159	3	−1.76
113345-1032	37.6	−11.5	*c*	average	3	7	103	-	-
114793-1530	30.2	−16.1	*c*	average	3	51	162	-	-
115381-349	39.4	−12.6	*ab*	fit	1	−38	63	2	−1.87

Table 4.1 (cont'd)

ID	$\Lambda_\odot$ (deg)	$B_\odot$ (deg)	RRL type	systemic vel. calculation	n_{vel}	V_{helio} (km s^{-1})	V_{GSR} (km s^{-1})	$n_{Fe/H}$	[Fe/H]
115381-767	38.8	−12.5	*ab*	fit	2	−74	26	3	−2.01
125857-20	27.1	−16.2	*ab*	fit	1	−1	109	1	−2.00
126040-78	29.5	−8.9	*ab*	fit	2	−50	34	2	−1.45
126093-1135	30.3	−8.0	*ab*	fit	3	56	137	3	−1.53
126245-763	33.7	−8.7	*ab*	fit	1	−13	72	1	−1.56
126536-714	31.0	−7.2	*ab*	fit	1	55	134	3	−0.73
VSS region									
96102-170	263.7	15.2	*ab*	fit	2	230	128	3	−2.15
105648-222	287.0	11.2	*ab*	fit	1	−91	−162	1	−1.45
107552-323	268.2	18.0	*ab*	fit	3	302	193	3	−1.34
108227-529	262.5	17.8	*c*	average	1	−8	−119	-	-
109247-528	286.4	14.7	*c*	average	2	113	28	-	-
119827-670	269.0	17.7	*ab*	fit	2	−84	−192	2	−1.68
120185-77	264.7	13.0	*ab*	fit	2	94	1	2	−2.38
120679-336	269.8	19.5	*ab*	fit	3	204	91	2	−1.74
120698-392	285.9	16.8	*c*	average	1	227	134	-	-
121242-188	274.3	22.4	*c*	average	3	276	155	-	-
121194-205	273.4	20.0	*c*	average	1	−39	−152	-	-

In order to further investigate the pattern of radial velocities and to explore how well they agree with expectations for Sgr Stream stars, we have compared the velocities to those predicted by the recent models of Law et al. (2005)[1] (hereafter LJM05). While a number of other models for the disruption from the Sgr-Milky Way interaction exist (see §1.3.1 for a brief review), LJM05's were chosen for the comparison as they are (at the time of writing) the only models based on a complete all-sky view of the tidal streams of Sgr (namely, the 2MASS M giant sample). They use N-body simulations to predict the heliocentric distances and radial velocities of 10^5 particles stripped from the Sgr dwarf up to four orbits ago (i.e. up to approximately 3 Gyr ago). Three models of the flattening, q, of the Galactic dark halo potential are considered: prolate ($q = 1.25$), spherical ($q = 1.0$) and oblate ($q = 0.90$). Their simulations adopt a spherical, Sun-centred, Sgr coordinate system[2], with the longitudinal coordinate, $\Lambda_\odot$, being zero in the direction of the Sgr core and increasing along the Sgr trailing debris stream. The zero plane of the latitude coordinate, $B_\odot$, is defined by the best fit great circle of the Sgr debris. For the purpose of clarifying the discussion which follows, Figure 4.2 shows $V_{\rm GSR}$ plotted against $\Lambda_\odot$ for the case of the prolate potential (selected due to its more easily identifiable streams compared to oblate and spherical potentials). The Sgr core is, by definition, located at $\Lambda_\odot = 0°$, the leading stream is highlighted in magenta and the trailing stream in cyan. In addition, certain parts of the streams have been labelled (a–d) for future reference. In the text which follows, they are referred to as, for example, *"debris-c"*, where the $\Lambda_\odot$ range should also be taken into account in order to focus on the relevant stream section.
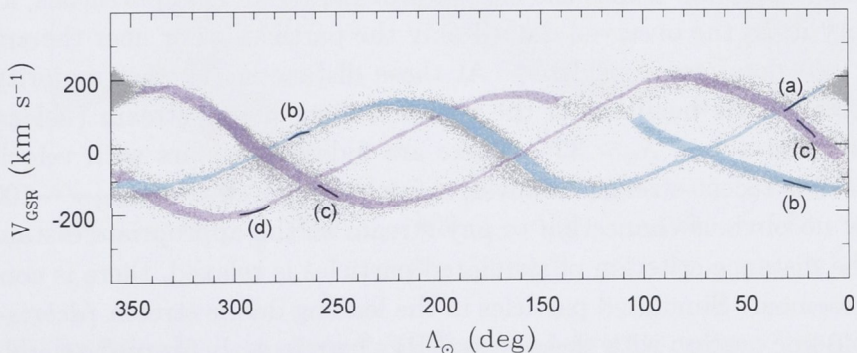
Figure 4.2: Radial velocities against $\Lambda_\odot$ from Law et al.'s (2005) model with a prolate Galactic halo potential. By definition, the Sgr dwarf is located at $\Lambda_\odot = 0°$. The leading and trailing arms are highlighted in magenta and cyan, respectively. For ease of reference, certain parts of the stream have been identified: (a) new trailing debris (current perigalactic passage); (b) very old trailing debris (4 orbits ago); (c) old leading debris (3–4 orbits ago); and (d) very old leading debris (4 orbits ago).

---

[1]Law et al. (2005) provide their data at `http://www.astro.virginia.edu/~srm4n/Sgr`.

[2]We converted from the standard Galactic coordinate system to the Sgr longitudinal coordinate system using David R. Law's C++ code, provided at the website above.

Figure 4.3 shows the distribution of V_{GSR} as a function of $\Lambda_\odot$ for LJM05's simulated particles assuming prolate, spherical and oblate halo potentials. Our observed RRLs are at heliocentric distances 16–21 kpc. Distances are based on the assumption of $M_V = 0.56$ and have an uncertainty of $\sim$7%, as described in KMP08. This corresponds to an uncertainty of approximately $\pm$1 kpc at a distance of 20 kpc. In order to isolate simulated stars at similar distances to the observed stars, the plot is colour-coded, with red representing particles at 6–31 kpc (i.e. 10 kpc closer/farther than our observed range). All other distances are colour-coded grey. The choice to consider a wider distance range for the simulated particles than for our observational data was motivated by the significant uncertainties involved in the modelled distances. The major factor contributing to this is the 17% distance uncertainty for 2MASS M giant stars, stemming from the uncertainty in the values of the solar distance from the Galactic centre and from Sgr. LJM05 note that the estimated size of Sgr's orbit scales according to the M giant distance scale, and distances to simulated debris particles similarly. (However, for comparison, equivalent plots highlighting simulated particles at the observed distances of 16–21 kpc are shown in Figure 4.4). Overplotted on Figure 4.3 as filled circles are our observational data in the Sgr region, with the 20 h clump corresponding to $\Lambda_\odot = 10°$ and the 21.5 h clump corresponding to $\Lambda_\odot = 25$–40°. In order to explore their possible association with the Sgr Stream (as discussed in §1.3.2), our observed RRLs in the VSS region are also plotted (triangles at $\Lambda_\odot = 260$–290°).

A comparison between the observed and simulated data in the 20 h and 21.5 h regions ($\Lambda_\odot \sim 10°$ and $\Lambda_\odot \sim 25$–40°, respectively) reveals several points of interest. The overall impression is that the models provide, for all halo potentials, a less than satisfactory fit to the observed data if only the particles at or near the appropriate distance (red dots) are considered. At these distances, the vast majority of stars are predicted to be members of the recent trailing debris stream *(debris-a)*, with $V_{GSR} \sim 100$ km s^{-1} at $\Lambda_\odot \sim 35°$. There are indeed ten stars with velocities close to that of this recent stream, however, a further eight stars ($V_{GSR} \sim -100$–+50km s^{-1}) show no obvious connection to any stream at the appropriate distance. However, if the distance criterion of simulated particles is relaxed, there is considerably better agreement. Simulated particles in the leading debris stream *(debris-c)* at distances $\sim$40 kpc overlap with these eight RRLs, particularly for prolate and spherical potentials. Interestingly, Majewski et al. (1999) found a similar result, with their red clump stars at $\Lambda_\odot = 27°$ showing a wide range in radial velocity which was well matched by the simulated particles. As with our data, however, the distances of their stars were measured to be $\sim$20 kpc rather than the 40 kpc predicted by the models. There is thus evidence that the distances in the models may be inaccurate, if the observed RRLs are indeed Sgr Stream members.

Another possible way of accounting for the "stray" RRLs (notably, the six RRLs between ~ -25 and 50 km s^{-1} at $\Lambda_\odot \sim 35°$) is by considering that a certain number
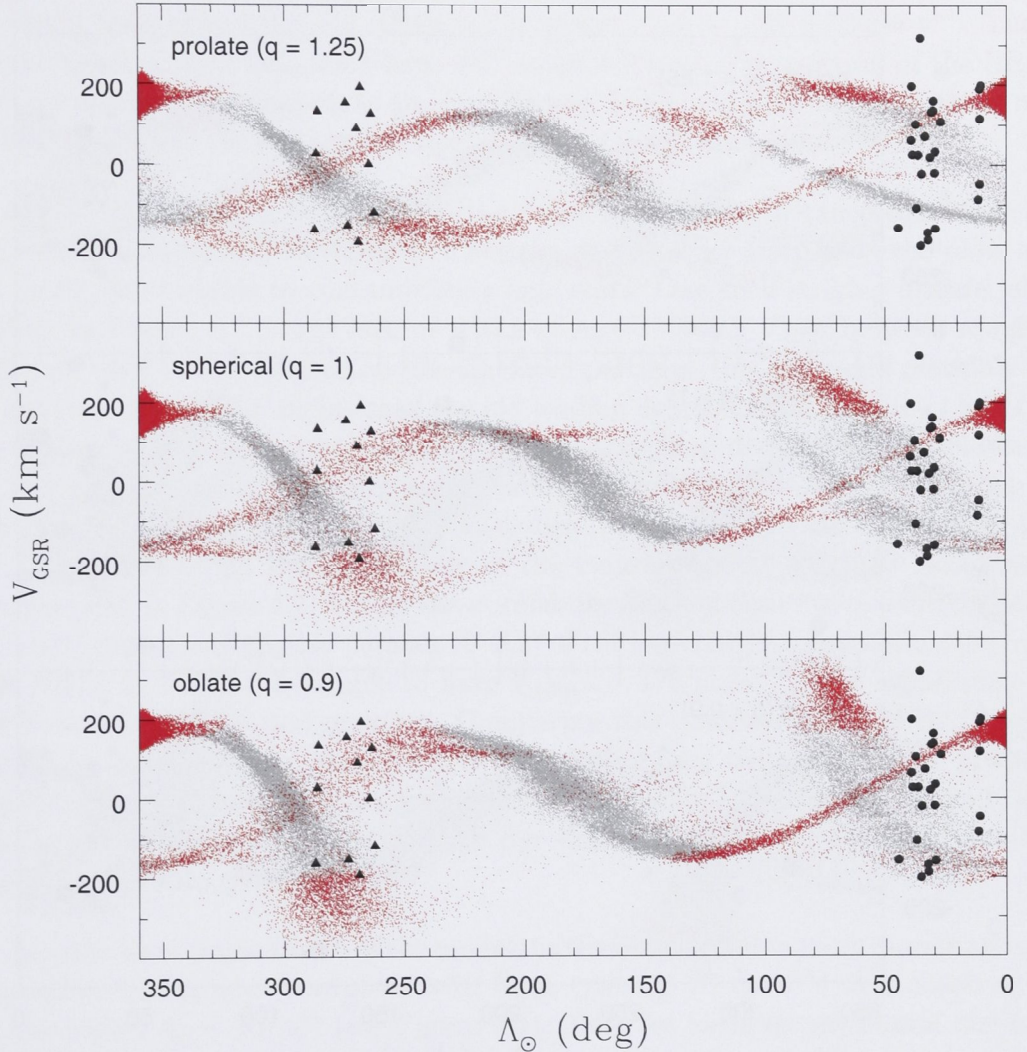
Figure 4.3: Radial velocities against $\Lambda_\odot$ from models with prolate *(top)*, spherical *(middle)* and oblate *(bottom)* Galactic halo potentials (Law et al., 2005). Red denotes simulated stars with heliocentric distances $d = 6$–31 kpc while grey denotes stars at all other distances. Overplotted are values for the 26 observed RRLs in the 20 h and 21.5 h Sgr regions *(circles)* and the 11 RRLs in the VSS region *(triangles)*. Note that, at the relevant distance, only the oblate model is able to predict the group of stars at $\Lambda_\odot \sim 35°$ which are observed to have highly negative V_{GSR}.
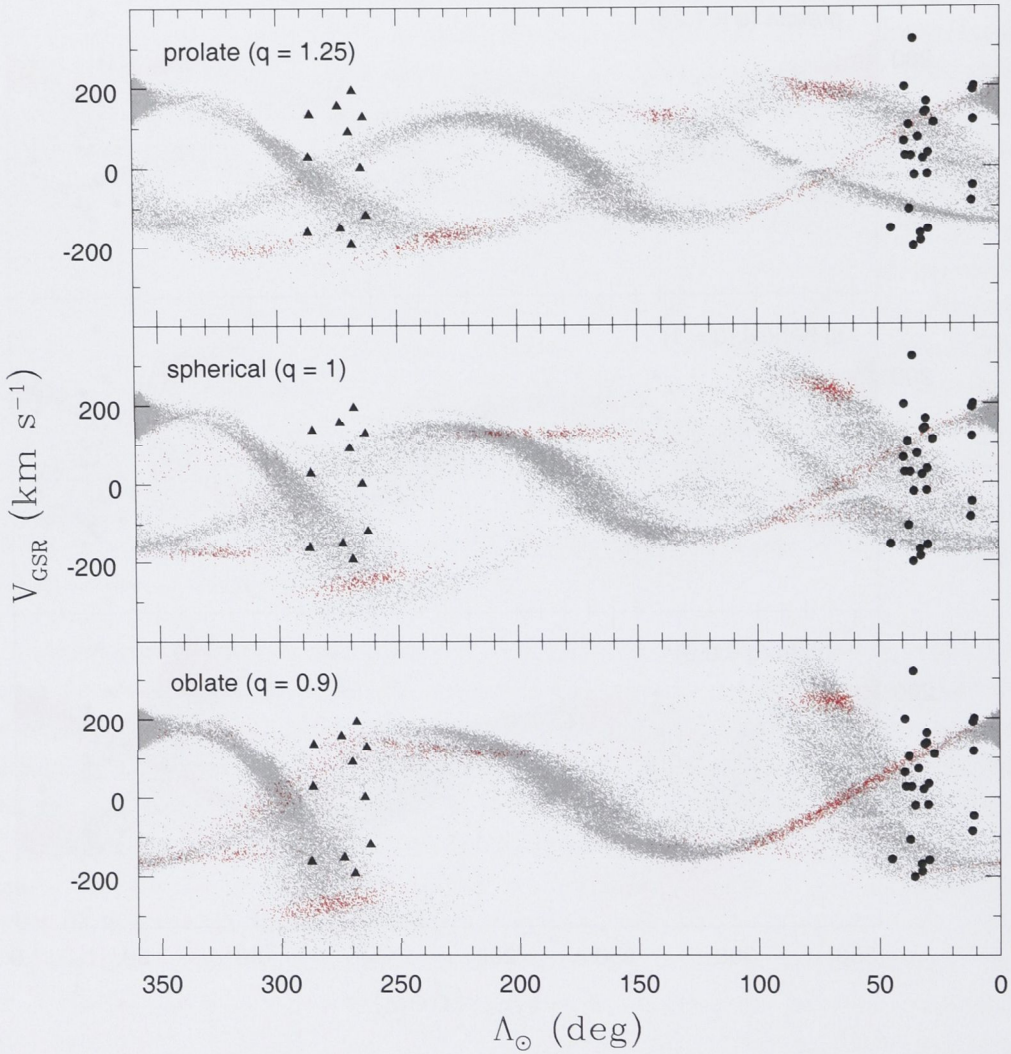
Figure 4.4: Radial velocities against $\Lambda_\odot$ from models with prolate *(top)*, spherical *(middle)* and oblate *(bottom)* Galactic halo potentials (Law et al., 2005). Red denotes simulated stars with heliocentric distances $d = 16$–21 kpc while grey denotes stars at all other distances. Overplotted are values for the 26 observed RRLs in the 20 h and 21.5 h Sgr regions *(circles)* and the 11 RRLs in the VSS region *(triangles)*.

of stars in our sample may be field halo RRLs rather than members of the Sgr Stream. Based on the smooth halo distribution of RRLs produced by KMP08, we estimate a 10–15% contamination of our 21.5 h sample by field RRLs. This corresponds to approximately 3±2 RRLs. Assuming these halo field stars have a normal distribution of radial velocities with $\langle V_{GSR} \rangle = 0$ km s^{-1} and $\sigma = 100$ km s^{-1}, we would then expect 0.3–1.5 RRLs in the range $V_{GSR} \sim -25$–$+50$ km s^{-1}. Thus, the inclusion of field halo stars may well account for some proportion of the RRLs with no apparent association to the Sgr Stream, but a certain number of those not fitting the models (at the appropriate distance) remain unaccounted for.

While the exclusion of certain RRLs helps to alleviate distance discrepancies between the model and our data to a certain extent, other features of the plots are not easily attributable to contaminating halo stars. One such striking feature, also evident in Figure 4.1, is the lack of RRLs at $\Lambda_\odot \sim 35°$ with V_{GSR} between roughly -25 and -100 km s^{-1}. Based on the simulated particles, this gap could plausibly be interpreted as dividing members of the old leading debris stream *(debris-c)* and the old trailing stream *(debris-b)*, though again, the simulated distances are problematic for this interpretation. The even more remarkable feature, however, is the group of five stars with highly negative radial velocities ($\langle V_{GSR} \rangle = -175$ km s^{-1}, $\sigma = 19$ km s^{-1}, slightly less than the uncertainty in the measurements) which we noted as a distinct peak in Figure 4.1. Under the normal distribution assumption stated above, we would expect a negligible number (0–0.2) of the expected 1–5 contaminating halo field RRLs in the 21.5 h sample to have $V_{GSR} < -175$ km s^{-1}. The significance of the feature is thus beyond question. Comparing this observed group of RRLs with the simulated particles in Figure 4.3, it is clear that only the oblate model predicts any significant number of stars with such velocities at this distance. In fact, the association of this group of stars with Sgr debris arguably rules out the prolate model for the halo potential.

In order to examine the fit of the models to the observed data more quantitatively, generalised histograms (convolved with V_{GSR} errors of 20 km s^{-1}) were constructed for the region $\Lambda_\odot = 25$–$40°$ (see Figure 4.5). Here we focus on the actual distance range of the observed data, 16–21 kpc (cyan lines), as shown in Figure 4.4, as well as the same augmented range used in Figure 4.3, 6-31 kpc (green lines). The most obvious feature of the plots is the lack of the narrow peak in the observed data at $V_{GSR} \sim 100$ km s^{-1} which is seen in the simulated data (corresponding to *debris-a*). Rather, a more diffuse spread of velocities is observed, partly overlapping with the large simulated peak, but extending to $V_{GSR} \sim -50$ km s^{-1}. As mentioned above, one could attempt to explain the discrepancy by attributing the bump in the observed data at ~ 25 km s^{-1} to contaminating halo field stars. But what of the observed peak at ~ -175 km s^{-1}? A clustering of halo field stars at such a negative radial velocity would be statisically highly improbable given the assumption that they are distributed normally with $\langle V_{GSR} \rangle = 0$ km s^{-1} and $\sigma = 100$ km s^{-1}.

Accepting that they are members of the Sgr Stream then indicates that the oblate model provides the best fit to the observed data. As we noted in Figure 4.3, the prolate model entirely fails to predict stars with these negative radial velocities. In the case of the spherical model, it predicts some of these stars but only in the case where we consider an augmented distance range, going 10 kpc beyond our observed distances. The oblate model, on the other hand, predicts stars at these velocities and at the correct distances, though the number of predicted stars increases when larger distances are considered. The velocity of the peak is also shifted to more accurately coincide with the observed data when distances up to 31 kpc are considered.

At this point it is useful to briefly consider the distance distribution of simulated particles under the different models. The inset distance histogram in Figure 4.5 for the oblate model over the relevant $\Lambda_\odot$ range indicates that the overdensity of Sgr Stream stars is expected to peak around 20 kpc and fall off as the distance approaches 30 kpc, with a second peak at distances $\sim$40 kpc. Prolate and spherical models show much less marked peaks at 20 kpc. This again supports the oblate model if we consider the significance map of overdensities revealed in the SEKBO survey data (see the RRL radial distribution in Figure 2.1). This map shows a notable density enhancement at distances $\sim$20 kpc and a density dropoff with distance which is not attributable to incompleteness effects (see KMP08 for comparison with a smooth simulated halo).

Thus far we have only discussed RRLs in the 20 and 21.5 h Sgr regions. We now turn our attention to the RRLs in the VSS region and explore their potential association with the Sgr debris streams. Figure 4.6 illustrates (using the oblate model case) that the stars considered indeed have appropriate values of $B_\odot$ to be Sgr debris, as the simulated streams are populated at $B_\odot > 5°$ at $\Lambda_\odot$ corresponding to the VSS (i.e. 12.4 and 14 h) region, while at $\Lambda_\odot$ corresponding to the Sgr (i.e. 20 and 21.5 h) regions they are populated at $B_\odot < -5°$. Note that, as with Figures 4.3 and 4.4, we highlight in red distances corresponding to the observed range of 16–21 kpc (left panel) and an augmented distance range of 6–31 kpc (right panel).

Having confidence that our VSS region RRLs have spatial locations consistent with Sgr debris, we now consider how their velocities fit with LJM05's models (see triangles at $\Lambda_\odot$= 260–290° on Figure 4.3). The trends in radial velocity with $\Lambda_\odot$ are immediately striking. Neglecting for a moment the star with $V_{GSR}\sim 0$ km s^{-1} (a likely candidate for a contaminating halo field star), the remaining RRLs appear to be divisible into two groups: six with positive velocities and four with negative. In both groups the apparent trend is for V_{GSR} to increase with decreasing $\Lambda_\odot$. Let us consider first the group with positive V_{GSR}. Four of these RRLs were identified in §3.1 as VSS members on the basis that their radial velocities were between 40 and 160 km s^{-1}. There is a clear suggestion from Figure 4.3, however, that these four stars are in fact part of a structure which varies considerably in radial velocity
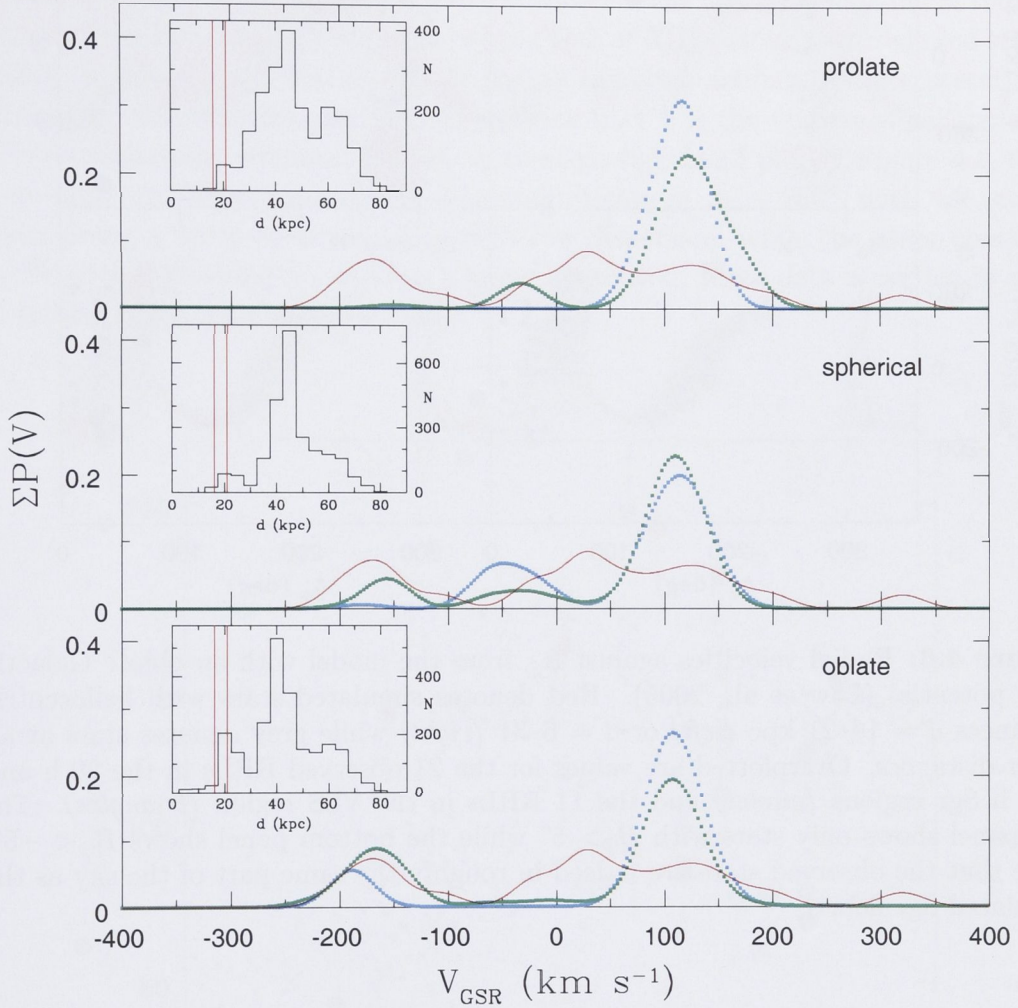
Figure 4.5: Generalised histogram of V_{GSR} (with kernel of 20 km s^{-1}) for the 21 observed RRLs in the 21.5 h Sgr region *(red solid lines)* and for simulated stars between $\Lambda_\odot = 25°$ and $\Lambda_\odot = 40°$ at heliocentric distances $d = 16$–21 kpc *(cyan dotted lines)* and $d = 6$–31 kpc *(green dotted lines)*. The model halo potential is prolate *(top)*, spherical *(middle)* or oblate *(bottom)*. The total number of model stars in the selected $\Lambda_\odot$ and d ranges has been normalised to the number of observed stars. The inset histograms show the distance distribution of simulated stars for each halo potential in the selected $\Lambda_\odot$ range. Note that Law et al. (2005) added a 17% artificial random distance scatter to the simulated particles to mimic the photometric distance error in the 2MASS sample. The red lines indicate the distance range of the observed data.

Figure 4.6: Radial velocities against $\Lambda_\odot$ from the model with an oblate Galactic halo potential (Law et al., 2005). Red denotes simulated stars with heliocentric distances $d = 16\text{--}21$ kpc *(left)* or $d = 6\text{--}31$ *(right)* while grey denotes stars at all other distances. Overplotted are values for the 21 observed RRLs in the 20 h and 21.5 h Sgr regions *(circles)* and the 11 RRLs in the VSS region *(triangles)*. The top panel shows only stars with $B_\odot > 5°$ while the bottom panel shows $B_\odot < -5°$. Note that the observed stars are indeed in roughly the same part of the sky as the simulated Sgr debris.

along its extent, with observed members having V_{GSR} as low as 28 km s^{-1} and as high as 193 km s^{-1}.

It is interesting to note that Duffau et al. (2006) also saw evidence of a possible radial velocity gradient in their VSS sample, when comparing their 'inner' and 'outer' samples. It seems highly unlikely, however, that this gradient should happen to so neatly coincide with LJM05's oblate model prediction for the Sgr trailing stream *(debris-d)*, considering the spatial coincidence of the stars with the stream. A portion of the oblate panel of Figure 4.3, focusing solely on V_{GSR} values near this trailing stream, is redisplayed in Figure 4.7. We have now also included the data of DZV06 which falls within the selected V_{GSR} range. There is reasonable agreement between the two data sets, though DZV06's covers a smaller range in $\Lambda_\odot$ and is therefore less well suited to examining velocity gradients along the stream. Indeed, according to the model, the stream's radial velocity starts to flatten at $\Lambda_\odot$ less than

270°. Nevertheless, their data does still show signs of following the general trend of the predicted trailing stream. Note that the reported velocities of the one common star in the two data sets within this V_{GSR} range (at $\Lambda_\odot \sim 264°$) agree within the combined errors. A curious pattern in Figure 4.7 is the apparent flanking of the simulated stream by the observed data, with a lack of RRLs along the predicted stream centre. If this is a real feature rather than a sampling artifact, its interpretation is intriguing. For example, one might speculate that it is the observational signature of two overlapping streams. Indeed, in the top, righthand plot of Figure 4.6, there is an apparent bifurcation of the simulated stream at $\Lambda_\odot \sim 250°$, with one stream maintaining a fairly constant V_{GSR} with low dispersion, while the other continues to rise with decreasing $\Lambda_\odot$ and has a larger dispersion. More data is needed in order to further investigate this possibility.
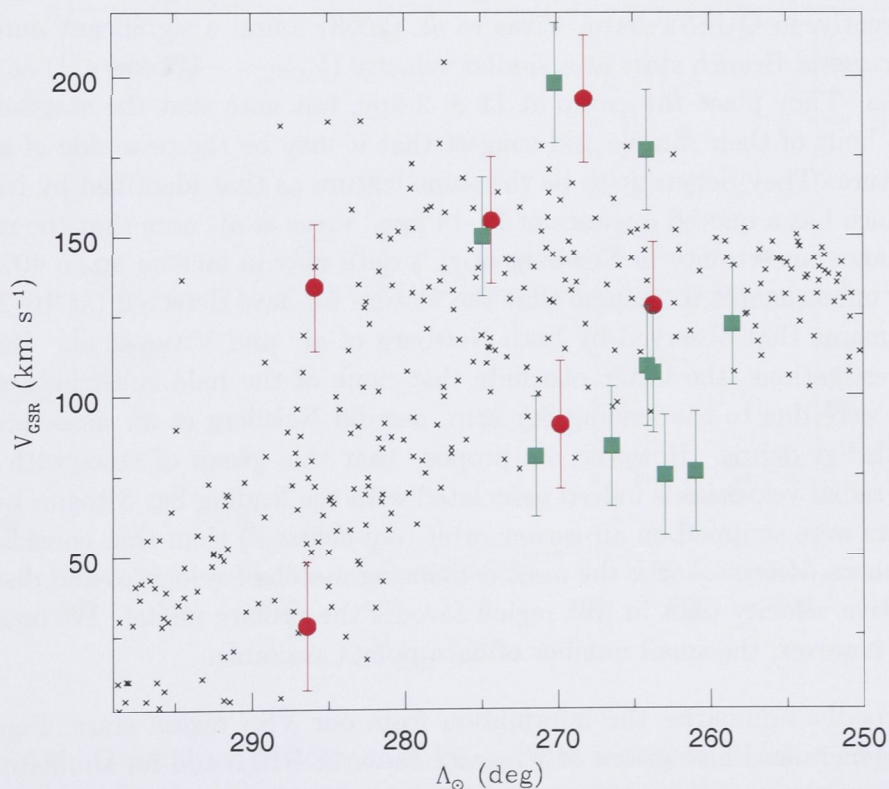
Figure 4.7: Radial velocities against $\Lambda_\odot$ from Law et al.'s (2005) model with an oblate Galactic halo potential *(small crosses)*, where only particles at heliocentric distances $d = 16$–21 kpc are plotted. Overplotted are values for RRLs in the VSS region from our data set *(red circles)* and from Duffau et al.'s (2006) data set *(green squares)*. While both sets include RRLs outside the plotted V_{GSR} range, these limits (which encompass all the "VSS members") have been selected to focus on the possible association of these VSS region RRLs with this trailing arm section of the Sgr Stream.

While the data for the positive V_{GSR} RRLs clearly favours the oblate model over the prolate and spherical models, the negative V_{GSR} RRLs in the VSS region are less decisive. While not wildly inconsistent with any of the models, the data seems to best fit the very old leading debris *(debris-d)* in the prolate model (see the top panel of Figure 4.3), though admittedly this conclusion is based on only a small number of data points. It is interesting to note that Kundu et al. (2002) similarly attributed to an old wrap of the Sgr leading tidal arm a group of K giants near this $\Lambda_\odot$ with a similar pattern of velocities, though at closer distances (2–10 kpc) than our sample. This raises the question of whether the groups are indeed related, and if so, what is the nature of the feature's distribution over distance?

Before returning to this point, it is salient to remark on the evidence that these four stars ($\langle V_{GSR} \rangle = -156$ km s^{-1}) are indeed part of some real substructure rather than being due to chance sampling. In this region, Newberg et al. (2007) detected a group of F stars in SDSS data having a similar velocity ($V_{GSR} \sim -168$ km s^{-1}). More recently, in QUEST data, Vivas et al. (2008) found a significant number of Blue Horizontal Branch stars at a similar velocity ($V_{GSR} \sim -171$ km s^{-1}) as well as two RRLs. They place the group at 11 ± 2 kpc, but note that the stars are near the faint limit of their sample and suggest that it may be the near side of a larger substructure. They believe it to be the same feature as that identified by Newberg et al., which has a quoted distance of 11–14 kpc. Vivas et al. note that the nominal 16% distance uncertainty in Newberg et al.'s data may in fact be up to 40%. It is thus not unreasonable to assume that the feature we have detected (at 16–21 kpc) is the same as that observed by both Newberg et al. and Vivas et al.. Based on their investigations, the latter conclude that none of the halo substructures they detected were due to the leading Sgr arm, nor did Newberg et al. associate these stars with Sgr debris. However, we propose that this group of stars with highly negative radial velocities is indeed associated with the leading Sgr Stream, but that these stars were stripped on an *earlier* orbit (see *debris-d*) than that considered by these authors *(debris-c)*. For the most convincing match of velocities and distances, the negative velocity data in this region favours the prolate model. We must keep in mind, however, the small number of data points available.

To broadly summarise the information from our VSS region stars, Figure 4.8 presents generalised histograms of V_{GSR} for these 11 RRLs and for simulated stars in the relevant $\Lambda_\odot$ range, at the relevant distance. The inset histograms reveal that the oblate model predicts the most stars within the observed distance range. It is also the model which best reproduces the observed stars (red line) with positive radial velocities, with a slight peak (cyan line) around the VSS velocity at ~ 130 km s^{-1} (see §3.1). The negative velocity peak in the data, on the other hand, is best fit by the prolate model, particularly when an augmented distance range (green line) is considered. Only a small number of simulated stars, however, were predicted to be at the observed distance. While these histograms provide a more quantitative and

potentially helpful way of looking at the data, one must bear in mind that when summing over 30° of $\Lambda_\odot$, important information regarding the variation of $V_{\rm GSR}$ with $\Lambda_\odot$ is lost. We therefore caution that the histograms do not tell the whole story, a better impression of which is gained from examination of Figure 4.3.
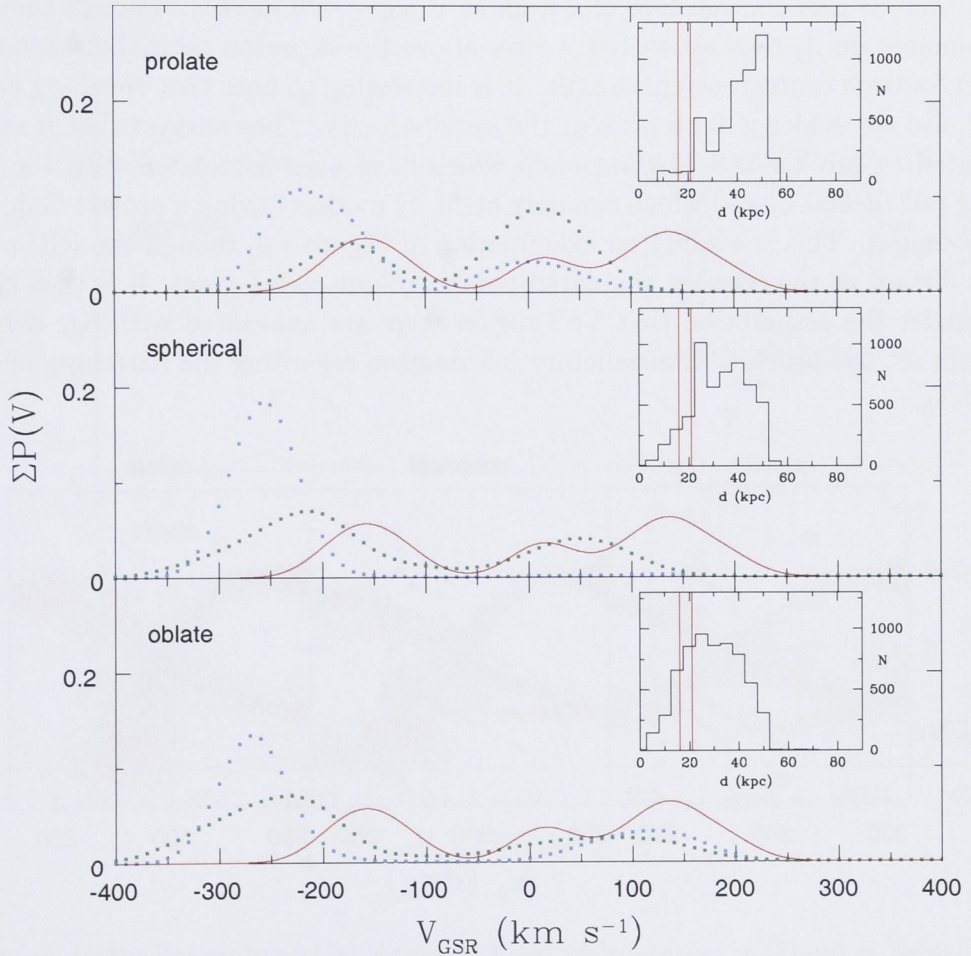
Figure 4.8: Generalised histogram of $V_{\rm GSR}$ (with kernel of 20 km s^{-1}) for the 11 observed RRLs in the VSS region *(red solid lines)* and for simulated stars between $\Lambda_\odot = 260°$ and $\Lambda_\odot = 290°$ at heliocentric distances $d = 16$–21 kpc *(cyan dotted lines)* and $d = 6$–31 kpc *(green dotted lines)*. The model halo potential is prolate *(top)*, spherical *(middle)* or oblate *(bottom)*. The total number of model stars in the selected $\Lambda_\odot$ and d ranges has been normalised to the number of observed stars. The inset histograms show the distance distribution of simulated stars for each halo potential in the selected $\Lambda_\odot$ range. Note that Law et al. (2005) added a 17% artificial random distance scatter to the simulated particles to mimic the photometric distance error in the 2MASS sample. The red lines indicate the distance range of the observed data.

As touched upon above, DZV06's data set can potentially provide additional information on the shape of the Galactic halo potential, if their RRLs are considered in the context of Sgr debris. The RRLs which they classify as members of the VSS, along with other positive velocity stars, were examined above. For completeness, Figure 4.9 shows DZV06's full set of 18 RRLs (along with our 11 VSS region RRLs) plotted over LJM05's models and Figure 4.10 shows the corresponding generalised histograms for DZV06's data. Apart from the peak at $V_{\mathrm{GSR}} \sim 100$ km s^{-1} discussed above, there is also a suggestion of a peak at $V_{\mathrm{GSR}} \sim -75$ km s^{-1}. Though they do not comment on it, they show that it rises above the expected normal distribution in their 'outside central region' sample. It is interesting to note that Newberg et al. (2007) also see evidence for a peak at the same velocity. They suggest that it could be related to the 2MASS M giant stars which have been associated with the Sgr leading tail *(debris-c)* and which can only be fit by models having a prolate Galactic halo potential. This is evident on examination of Figure 4.9, though the RRLs are not as distant as the relevant simulated points (colour-coded grey). It is thus clear that, under the assumption that VSS region stars are associated with Sgr debris, this data set too provides contradictory information regarding the flattening of the dark halo.
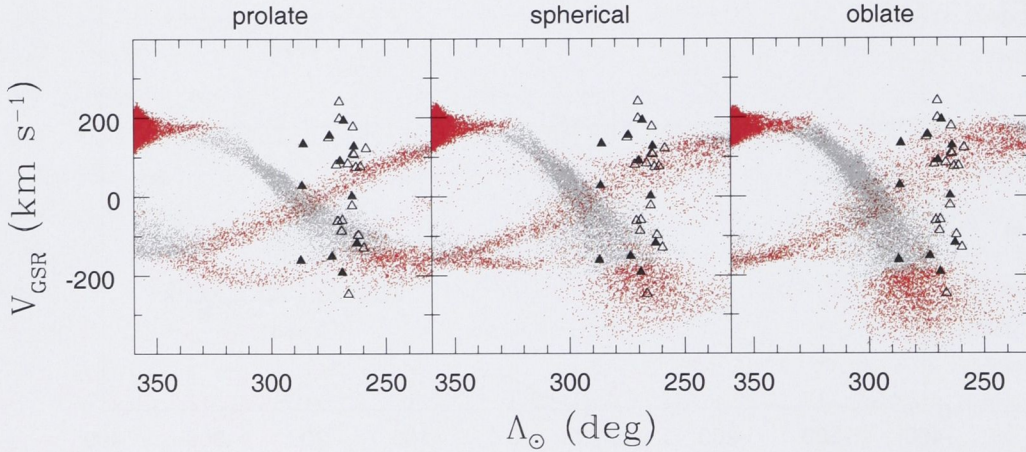
Figure 4.9: Radial velocities against $\Lambda_{\odot}$ from models with prolate *(left)*, spherical *(middle)* and oblate *(right)* Galactic halo potentials (Law et al., 2005). Red denotes simulated stars with heliocentric distances $d = 6$–31 kpc while grey denotes stars at all other distances. Overplotted are values for our data *(filled triangles)* and for Duffau et al.'s (2006) *(open triangles)* for RRLs in the VSS region.

As a final attempt to investigate the shape of the halo potential, we compared the reported radial velocities of Vivas et al.'s (2005) (hereafter VZG05) 16 RRLs to LJM05's models. These RRLs are located at a different angular separation from Sgr to our data, as shown in Figure 4.11, and are at a heliocentric distance of roughly 50 kpc (red simulated particles are between 40 and 65 kpc). Upon comparing their data with those of Helmi (2004a) and Martínez-Delgado et al. (2004), VZG05 conclude
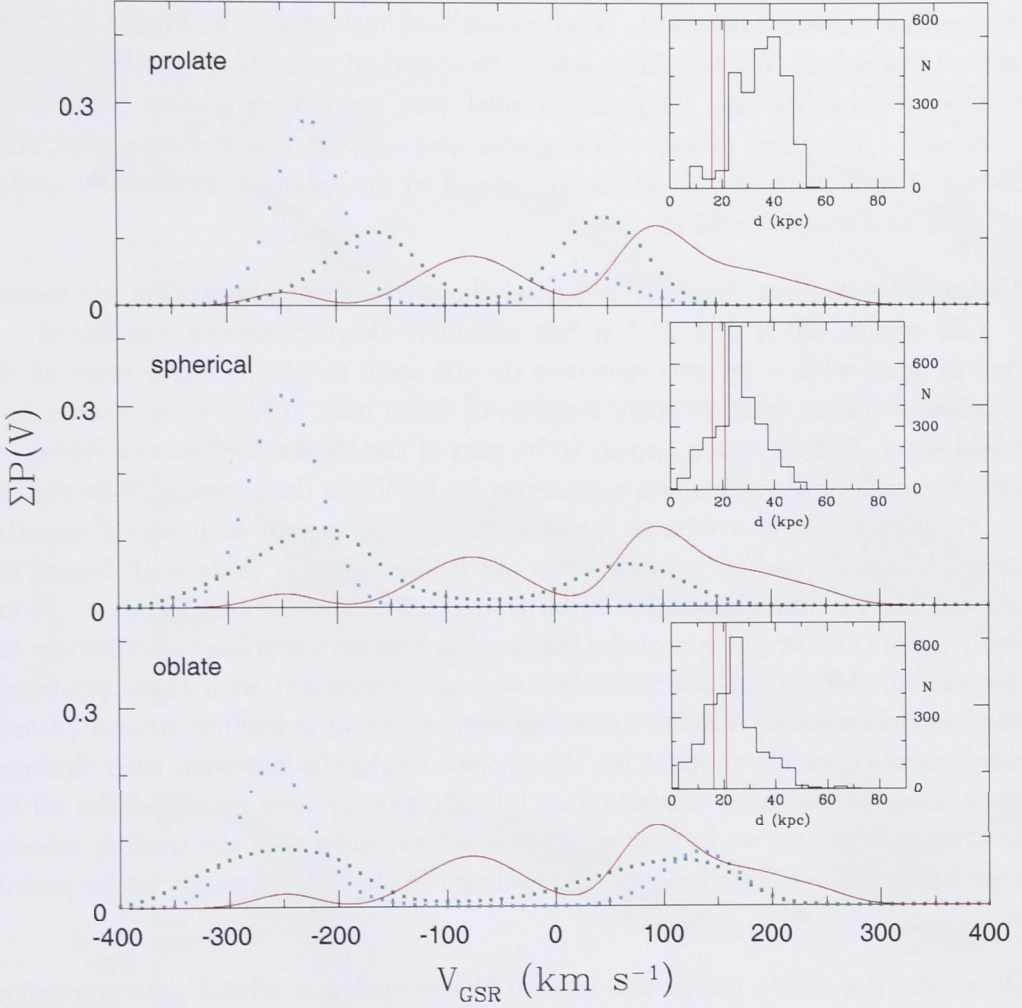
Figure 4.10: Generalised histogram of V_{GSR} (with kernel of 20 km s^{-1}) for Duffau et al.'s (2006) 18 observed RRLs in the VSS region *(red solid lines)* and for simulated stars between $\Lambda_\odot = 255°$ and $\Lambda_\odot = 275°$ at heliocentric distances $d = 16$–21 kpc *(cyan dotted lines)* and $d = 6$–31 kpc *(green dotted lines)*. The model halo potential is prolate *(top)*, spherical *(middle)* or oblate *(bottom)*. The total number of model stars in the selected $\Lambda_\odot$ and d ranges has been normalised to the number of observed stars. The inset histograms show the distance distribution of simulated stars for each halo potential in the selected $\Lambda_\odot$ range. Note that Law et al. (2005) added a 17% artificial random distance scatter to the simulated particles to mimic the photometric distance error in the 2MASS sample. The red lines indicate the distance range of the observed data.

that spherical and prolate models fit better than oblate models, though none of the fits are completely satisfactory. Comparison with LJM05's models reveals a similar conclusion. In Figure 4.11, the prolate model is clearly the best fit, with all RRLs except the two VZG05 identified as probable non-members appearing to belong to the leading stream *(debris-c)*. The generalised histograms in Figure 4.12 give the same impression. We note that while the spherical and oblate models produce progressively worse fits than the prolate model, they are not completely inconsistent with the data. The inset distance histograms also support the prolate choice, since it shows a clearer peak at $d = 50$ kpc compared to the spherical and oblate models which peak at distances $\sim$45 kpc.

Taking into account data for potential Sgr Stream members from all regions (i.e. VSS region, 20 h and 21.5 h Sgr regions), the conclusions are mixed. A number of stars with near zero velocities do not seem to fit any Sgr stream at the appropriate distance, though some fraction of these may in fact be contaminating halo field stars. Others which appear to be part of the old trailing stream *(debris-b)* in both Sgr and VSS regions (supplemented by DZV06's data) strongly favour the oblate model. On the other hand, a group in the VSS region with highly negative velocities, which appear to belong to the old leading stream *(debris-d)*, favour the prolate model. The association of a small group in DZV06's data at $V_{GSR} \sim -75$ km s^{-1} with a more recent portion of the leading Sgr Stream *(debris-c)* also favours the prolate model, though the observed distances are discrepant with those predicted. Finally, consideration of VZG05's observations of probable leading stream *(debris-c)* members also reveals support for the prolate model, in line with their findings. We thus come to the same conclusion as LJM05, namely that no model fits all the observational data and we further substantiate their note that the trailing velocity data are better fit by oblate halos, while leading velocity data strongly prefer prolate halos.

Since only the oblate model was able to fit the observed orbital pole precession, LJM05 favour this model, advocating that the inability of the oblate model to fit the leading velocity data could be remedied by appropriate variations to other free parameters. For example, they propose that more sophisticated models involving an evolution of orbital parameters and/or the strength of the Galactic potential may be necessary to fit all observational data. Given that RRL stars are members of an old stellar population (in comparison to younger M giant stars, for example), our observations have the advantage that they could potentially trace debris torn from Sgr several orbits ago. As such, they may be prime candidates for examination of the higher order effects that LJM05 hypothesise to be important for construction of a more accurate model. Moreover, since distances for RRLs are better established than for M giants, data from RRLs could place stronger constraints on models than the M giant data used in LJM05's models.
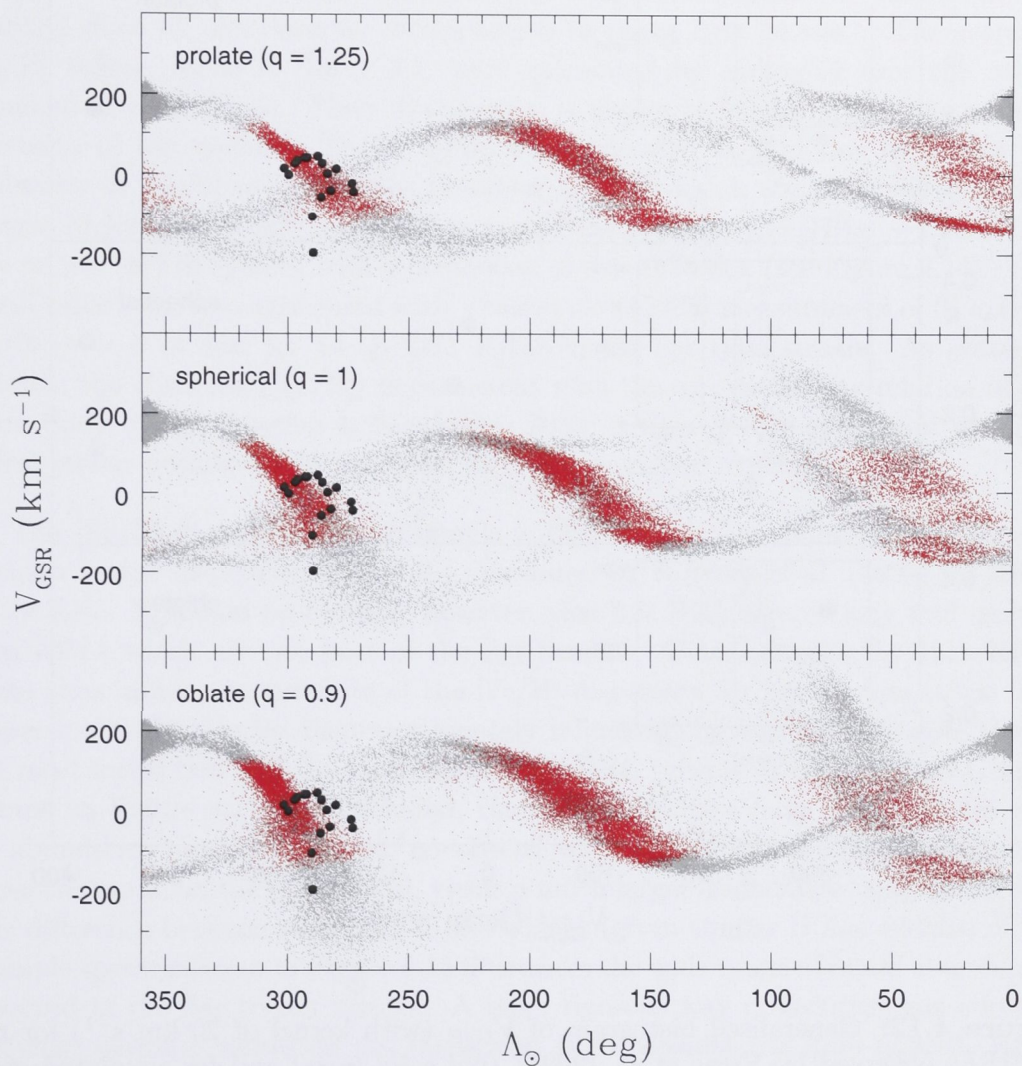
Figure 4.11: Radial velocities against $\Lambda_\odot$ from models with prolate *(top)*, spherical *(middle)* and oblate *(bottom)* Galactic halo potentials (Law et al., 2005). Red denotes simulated stars with heliocentric distances $d = 40$–65 kpc while grey denotes stars at all other distances. Overplotted *(circles)* are values for the 16 hypothesised Sgr Stream RRLs observed by Vivas et al. (2005) .
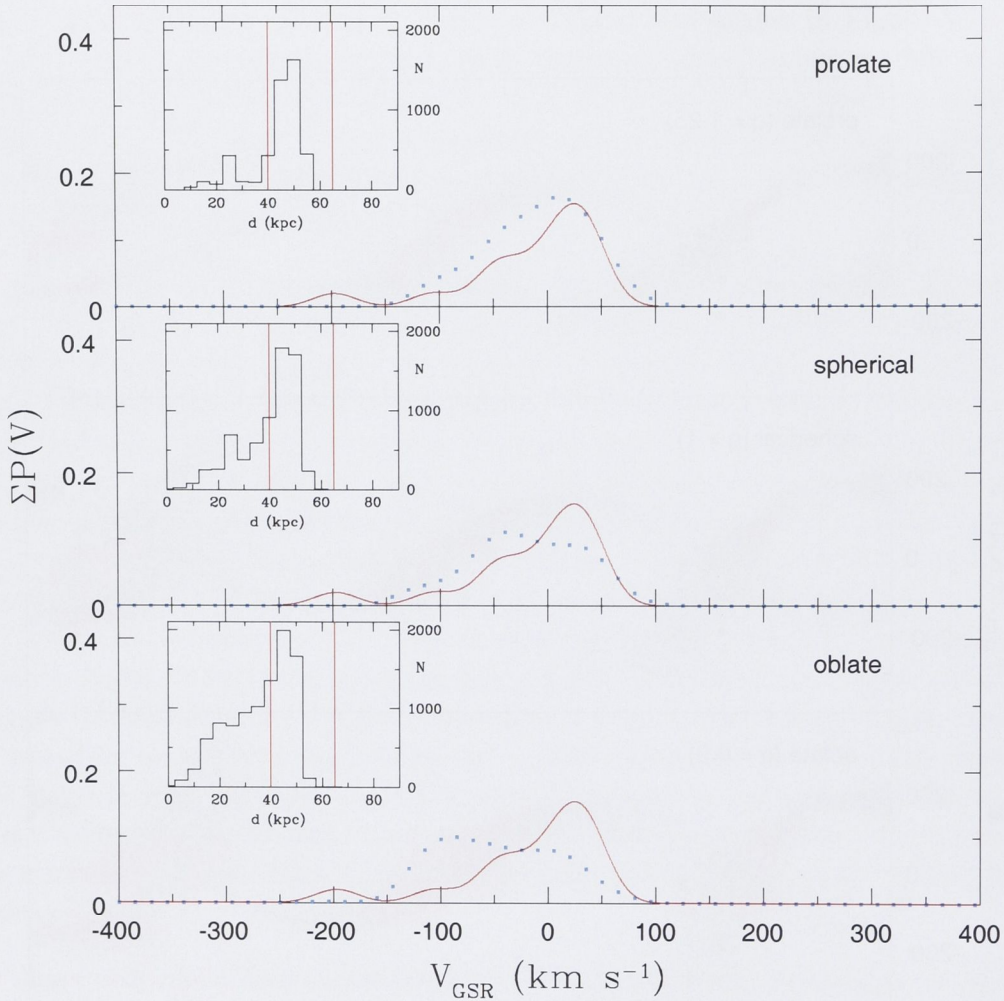
Figure 4.12: Generalised histogram of V_{GSR} (with kernel of 20 km s^{-1}) for the 16 RRLs observed by Vivas et al. (2005) *(red solid lines)* and for simulated stars between $\Lambda_\odot = 273°$ and $\Lambda_\odot = 301°$ at heliocentric distances $d = 40$–65 kpc *(cyan dotted lines)*. The model halo potential is prolate *(top)*, spherical *(middle)* or oblate *(bottom)*. The total number of model stars in the selected $\Lambda_\odot$ and d ranges has been normalised to the number of observed stars. The inset histograms show the distance distribution of simulated stars for each halo potential in the selected $\Lambda_\odot$ range. Note that Law et al. (2005) added a 17% artificial random distance scatter to the simulated particles to mimic the photometric distance error in the 2MASS sample. The red lines indicate the distance range of the observed data.

4.2 Metal abundances

Figure 4.13 displays values in the H3–W(K) plane at each observed phase for the 21 type *ab* RRLs in the 20 h and 21.5 h Sgr regions (note that one RR*ab* star was omitted since all observations corresponded to rising light phases). The systemic [Fe/H] values, listed in Table 4.1, were calculated by averaging over the values obtained at each phase. Their distribution is shown in Figure 4.14. The internal precision of the systemic [Fe/H] values was estimated as 0.11 dex by noting the difference in [Fe/H] values at each phase for an RRL which was observed at similar phases (0.580 and 0.583). Averaging across the sample, $\langle$[Fe/H]$\rangle = -1.79 \pm 0.08$ dex on our [Fe/H] system with a dispersion of $\sigma = 0.38$ dex (see Figure 4.14). This mean value is in close agreement with Vivas et al.'s (2005) measurement of $\langle$[Fe/H]$\rangle = -1.76$, $\sigma = 0.22$ dex, for 14 QUEST RRLs in the Sgr tidal stream. As noted by VZG05, the observed $\langle$[Fe/H]$\rangle$ is consistent with the age-metallicity relation of the main body of Sgr (Layden & Sarajedini, 2000) if these RRLs are coeval with the oldest stellar population in the body, as they are indeed expected to be.

The [Fe/H] dispersion of our sample is larger than that found by VZG05 and is closer to the dispersion of $\sigma = 0.4$ dex found by Kinman et al. (2000) for RRLs in the halo. It should be recalled, however, that our RRL sample may well include field RRLs which are not part of the Sgr Stream. Contamination by such RRLs could thus inflate our estimate of the [Fe/H] dispersion for Sgr Stream stars. The dispersion could also be disproportionately influenced by outliers. We note that if the most metal rich and the most metal poor RRL (visible as the outermost, small bumps on Figure 4.14) are excluded, the remaining stars have $\sigma = 0.23$ dex and an abundance range of 0.8 dex, consistent with the values of VZG05. Including those two stars, on the other hand, yields a much larger abundance range of 1.8 dex. The difference between the Ca II K line widths (given similar H line widths) of the example spectra shown in Figure 4.15 illustrates the wide range of metal abundances observed in the Sgr region sample. A more rigorous way of reducing the effect of outlying, extreme values on the dispersion is to consider the inter-quartile range (IQR). We obtain IQR = 0.46 dex which is larger than that for VZG05's data, IQR = 0.22 dex. It thus appears that the larger [Fe/H] dispersion in our Sgr Stream sample than in VZG05's is not driven solely by outlying values.

The differing abundance dispersions are perhaps unsurprising given that we are sampling a different part of the Sgr Stream than VZG05. The fact that the mean abundances agree raises the question of whether there is any pattern in mean [Fe/H] according to the part of the stream to which the RRLs belong. Indications of an age/metallicity gradient along the Sgr Stream have been observed, with stars stripped from Sgr on past perigalactic passages being older and more metal poor than the Sgr core and than stars stripped more recently (Majewski et al., 2003;
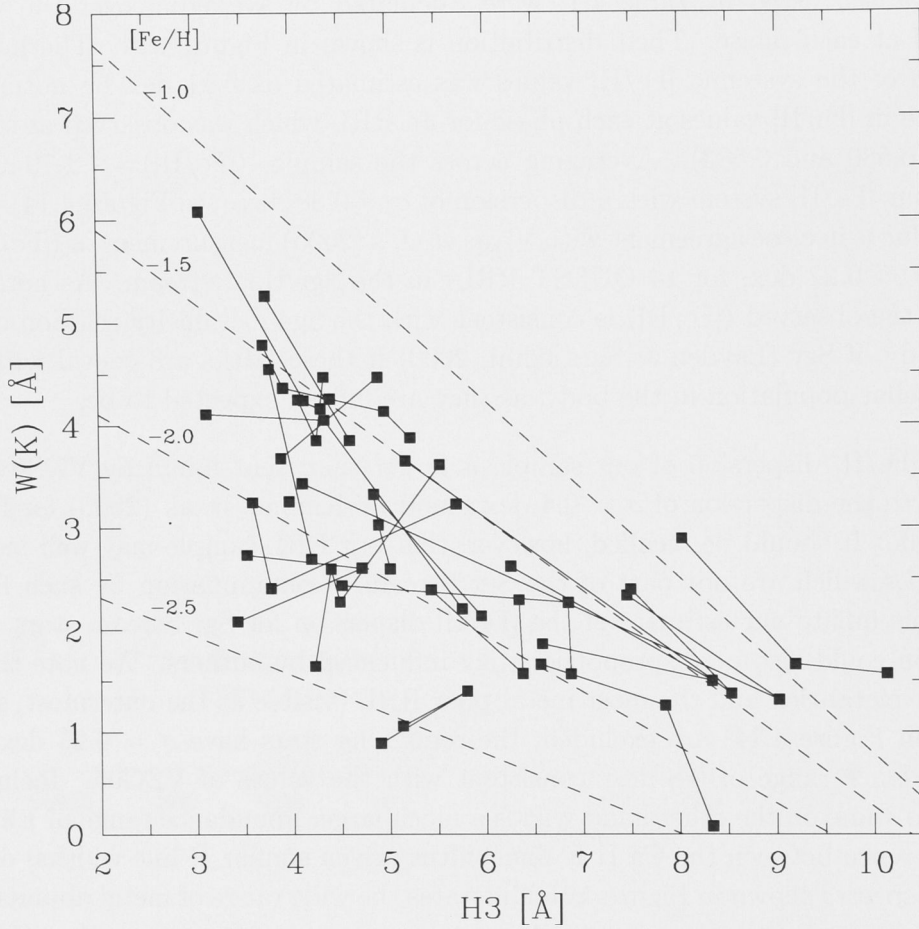
Figure 4.13: The pseudo-equivalent width of the Ca II K line, corrected for interstellar absorption, against the average width of Hδ, Hγ and Hβ for the 21 type *ab* RRLs in the Sgr region. Solid lines connect values for the same RRL observed at different phases. The dashed lines are the loci of stars having the indicated [Fe/H] value according to Layden's (1994) calibration.
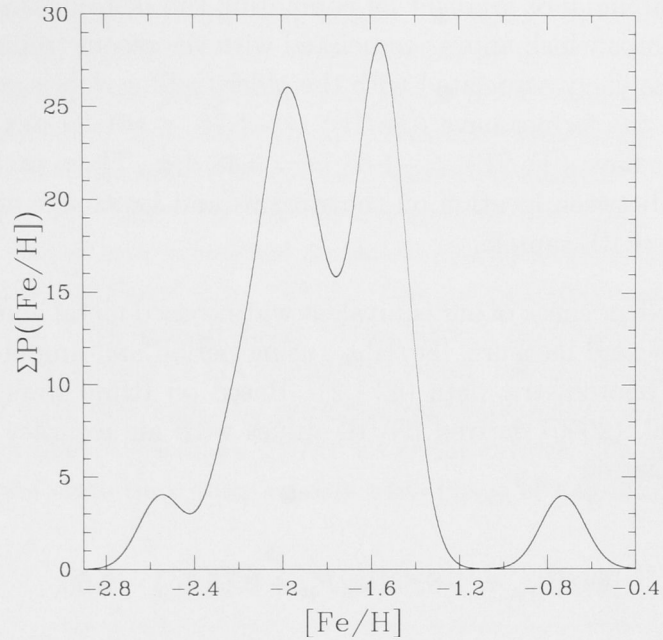
Figure 4.14: Generalised histogram of [Fe/H] (with kernel of 0.1 dex) for the 21 type *ab* RRLs in the Sgr region.
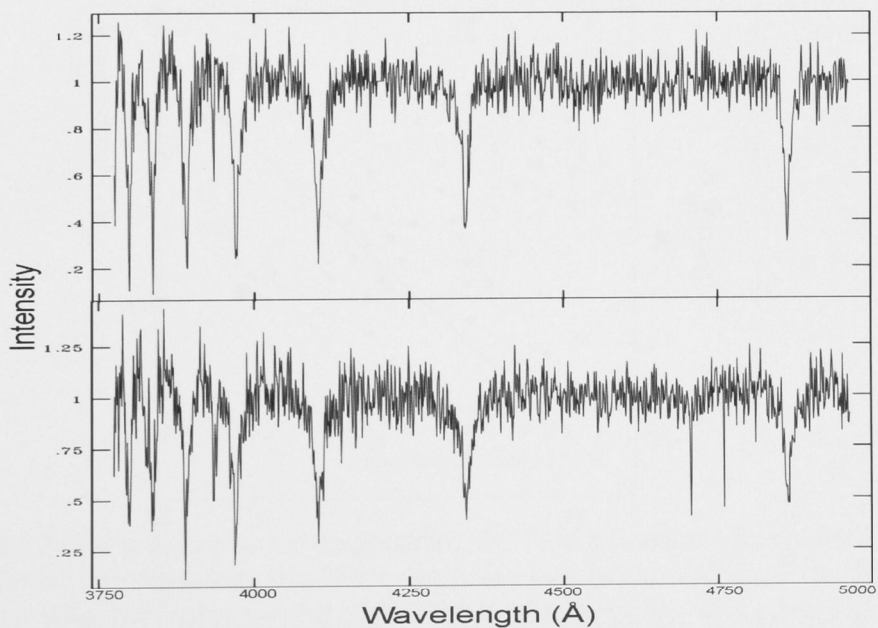
Figure 4.15: Example normalised spectra for RRLs in the Sgr region demonstrating the abundance range in our sample. *Top*: a metal poor RRL with [Fe/H]= −2.17. *Bottom*: a metal rich RRL with [Fe/H]= −0.73. Note that the spectrum for the metal rich RRL exhibits a stronger Ca II K line.

Martínez-Delgado et al., 2004; Bellazzini et al., 2006). We might then search for evidence of this abundance gradient by comparing the metallicities of RRLs in the 20 and 21.5 h clumps which appear associated with the recent trailing debris stream (*debris-a*) to those likely associated with the older trailing debris stream (*debris-b*). The six RRLs in the former have $\langle[\text{Fe/H}]\rangle = -1.76$, $\sigma = 0.24$ dex while the seven stars in the latter have $\langle[\text{Fe/H}]\rangle = -1.68$, $\sigma = 0.48$ dex. Thus, we find no evidence for a correlation between location on the stream (and hence age of stripping) with abundance in our RRL sample.

As an independent check of our equivalent width-based metal abundances, $[\text{Fe/H}]_{\text{EW}}$, we calculated a second measure, $[\text{Fe/H}]_{\text{PA}}$, using period and amplitude information gained from our photometric data (§2.1.2). Based on RR*ab* stars in M3, M5 and M15, Alcock et al. (2000) derived [Fe/H] values with an accuracy of 0.31 dex per star using the equation

$$[\text{Fe/H}]_{\text{PA}} = -8.85(\log P_{ab} + 0.15 A_V) - 2.60, \tag{4.1}$$

where P_{ab} is the period of the RRL and A_V is its amplitude in the V band.
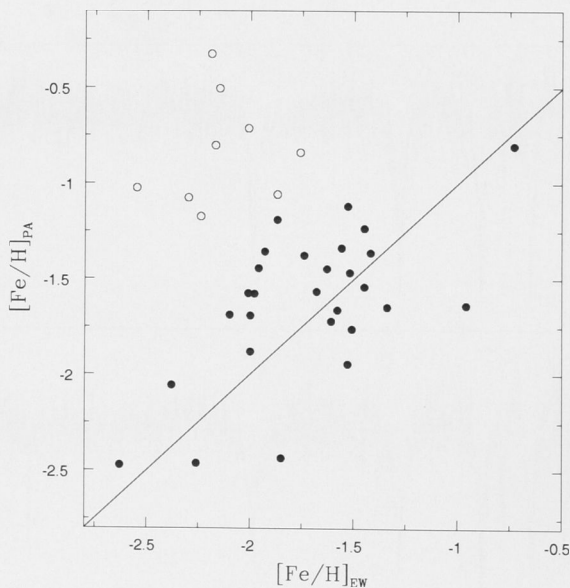
Figure 4.16: Metal abundances for the 37 spectroscopically followed up type *ab* RRLs in all regions, calculated using different methods. $[\text{Fe/H}]_{\text{PA}}$, calculated using Alcock et al.'s (2000) period-amplitude relationship is plotted against $[\text{Fe/H}]_{\text{EW}}$, calculated using equivalent widths, as described and calibrated by Layden (1994). For reference, the solid line shows $[\text{Fe/H}]_{\text{PA}} = [\text{Fe/H}]_{\text{EW}}$. Open circles are used to highlight points which deviate most significantly from this line.

Figure 4.16 displays $[Fe/H]_{PA}$ using the equation above against $[Fe/H]_{EW}$ for the 37 RR*ab* stars in our spectroscopic sample (across *all* regions) for which metal abundances could be calculated (i.e. spectra were obtained between phases 0 and 0.8). The nine data points plotted as open circles show relatively large deviations from the solid line at $[Fe/H]_{PA} = [Fe/H]_{EW}$. The period-amplitude diagram in Figure 4.17 helps to elucidate the nature of this discrepancy. It shows all 77 photometrically confirmed RRLs. The type *c* RRLs can be seen as the group of asterisks with shorter periods, falling in a somewhat parabolic shape, as predicted by Bono et al. (1997) and observed by Pritzl et al. (2002). The non-outlying points on Figure 4.16 (solid circles) follow a tight relationship in the period-amplitude diagram, while the outlying points on Figure 4.16 fall below this trend, having smaller amplitudes. It should be noted that although the period-amplitude relationship is known to be dependent on metallicity (Sandage, 1993), it cannot explain this group of stars with smaller amplitudes since they span a fairly wide range of metallicities.
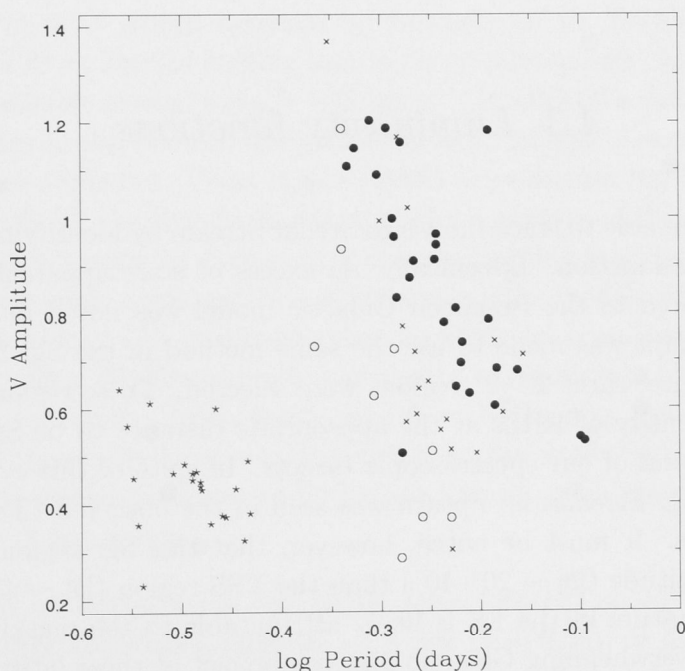
Figure 4.17: Period-amplitude diagram for the 77 photometrically confirmed RRLs in all regions. As expected, the RR*ab* stars are well separated from the RR*c* stars *(asterisks)*, with the latter having distinctly shorter periods. RRLs for which metal abundances were calculated from follow-up spectra are denoted by circles. The nine open circles are those stars which deviated most significantly from $[Fe/H]_{PA} = [Fe/H]_{EW}$ in Figure 4.16. Falling below the trend of the filled circles, these stars tend to have smaller determined amplitudes than expected based on their determined periods. Small crosses denote RR*ab* stars for which metal abundances were not calculated.

The notion that the period and amplitude-fitting routines we employed sometimes resulted in underestimates in amplitudes is illustrated by an overlap star between our sample and that of QUEST. While we arrived at similar periods, QUEST quoted a V amplitude of 0.99 (Vivas et al., 2004) compared to our value of 0.29. Due to being based on many more epochs than our data, QUEST's period and amplitude values are unquestionably the more accurate. We also note that their values place this star in line with the general period-amplitude trend. It is more than likely that others in our sample have inaccurately determined amplitudes (due to insufficient sampling of the light curve) and for these stars it is clear that Equation (4.1) should not be used. It is thus justifiable that, in this comparison between [Fe/H] measures, we omit the nine outlying stars on Figure 4.16 which are seen to have suspect amplitudes based on Figure 4.17. For the remaining 28 RRLs, the RMS of the $[Fe/H]_{PA}$ values from the $[Fe/H]_{PA} = [Fe/H]_{EW}$ fit is 0.35 dex. Given the uncertainty of 0.31 dex per star of Equation (4.1), the scatter of $[Fe/H]_{PA}$ from $[Fe/H]_{EW}$ can largely be explained by the combined uncertainties in the [Fe/H] measures. This provides independent evidence that we can have confidence in our equivalent width-based [Fe/H] values.

4.3 Luminosity functions

In §3.3 we were able to trace the Virgo Stellar Stream by identifying its signature in the luminosity function. Specifically, an excess of stars apparently peaking at $V \sim 19.5$ compared to the Besançon Galactic model was noted in certain $2° \times 2°$ regions. An attempt was made to use the same method in the Sgr Stream region. In the first instance, three $2° \times 2°$ regions were selected. These regions contained a relatively high density of RRLs at the appropriate distance to be Sgr tidal debris and included several of our spectroscopic targets. In spite of this evidence for the presence of the Sgr Stream, no upturn was seen in the observed LFs compared to the synthetic LFs. It must be noted, however, that this Sgr region is at a much lower Galactic latitude ($|b| \sim 20°–40°$) than the VSS region ($|b| \sim 45°–60°$). Thus the lack of a signature in the LF is likely attributable to the masking of any Sgr features by the overwhelming Galactic disk component at these latitudes.

4.4 Summary

Analysis of follow-up spectroscopy of 26 photometrically confirmed RRLs from a candidate list based on SEKBO survey data reveals a radial velocity distribution which does not appear consistent with a general halo population. Based on their location, the RRLs are likely to be associated with debris from the disrupting Sgr

dwarf galaxy. A comparison of the radial velocities with those predicted by the models of Law et al. (2005) supports this hypothesis. In the 21.5 h region, the group of stars with highly negative radial velocities ($V_{\rm GSR} \sim -175$ km s^{-1}) is predicted to be old trailing debris when the Galactic potential is modelled as oblate. On the other hand, the observed spread in radial velocities from -100–$+50$ km s^{-1} is poorly fit by any model at the appropriate distance. Either uncertainties in the model distances or contamination of our Sgr region sample by halo field RRLs could help to explain this.

Comparison of radial velocities of VSS region RRLs with the Sgr debris models reveals striking similarities in trends with $\Lambda_\odot$. Together with the evidence of spatial coincidence of these stars with the predicted debris streams, our results provide observational support for Martínez-Delgado et al.'s (2007) proposition that Sgr debris is in fact at least partially responsible for the overdensity in Virgo. A group of six RRLs (including the four stars identified as VSS members in §3.1) with positive $V_{\rm GSR}$ are well fit by the old trailing arm in the oblate model (and are consistent with Duffau et al.'s, 2006, data), while a slightly smaller group with highly negative $V_{\rm GSR}$ (consistent with groups detected by Newberg et al., 2007 and Vivas et al., 2008) are better fit by the old leading arm in the prolate model. In addition, the association of a possible group ($V_{\rm GSR} \sim -75$ km s^{-1}) in DZV06's data with the recent leading Sgr Stream also favours the prolate model, though observed distances are closer than those predicted. Vivas et al.'s (2005) more distant Sgr Stream sample is similarly better fit by the prolate model, again for a portion of the leading arm. We thus find further evidence for Law et al.'s observation that trailing debris is best fit by oblate models while leading debris is favours prolate models. That is, we are in agreement with Law et al.'s conclusion that no single orbit and/or potential can fit all the observed data. Further modelling is needed to investigate higher order effects such as orbital evolution. To this end, data from RRLs may prove useful as these old stars could potentially have been stripped from Sgr several orbits ago. The high accuracy of determined distances to RRLs provides an extra incentive to use these stars as probes of Sgr debris.

The 21 type *ab* RRLs in the Sgr region have $\langle [{\rm Fe/H}] \rangle = -1.79 \pm 0.08$ on our system and a large abundance range of ~ 1.8 dex ($\sigma = 0.35$), or 0.8 dex ($\sigma = 0.23$) omitting the two most extreme values. The interquartile range is 0.46 dex. The mean metallicity is consistent with that of Vivas et al. (2005) for Sgr tidal debris, though the spread in our data appears larger. Metal abundances derived from equivalent widths of spectra are consistent with those derived using the period-amplitude relation of Alcock et al. (2000), taking into account the combined errors of the two methods.

Limitless undying love which
Shines around me like a million suns
It calls me on and on
Across the universe

Lennon & McCartney

Conclusions and Future Work

The original aim of this project was to investigate, using RR Lyrae stars as tracers, substructure in the Galactic halo by focussing primarily on two known examples: the Virgo Stellar Stream and the Sagittarius Stream. We planned to use radial velocities, in addition to spatial information, to help clarify the nature of these substructures, gaining a better understanding of their locations, spatial extents and kinematics. The initial analysis of the VSS region RRLs revealed this stream to be large and diffuse, extending to the south of the declination limits of SDSS and QUEST coverage. Investigation into the possible association of the VSS region stars with the Sgr Stream, however, led to a somewhat unexpected discovery, though it had been foreshadowed by Martínez-Delgado et al. (2007). Namely, that our initial categorisation and labelling of our two follow-up regions, the 'VSS region' and the 'Sgr region', may well have been misleading from the outset.

The trends in radial velocity with orbital longitude of stars in the VSS region, including those identified as VSS members, point strongly towards their association with Sgr debris streams, as modelled by Law et al. (2005). Indeed, Martínez-Delgado et al. suggest that Duffau et al.'s (2006) detection of the VSS might in fact be the trailing Sgr Stream if the dark halo is modelled as oblate. With this shape for the halo potential, they show the VSS to overlap spatially with Sgr debris. DZV06's data, however, spanning a relatively small range in $\Lambda_\odot$, make it difficult to detect velocity gradients along the stream given the uncertainty in the measurements, although they do note this possibility. The data in the current project fortuitously overcomes this problem due to its larger spread in $\Lambda_\odot$. Upon comparison with LJM05's model, the association of six of the VSS region sample with the old Sgr

trailing stream is difficult to deny. These stars, along with a prominent group in the Sgr region with highly negative radial velocities (corresponding to a slightly older part of the trailing stream), strongly favour oblate models for the Galactic halo potential. Suspected leading arm data from our VSS region sample in addition to DZV06's and Vivas et al.'s (2005) samples, however, tell a different story in which prolate models are favoured. These findings echo those of LJM05 and reinforce the conclusion that the issue of dark halo shape cannot be definitively resolved with current models of the Sgr disruption.

LJM05 suggest that an evolution of the orbital parameters of Sgr over several Gyr may need to be considered. In addition, the Sgr dwarf itself may need to be modelled as a two component system, in which the dark matter is bound more loosely than the baryons. Warnick et al.'s (2008) N-body simulations of satellite disruption within 'live' (cosmological) host halos suggest that the situation may be far more complicated than previously envisioned. Their preliminary studies find little correlation between debris properties and host halo properties such as shape. They note that the host dark halo undergoes a complex mass accretion history and also comment that it cannot be easily modelled as a simple ellipsoid due to the wealth of substructure present. In contrast, Siegal-Gaskins & Valluri (2008) investigate the effects of dark matter substructure on tidal streams and find that halo shape and orbital path play a much more important role in the large-scale structure of the debris. However, they do note that substructure increases the clumpiness of the debris and changes the location of certain sections compared to the predictions from a smooth halo model. This could add an extra complication to studies such as the current one, where attempts are made to fit tidal debris models with data. For example, there is the possibility that apparent model distance errors (alluded to in §4.1) could be attributable to the effects of unknown dark matter substructures.

While the data presented in this thesis will no doubt be a great asset in helping to constrain improved models and to verify their success in predicting observed phenomena, it is also clear that the current analysis raises a myriad of questions. The most basic of these is whether the overdensity in Virgo can be solely attributed to Sgr debris, or whether there are overlapping features which conspire to produce the observed excess. Almost all the RRLs in the current study have radial velocities and distances which are consistent with either the old leading or the old trailing Sgr debris stream. In addition, DZV06's VSS region data show the suggestion of a group of stars with $V_{\mathrm{GSR}} \sim -75$ km s^{-1}, at the same velocity as a peak found by Newberg et al. (2007) and possibly related to the 2MASS M giant stars which have been associated with the recent Sgr leading tail. In this region, the other peak reported by Newberg et al., aside from the 100–130 km s^{-1} VSS peak, has a velocity consistent with a group of stars in the current study, which we showed to overlap with the old leading tail. Thus, there appears to be mounting evidence that the identified spatial overdensities in the VSS region could potentially all be related

to Sgr debris, albeit different portions of the streams. We must stress, however, that the radial velocity peaks discussed here (excluding the M giant sample) each consisted of between only four and nine stars. Clearly, larger samples will increase our confidence in any conclusions we draw about these groups of stars. The SEKBO survey catalogue alone provides a more than ample selection of RRLs stars in the VSS region which could potentially be followed up spectroscopically. This would seem to be a very useful endeavour to pursue.

The current project provides us with a better understanding of the location and extent of the overdensity in Virgo, extending it south of previous survey limits and revealing a somewhat unexpected association with Sgr debris. Clearly, the addition of radial velocity information is crucial in order to elucidate the nature of any overdensities uncovered via analysis of the spatial distribution of tracer populations. Rather than being a stream or structure with a simple velocity structure, the emerging picture of the overdensity in Virgo is rather complex. Based on the data currently available, there are indications that it comprises at least three groups of stars, each having a radial velocity signature which plausibly associates it with a section of the Sgr Stream. A question which arises is whether other regions of the halo are similarly dominated by complex substructures, or whether the region of overdensity in Virgo represents a special case, possibly due to the crossing of two or more sections of the Sgr Stream.

Not only is investigation into the radial velocity distributions of known substructures important in addressing this question, but there is also the likelihood that certain substructures are too diffuse to be detected spatially, yet could be revealed with appropriate spectroscopic information. Current and future astrometric and spectroscopic surveys, including the Radial Velocity Experiment (RAVE) (Steinmetz et al., 2006), the Sloan Extension for Galactic Underpinnings and Exploration (SEGUE) (Beers et al., 2004), the satellite Gaia (Perryman et al., 2001) and the Space Interferometry Mission (SIM) PlanetQuest, will considerably aid in uncovering such substructures, if they exist. Such surveys will furnish us with a greatly enhanced view of the halo, adding an exciting new dimension to our understanding of the role of accretion in galaxy formation. In the optical domain, surveys such as SkyMapper (Keller et al., 2007), the Visible and Infrared Survey Telescope for Astronomy (VISTA), OmegaCam on the Very Large Telescope (VLT) Survey Telescope, the Panoramic Survey Telescope and Rapid Response System (Pan-Starrs) [3] and the Large Synoptic Survey Telescope (LSST) [4] will give us unprecedented maps of the deepest, uncharted realms of the Galactic halo. This comprehensive set of astrometric, spectroscopic and photometric data, together with increasingly sophisticated models of satellite disruption, promises to bring us ever closer to unravelling the mysteries of the formation of the Milky Way and of galaxies across the universe.

---

[3]http://pan-starrs.ifa.hawaii.edu/public/
[4]http://www.lsst.org

APPENDIX

Table 1: Photometric data summary

ID	α (J2000.0)	δ (J2000.0)	$\langle V \rangle$	$\langle R \rangle$	$\langle V - R \rangle_0$	n_{obs}	Classification	Period (days)	V Amplitude
96102-170	12 24 15.67	-01 49 14.52	17.02	16.83	0.174	15	RRab	0.525	0.286
96637-458	08 48 02.53	17 02 45.92	17.19	16.68	0.499	6	non-variable	-	-
97883-402	13 51 34.58	-11 46 40.63	17.30	17.06	0.199	5	RRab	0.542	0.718
97890-199	13 43 04.44	-11 34 05.74	16.34	16.18	0.130	6	RRc	0.350	0.374
97890-1542	13 45 14.61	-11 12 09.57	17.24	17.09	0.105	7	unclassified variable	-	-
99747-73	21 14 09.39	-17 36 32.90	17.09	16.91	0.135	8	RRab	0.517	0.724
99752-96	21 33 35.19	-16 07 05.52	17.08	16.93	0.098	15	RRc	0.324	0.466
101745-82	02 02 59.34	11 02 07.20	16.51	16.02	0.443	8	non-variable	-	-
101751-216	02 11 41.33	03 29 41.10	15.03	14.97	0.036	9	RRc	0.347	0.377
102253-790	03 20 38.35	15 53 01.72	18.17	17.69	0.396	8	non-variable	-	-
102292-1096	21 20 11.59	-14 51 13.75	17.22	16.98	0.194	14	RRab	0.570	0.965
102297-1488	21 16 05.66	-15 53 20.61	17.19	17.02	0.122	11	RRab	0.643	0.786
102601-400	21 28 51.69	-16 12 57.11	16.94	16.71	0.203	5	RRab	0.603	0.695
102601-1489	21 27 39.03	-16 03 56.87	17.35	17.09	0.226	15	RRab	0.803	0.531
103170-481	03 48 07.77	18 15 13.80	15.60	15.28	0.130	8	W-UMa	0.590	0.303
103207-176	01 43 09.85	10 13 18.08	15.91	15.72	0.123	7	non-variable	-	-
104394-240	08 44 32.11	07 57 09.90	15.15	14.80	0.320	11	W-UMa	0.342	0.601
104395-1233	08 51 56.36	07 57 19.66	18.57	18.30	0.231	8	non-variable	-	-
104410-181	03 19 05.03	09 08 41.95	17.00	16.71	0.143	9	RRab	0.544	0.587
104410-220	03 19 04.26	09 14 20.32	15.13	14.77	0.201	9	RRab	0.664	0.590
104638-2589	07 37 32.34	11 15 51.86	19.09	19.00	0.069	11	RRab	0.521	1.169
105287-296	11 24 18.84	05 06 04.73	17.18	17.00	0.155	9	RRab	0.696	0.712
105494-895	09 15 03.14	14 24 45.80	18.84	18.66	0.160	8	non-variable	-	-
105648-222	13 51 34.58	-09 35 49.90	17.15	16.96	0.163	7	RRab	0.472	1.146

Table 1 (cont'd)

ID	α (J2000.0)	δ (J2000.0)	$\langle V \rangle$	$\langle R \rangle$	$\langle V - R \rangle_0$	n_{obs}	Classification	Period (days)	V Amplitude
106139-90	10 38 19.41	−01 24 23.28	15.54	15.12	0.388	6	W-UMa	0.283	0.456
106586-211	16 02 54.59	−23 41 57.16	15.47	15.19	0.173	9	RRab	0.596	0.645
106591-2906	16 07 51.54	−24 03 40.73	15.51	15.20	0.208	9	unclassfied variable	-	-
106592-1877	16 05 14.83	−23 54 48.64	15.43	15.16	0.188	9	unclassfied variable	-	-
107398-355	16 10 51.23	−19 18 25.11	16.35	15.80	0.294	8	non-variable	-	-
107434-394	10 50 31.27	06 28 54.83	17.32	17.12	0.183	8	RRc	0.327	0.469
107539-4920	11 52 22.98	01 18 09.02	17.37	16.87	0.489	7	unclassfied variable	-	-
107552-323	12 34 12.69	−06 20 32.97	16.82	16.65	0.165	9	RRab	0.605	0.738
108145-212	14 00 53.27	−10 19 06.97	17.22	17.03	0.166	5	RRab	0.559	0.656
108227-529	12 15 24.20	−03 38 43.28	17.24	17.10	0.107	19	RRc	0.310	0.466
108237-459	13 54 43.43	−14 44 25.75	16.44	16.09	0.292	7	Algol	0.444	1.369
108407-552	12 50 09.73	−08 45 32.69	17.24	17.14	0.077	16	RRc	0.279	0.565
109247-528	13 42 08.15	−12 17 03.39	17.06	16.87	0.147	7	RRc	0.331	0.431
109463-3964	19 51 25.73	−19 34 58.68	17.38	17.04	0.249	9	RRab	0.525	1.158
109464-5627	19 48 44.48	−20 07 55.96	17.50	17.33	0.100	14	RRab	0.500	0.993
109489-2379	19 49 32.88	−20 05 21.50	17.33	17.10	0.170	12	RRab	0.551	0.371
109489-3076	19 48 50.58	−19 56 38.05	17.25	16.95	0.240	12	RRab	0.795	0.539
109582-3724	19 47 37.10	−19 49 35.72	17.49	17.31	0.114	12	RRab	0.497	1.090
109700-853	13 37 58.92	−12 46 19.58	17.24	17.03	0.165	7	RRc	0.274	0.642
110211-216	13 53 43.46	−08 26 40.43	17.05	16.85	0.166	6	RRab	0.534	1.020
110735-595	21 16 02.53	−14 16 59.35	17.07	16.89	0.144	11	RRab	0.489	1.204
110735-919	21 14 25.80	−13 57 27.62	17.42	17.15	0.228	12	non-variable	-	-
110738-411	21 36 47.31	−16 36 49.18	17.24	16.94	0.268	13	RRab	0.596	0.810

Table 1 (cont'd)

ID	α (J2000.0)	δ (J2000.0)	$\langle V \rangle$	$\langle R \rangle$	$\langle V - R \rangle_0$	n_{obs}	Classification	Period (days)	V Amplitude
110753-346	21 30 51.22	-16 38 51.28	16.96	16.78	0.149	6	RRab	0.570	0.943
110823-641	21 06 56.76	-18 51 00.14	17.17	17.04	0.089	9	RRc	0.318	0.485
110827-579	21 34 26.07	-17 18 32.31	17.06	16.79	0.241	15	RRab	0.652	0.605
110828-1100	21 05 39.67	-19 06 36.28	17.05	16.83	0.183	9	RRab	0.458	0.934
111945-745	21 50 08.21	-16 29 28.13	17.07	16.77	0.256	5	unclassfied variable	-	-
113345-1032	21 38 47.20	-17 06 58.41	17.16	17.03	0.099	12	RRc	0.370	0.381
114421-242	00 28 58.31	01 35 38.43	16.81	16.67	0.114	6	RRab	0.564	0.510
114791-928	21 08 08.90	-14 01 46.01	17.27	17.08	0.154	13	unclassfied variable	-	-
114793-1530	21 06 36.25	-13 39 13.42	17.17	17.02	0.112	11	RRc	0.338	0.360
115125-69	03 21 03.38	14 08 58.25	16.58	16.16	0.269	9	RRab	0.527	0.772
115213-329	03 23 36.23	14 47 54.25	15.50	15.09	0.293	12	RRab	0.625	0.505
115381-349	21 45 05.42	-15 40 27.54	16.80	16.56	0.204	6	RRab	0.589	0.370
115381-767	21 42 56.55	-15 53 35.89	17.28	17.07	0.175	6	RRab	0.508	1.188
115511-269	03 22 28.88	13 30 59.29	16.74	16.34	0.129	10	RRab	0.531	0.571
115545-172	03 29 12.27	12 50 17.09	15.28	15.16	-0.143	10	unclassfied variable	-	-
115638-118	01 26 49.56	08 30 45.24	15.73	15.49	0.209	8	non-variable	-	-
115709-124	01 31 19.61	06 47 18.32	17.22	16.91	0.289	8	non-variable	-	-
116385-432	02 10 44.39	12 45 09.71	17.88	17.59	0.192	8	RRab	0.547	0.641
116709-1029	03 29 23.66	16 37 52.33	17.58	17.27	0.203	9	unclassfied variable	-	-
116920-426	02 12 42.68	11 19 57.14	17.90	17.52	0.274	9	RRab	0.575	0.554
116949-88	02 14 10.60	12 38 40.94	16.00	15.68	0.241	9	RRab	0.583	0.575
117300-672	03 24 48.45	18 05 07.41	17.30	16.84	0.386	8	W-UMa	0.365	0.325
117607-696	07 53 01.35	16 20 28.56	15.63	15.11	0.503	11	W-UMa	0.294	0.613

Table 1 (cont'd)

ID	α (J2000.0)	δ (J2000.0)	$\langle V \rangle$	$\langle R \rangle$	$\langle V - R \rangle_0$	n_{obs}	Classification	Period (days)	V Amplitude
117777-2199	08 01 18.98	12 09 38.38	19.47	19.25	0.203	9	non-variable	-	-
117937-1180	09 26 51.14	11 10 39.42	18.76	18.66	0.082	9	non-variable	-	-
119120-368	09 35 24.16	11 08 35.88	15.72	15.22	0.483	10	unclassfied variable	-	-
119516-139	10 13 39.37	04 54 12.96	16.74	16.51	0.211	8	RRab	0.652	0.741
119827-670	12 37 14.75	−06 24 47.70	16.95	16.79	0.147	16	RRab	0.615	0.631
120173-523	12 59 07.20	−09 15 23.90	17.03	16.89	0.114	8	RRc	0.324	0.452
120185-77	12 31 33.36	−00 20 10.39	16.87	16.71	0.138	14	RRab	0.687	0.679
120219-92	13 47 41.47	−15 10 26.72	16.39	16.23	0.103	7	unclassfied variable	-	-
120679-336	12 36 40.39	−08 20 33.49	17.25	17.09	0.141	17	RRab	0.515	0.998
120698-392	13 35 41.49	−13 50 31.02	17.25	17.10	0.120	9	RRc	0.330	0.448
120857-475	13 42 20.97	−14 54 49.81	16.41	16.19	0.172	7	RRab	0.458	1.187
121087-197	13 59 09.00	−06 17 03.35	17.13	16.87	0.237	6	non-variable	-	-
121194-205	12 47 39.12	−10 28 09.41	16.79	16.70	0.061	16	RRc	0.330	0.438
121242-188	12 45 26.88	−13 00 32.31	16.86	16.78	0.051	14	RRc	0.358	0.433
121817-2385	16 03 50.77	−26 25 36.16	15.45	15.20	0.151	9	RRab	0.520	0.832
121906-2336	15 58 19.98	−27 31 46.81	15.74	15.52	0.121	10	RRc	0.368	0.491
122112-595	16 06 24.29	−26 16 46.23	15.52	15.23	0.175	8	RRab	0.536	0.874
122156-1114	16 02 19.21	−27 20 46.82	15.54	15.34	0.067	9	RRc	0.289	0.231
122214-1315	16 03 44.83	−27 12 58.46	16.12	15.73	0.199	9	RRab	0.541	0.909
122240-33	13 39 09.22	−17 14 31.55	16.39	16.22	0.124	6	RRab	0.493	0.626
124518-1558	21 06 42.10	−21 34 53.09	17.15	16.94	0.183	6	unclassfied variable	-	-
125766-526	21 56 31.86	−15 44 38.17	17.28	16.99	0.261	6	unclassfied variable	-	-
125812-515	21 48 49.46	−16 49 53.14	17.28	17.05	0.203	5	unclassfied variable	-	-

Table 1 (cont'd)

ID	α (J2000.0)	δ (J2000.0)	$\langle V \rangle$	$\langle R \rangle$	$\langle V - R \rangle_0$	n_{obs}	Classification	Period (days)	V Amplitude
125857-20	20 54 26.39	−13 52 16.61	17.06	16.83	0.207	9	RRab	0.655	0.683
126040-78	21 07 03.45	−20 52 49.28	17.24	17.02	0.180	8	RRab	0.580	0.780
126093-1135	21 11 09.55	−21 37 29.50	17.01	16.84	0.134	8	RRab	0.464	1.108
126245-633	21 24 11.98	−20 37 48.52	17.07	17.04	0.004	7	non-variable	-	-
126245-763	21 24 55.10	−20 26 55.45	17.25	17.02	0.181	6	RRab	0.517	0.960
126536-714	21 14 36.92	−22 20 23.28	17.19	17.12	0.039	7	RRab	0.526	0.506
127008-210	00 40 56.66	−02 08 03.07	16.88	16.61	0.262	5	RRab	0.568	0.912
127605-345	01 07 44.97	−00 24 37.72	17.64	17.53	0.086	8	non-variable	-	-
127679-18	01 17 42.03	−02 08 20.06	15.92	15.75	0.144	8	RRab	0.589	0.513
127806-85	00 25 12.59	−03 31 29.75	17.22	17.09	0.095	6	RRab	0.643	1.183
127806-438	00 25 23.38	−03 15 22.88	17.24	17.04	0.169	6	RRc	0.286	0.358
128320-7	01 26 56.32	04 12 26.31	15.52	15.29	0.218	10	unclassfied variable	-	-
128416-544	00 12 52.83	05 02 56.71	17.17	16.98	0.176	6	RRab	0.430	0.730

Note. — Units of right ascension are hours, minutes, and seconds, and units of declination are degrees, arcminutes, and arcseconds.

References

Adelman-McCarthy, J. K. et al. 2008, ApJS, 175, 297

Alcock, C. et al. 2000, AJ, 119, 2194

Bahcall, J. N., & Soneira, R. M. 1980, ApJS, 44, 73

Beers, T. C. 1990, AJ, 99, 323

Beers, T. C., Allende Prieto, C., Wilhelm, R., Yanny, B., & Newberg, H. 2004, Publications of the Astronomical Society of Australia, 21, 207

Bell, E. F. et al. 2008, ApJ, 680, 295

—. 2007, ArXiv e-prints, 706

Bellazzini, M., Newberg, H. J., Correnti, M., Ferraro, F. R., & Monaco, L. 2006, A&A, 457, L21

Belokurov, V. et al. 2007a, ApJ, 657, L89

—. 2006, ApJ, 642, L137

—. 2007b, ApJ, 654, 897

Binney, J., & Merrifield, M. 1998, Galactic Astronomy (Princeton: Princeton Univ. Press)

Bono, G., Caputo, F., Santolamazza, P., Cassisi, S., & Piersimoni, A. 1997, AJ, 113, 2209

Brown, W. R., Geller, M. J., Kenyon, S. J., Kurtz, M. J., Allende Prieto, C., Beers, T. C., & Wilhelm, R. 2005, AJ, 130, 1097

Bullock, J. S., & Johnston, K. V. 2005, ApJ, 635, 931

Carollo, D. et al. 2007, Nature, 450, 1020

Chiba, M., & Beers, T. C. 2000, AJ, 119, 2843

De Silva, G. M., Freeman, K. C., Asplund, M., Bland-Hawthorn, J., Bessell, M. S., & Collet, R. 2007, AJ, 133, 1161

Diemand, J., Kuhlen, M., & Madau, P. 2007, ApJ, 657, 262

Dohm-Palmer, R. C. et al. 2001, ApJL, 555, L37

Duffau, S., Zinn, R., Vivas, A. K., Carraro, G., Méndez, R. A., Winnick, R., & Gallart, C. 2006, ApJ, 636, L97

Eggen, O. J., Lynden-Bell, D., & Sandage, A. R. 1962, ApJ, 136, 748

Fellhauer, M. et al. 2006, ApJ, 651, 167

Freeman, K., & Bland-Hawthorn, J. 2002, ARA&A, 40, 487

Freeman, K. C., & Rodgers, A. W. 1975, ApJ, 201, L71+

Gilmore, G., & Reid, N. 1983, MNRAS, 202, 1025

Harding, P., Morrison, H. L., Olszewski, E. W., Arabadjis, J., Mateo, M., Dohm-Palmer, R. C., Freeman, K. C., & Norris, J. E. 2001, AJ, 122, 1397

Helmi, A. 2004a, MNRAS, 351, 643

—. 2004b, ApJ, 610, L97

Helmi, A., & White, S. D. M. 2001, MNRAS, 323, 529

Helmi, A., White, S. D. M., de Zeeuw, P. T., & Zhao, H. 1999, Nature, 402, 53

Ibata, R., Lewis, G. F., Irwin, M., Totten, E., & Quinn, T. 2001, ApJ, 551, 294

Ibata, R. A., Gilmore, G., & Irwin, M. J. 1994, Nature, 370, 194

Ibata, R. A., Irwin, M. J., Lewis, G. F., Ferguson, A. M. N., & Tanvir, N. 2003, MNRAS, 340, L21

Ivezić, Ž. et al. 2000, AJ, 120, 963

Johnston, K. V., Bullock, J. S., Sharma, S., Font, A., Robertson, B. E., & Leitner, S. N. 2008, ArXiv e-prints, 807

Johnston, K. V., Majewski, S. R., Siegel, M. H., Reid, I. N., & Kunkel, W. E. 1999, AJ, 118, 1719

Jones, R. V., Carney, B. W., & Latham, D. W. 1988, ApJ, 326, 312

Jurić, M. et al. 2008, ApJ, 673, 864

Keller, S. C., Murphy, S., Prior, S., DaCosta, G., & Schmidt, B. 2008, ApJ, 678, 851

Keller, S. C. et al. 2007, Publications of the Astronomical Society of Australia, 24, 1

Kinman, T., Castelli, F., Cacciari, C., Bragaglia, A., Harmer, D., & Valdes, F. 2000, A&A, 364, 102

Klypin, A., Kravtsov, A. V., Valenzuela, O., & Prada, F. 1999, ApJ, 522, 82

Kundu, A. et al. 2002, ApJ, 576, L125

Law, D. R., Johnston, K. V., & Majewski, S. R. 2005, ApJ, 619, 807

Layden, A. C. 1994, AJ, 108, 1016

Layden, A. C., & Sarajedini, A. 2000, AJ, 119, 1760

Liu, T., & Janes, K. A. 1989, ApJS, 69, 593

Majewski, S. R., Munn, J. A., & Hawley, S. L. 1994, ApJL, 427, L37

Majewski, S. R., Siegel, M. H., Kunkel, W. E., Reid, I. N., Johnston, K. V., Thompson, I. B., Landolt, A. U., & Palma, C. 1999, AJ, 118, 1709

Majewski, S. R., Skrutskie, M. F., Weinberg, M. D., & Ostheimer, J. C. 2003, ApJ, 599, 1082

Martínez-Delgado, D., Gómez-Flechoso, M. Á., Aparicio, A., & Carrera, R. 2004, ApJ, 601, 242

Martínez-Delgado, D., Peñarrubia, J., Jurić, M., Alfaro, E. J., & Ivezić, Z. 2007, ApJ, 660, 1264

Mateo, M. L. 1998, ARA&A, 36, 435

Moody, R., Schmidt, B., Alcock, C., Goldader, J., Axelrod, T., Cook, K. H., & Marshall, S. 2003, Earth Moon and Planets, 92, 125

Moore, B., Ghigna, S., Governato, F., Lake, G., Quinn, T., Stadel, J., & Tozzi, P. 1999, ApJL, 524, L19

Morrison, H. L. et al. 2008, ArXiv e-prints, 804

Morrison, H. L., Mateo, M., Olszewski, E. W., Harding, P., Dohm-Palmer, R. C., Freeman, K. C., Norris, J. E., & Morita, M. 2000, AJ, 119, 2254

Newberg, H. J., Yanny, B., Cole, N., Beers, T. C., Re Fiorentin, P., Schneider, D. P., & Wilhelm, R. 2007, ApJ, 668, 221

Newberg, H. J. et al. 2003, ApJ, 596, L191

—. 2002, ApJ, 569, 245

Norris, J. E. 1994, ApJ, 431, 645

Oke, J. B. 1966, ApJ, 145, 468

Perryman, M. A. C. et al. 2001, A&A, 369, 339

Preston, G. W. 1959, ApJ, 130, 507

Preston, G. W., Shectman, S. A., & Beers, T. C. 1991, ApJ, 375, 121

Pritzl, B. J., Armandroff, T. E., Jacoby, G. H., & Da Costa, G. S. 2002, AJ, 124, 1464

Robin, A. C., Reylé, C., Derrière, S., & Picaud, S. 2003, A&A, 409, 523

Sandage, A. 1993, AJ, 106, 703

Schlegel, D. J., Finkbeiner, D. P., & Davis, M. 1998, ApJ, 500, 525

Searle, L., & Zinn, R. 1978, ApJ, 225, 357

Sesar, B. et al. 2007, AJ, 134, 2236

Shapley, H. 1939, Proceedings of the National Academy of Science, 25, 423

Siegal-Gaskins, J. M., & Valluri, M. 2008, ApJ, 681, 40

Siegel, M. H., Majewski, S. R., Reid, I. N., & Thompson, I. B. 2002, ApJ, 578, 151

Simon, J. D., & Geha, M. 2007, ApJ, 670, 313

Sirko, E. et al. 2004, AJ, 127, 899

Springel, V., Frenk, C. S., & White, S. D. M. 2006, Nature, 440, 1137

Steinmetz, M. et al. 2006, AJ, 132, 1645

Totten, E. J., & Irwin, M. J. 1998, MNRAS, 294, 1

Vivas, A. K., Jaffe, Y., Zinn, R., Winnick, R., Duffau, S., & Mateu, C. 2008, ArXiv e-prints, 807

Vivas, A. K., & Zinn, R. 2006, AJ, 132, 714

Vivas, A. K. et al. 2004, AJ, 127, 1158

—. 2001, ApJ, 554, L33

Vivas, A. K., Zinn, R., & Gallart, C. 2005, AJ, 129, 189

Warnick, K., Knebe, A., & Power, C. 2008, MNRAS, 385, 1859

Wetterer, C. J., & McGraw, J. T. 1996, AJ, 112, 1046

Yanny, B. et al. 2003, ApJ, 588, 824